On-Site Characterization of Automotive Diffuser Aerodynamics by 3D LPT

by

Andrea Battegazzore

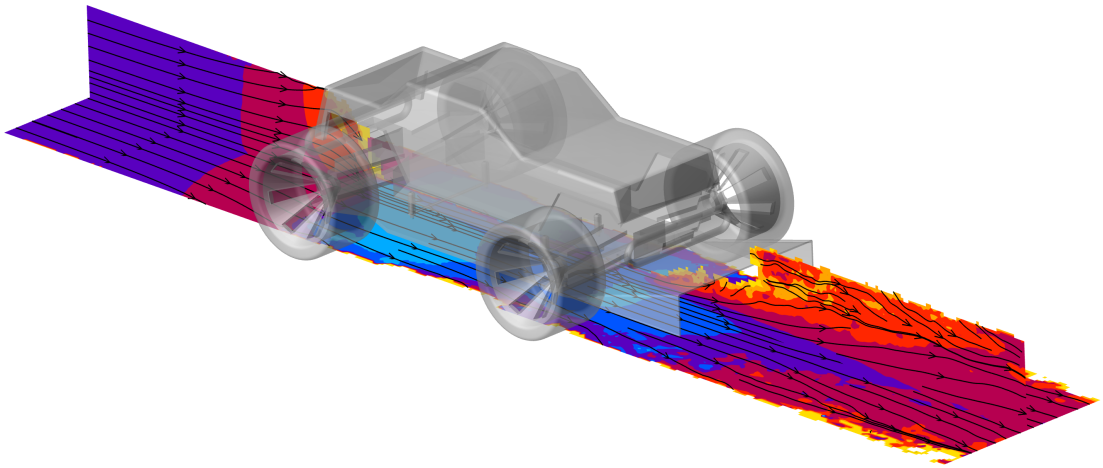

Supervisor:	Dr.ir. A. Sciacchitano
Daily Supervisor:	A. Grille Guerra
Institution:	Delft University of Technology
Place:	Faculty of Aerospace Engineering, Delft
Report Date:	Wednesday 8th May, 2024

TU Delft

Preface

Dear reader, I am pleased to present to you this document outlining the conception, construction and execution of a novel measurement setup to characterize the aerodynamics of automotive diffusers.

I would like to express my sincere gratitude to my supervisor Andrea Sciacchitano for initiating this project and for supporting me along the way with his extensive experience in the field of experimental aerodynamics. I would also like to thank Adrian, for providing crucial knowledge and support during the complex testing and data-processing phases. My gratitude extends to Fulvio Scarano for providing key insights that contributed to shaping the project and realizing its full potential.

Vital to the construction of the experimental setup was the support of Henk-Jan in the planning of the campaign and to ensure its safety, Dennis and Pieter for their help machining parts and Frits for operating the 3D printing machines.

I would also like to thank Aytek, Alex, Alejandro, Alessandro, Austin, Luca, Michael, Octavian and Tamim for joining me in December and assisting me through the experimental campaign.

Finally, my appreciation goes to my family, my close friends and my girlfriend who enabled me to stay motivated through this extensive stay at TU Delft.

Andrea Battegazzore
Delft University of Technology
Wednesday 8th May, 2024

Abstract

The research project focused on investigating the aerodynamic characteristics of automotive vehicles, particularly emphasizing the role of diffusers and underbody regions in generating downforce. Through its diverging, duct-like section, the diffuser converts the flow's kinetic energy into a pressure rise and is therefore responsible for the effective expansion of the airflow under moving cars. As a result of pressure propagation and the diffuser pumping effect [1], the flow characteristics within the diffuser have large consequences on the flow beneath the vehicle's floor. Considering this, the proposed objectives of this study were to develop an experimental setup capable of studying the flow dynamics around a scaled ground vehicle, to identify mechanisms of separation within the diffuser, and to explore the relationship between diffuser angles and downforce generation.

A novel Lagrangian Particle Tracking (LPT) facility was designed and constructed, featuring Helium Filled Soap Bubbles, LED illumination, and multiple high-speed cameras to characterize the flow inside automotive diffusers. A 50 cm long RC car, fitted with a custom floor and diffuser, traversed a region of seeded air in a Ring of Fire style [2]. Underground cameras viewed the moving car through a transparent panel, providing unparalleled optical access to the diffuser of the car. The on-site construction of the setup and the intrinsically realistic interaction with the ground, contributed to realism and fidelity while potentially reducing testing costs associated to wind tunnel operation. Particle tracks from multiple runs (> 20 for each diffuser), obtained with Shake-the-Box [3] processing, were averaged together. The outdoor experiment took place between November 22nd and December 4th, 2023, at the Flow Physics and Technology Laboratories of the Aerospace Engineering faculty of TU Delft in Delft, the Netherlands.

The setup was shown to be a valid alternative to conventional testing grounds to capture separation, 3D flow evolution and differences in the flow field between the diffusers with varying angles. The 15° diffuser led to the largest velocity ($u/U = 1.3$) under the car, the 10° diffuser produced the most downforce overall while the 20° diffuser entailed the most prominent separation, heavily affecting its ability to sustain low pressures under the car. Results were consistent with academic literature, showcasing the efficacy of the experimental setup. The results described the impact of the tyres in disrupting the mechanism of downforce generation through mass flow leakage through the sides of the car.

The research project advanced the understanding of automotive aerodynamics, highlighting the complexities of on-site track testing. Looking ahead, the established setup provides a solid foundation for future iterations, building on the accumulated knowledge and ultimately leading to the testing of a full-scale car or the broader application of the methodology to study bodies in ground effect.

Contents

List of Figures

List of Tables

Nomenclature

Abbreviation	Meaning
BFS	Bubble Fluid Solution
BNC	Bayonet Neill–Concelman (connector)
CFD	Computational Fluid Dynamics
FEM	Finite Element Method
FSU	Fluid Supply Unit
$HFSB$	Helium Filled Soap Bubbles
LDA	Laser Doppler Anemometry
LED	Light Emitting Diode
$LiPo$	Lithium-ion Polymer (battery)
LPT	Lagrangian Particle Tracking
PIV	Particle Image Velocimetry
PTU	Programmable Timing Unit
PTV	Particle Tracking Velocimetry
ROF	Ring of Fire
RC	Remote/Radio Controlled (car)
STB	Shake The Box

Symbol	Meaning	Unit
C_d	Pressure coefficient	[−]
C_l	Lift coefficient	[−]
d	Half diffuser width ($2d$ is the total diffuser width)	[mm]
e	Error	[−]
F_z	Force in z direction: downforce	[N]
$f_\#$	Camera's f-stop	[−]
h	Height or mesh cube edge length	[m]
l_d	Diffuser length (170 mm)	[mm]
L_u	Underbody length (550 mm)	[mm]
$M_d(\texttt{Var})$	Median of variable	[−]
$\dot{m}$	Mass flow	[g/s]
N	Sample size	[−]
p	Pressure	[Pa]
p_∞	Freestream pressure	[Pa]
$p_{n\to m}$	Indicative pressure between station n and m	[Pa]
q_∞	Freestream dynamic pressure	[Pa]
r	Number of runs or radius	[−]
t	Time	[s]
$\bar{u}$	Mean streamwise velocity	[m/s]
u	Velocity in x (streamwise) direction	[m/s]
u_c	Streamwise "car" velocity	[m/s]
U	General streamwise velocity used for normalization of velocities	[m/s]
U_∞	Freestream velocity. Often equal to u_c and used as U	[m/s]
v	Velocity in y direction	[m/s]
w	Velocity in z direction	[m/s]
x	Streamwise direction in vehicle's frame of reference	[−]
y	Spanwise direction in vehicle's frame of reference	[−]
z	Vertical direction ($\perp$ (xy)) in vehicle's frame of reference	[−]
$x^{'}$	Stream-wise direction in laboratory frame of reference	[mm]
$y^{'}$	Span-wise direction in laboratory frame of reference	[mm]
$z^{'}$	Vertical direction ($\perp$ ($x^{'}y^{'}$)) in laboratory frame of reference	[mm]
$\texttt{Var}^*$	Variable value at key frame	[−]
$\texttt{Var}^t$	Variable value on top surface	[−]
$\texttt{Var}^b$	Variable value on bottom surface	[−]
$\texttt{Var}_i$	Variable value at i^{th} node	[−]

Greek Symbol	Meaning	Unit
ρ_∞	Freestream (air) density	[kg/m^3]
θ	Diffuser angle	[°]
$\mu(\texttt{Var})$	Mean of variable	[−]

1

Introduction

The study of the flow around ground vehicles has always been a crucial part of their design, especially concerning the aspect of performance and safety. Going hand in hand with the development of more effective flow visualization and measurement techniques, the study of the vehicle's aerodynamics has been an increasingly important area of attention for manufacturers of race and private cars alike. These firms often aim to design vehicles that produce low drag and downforce to increase speed, reduce the likelihood of take-off and increase efficiency. One aspect of a vehicle's aerodynamics that is often overlooked is the underfloor region, which is heavily influenced by the properties of the diffuser. The underbody typically contributes to about 50% of the total downforce generated by race cars, with the remaining 50% achieved by the front and rear wing assemblies as displayed in Figure 1.1 [4].

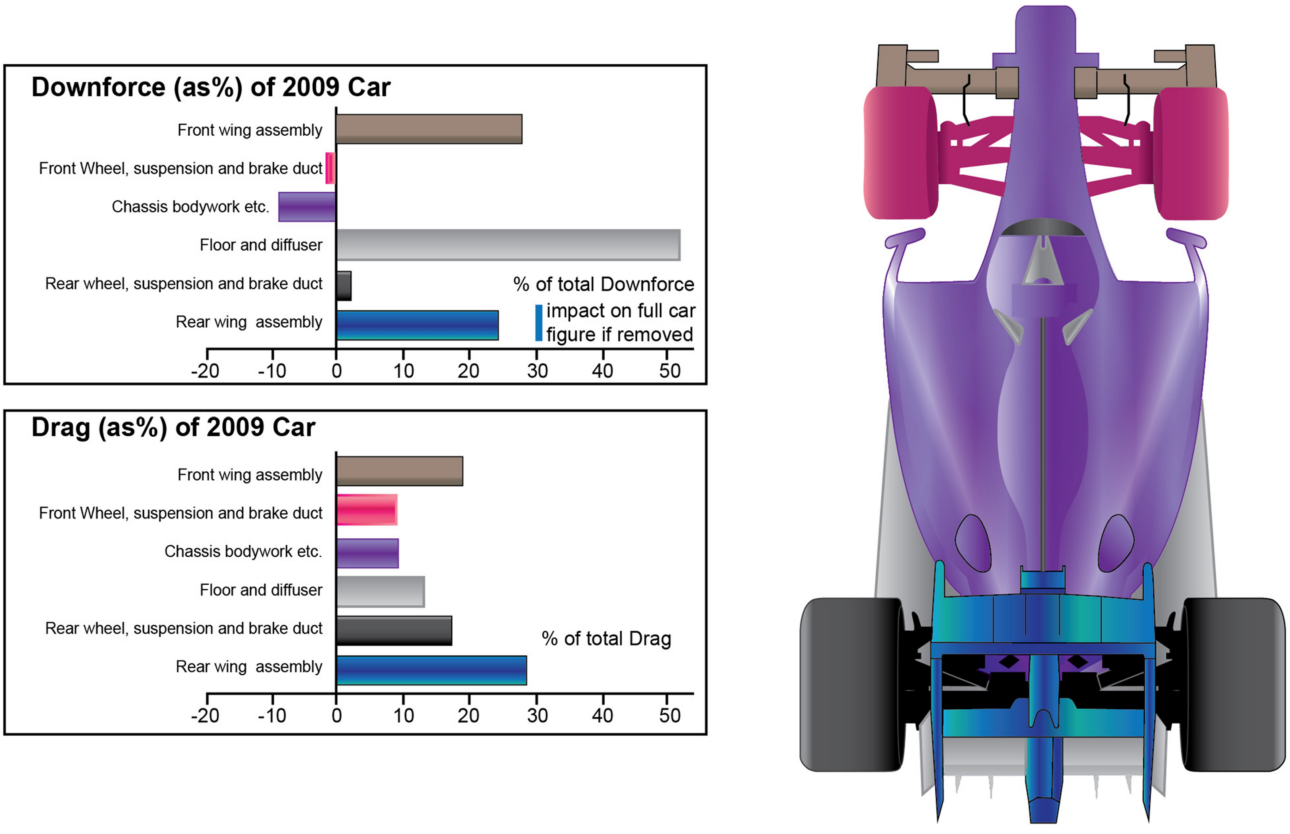

Figure 1.1: Force breakdown (Drag & Downforce) for different key regions of the 2009 F1 spec car [4]

The diffuser of a ground vehicle is the underfloor portion that joins the, usually flat underbody, with the rear of the vehicle. This diverging channel facilitates the expansion of fluid between under the car and the wake of the vehicle. It is this specific area that will be the target of this investigation through an extensive testing campaign.

The objective of this study is to design and execute an experimental campaign that leverages recent technological advancements concerning particle tracking, seeding, processing methods and testing mechanics to characterize the flow field in the diffuser of automotive vehicles. This broad goal is split into two non-technical macro objectives: to outline a novel measurement setup for outdoor vehicle aerodynamic testing and to showcase the potential of the proposed technology by discussing the 3D flow evolution inside the diffuser of a moving vehicle when varying one geometrical parameter. These goals consider a future full-scale facility and the generalization of the setup to accommodate the study of various ground-effect vehicles as the ultimate goal.

The core of this report begins with Chapter 2 which will review the academic literature on the aerodynamics of ground vehicles and, in particular of the underfloor and diffuser region. Within this chapter, Section 2.2, introduces a conceptual 1D model of a car, detailing the flow features expected. Chapter 3 introduces the current state of the Particle Image Velocimetry technologies including the aspect of tracers, volumetric PIV measurements, Shake-the-Box processing, and the Ring of fire methodology. Chapter 4 will summarize the literature and focus the research through a few detailed technical research questions. The design of the experimental setup, including the rationale for the choices made and the rundown of the steps necessary to obtain particle tracks are featured in Chapter 5. Later, Chapter 6 will outline how the data was processed before being presented and discussed in Chapter 7. The comprehensive stand-alone conclusion of the report found in Chapter 8 reintroduces the problem and links the key findings of the study with the leading research questions. The insights gained and the recommendations for future works on the topic are outlined in the same chapter (Section 8.3).

2

Vehicle Aerodynamics

In order to best tackle the research questions presented and direct the research phase, constructing a complete picture of the current state of the literature on the topic of vehicle aerodynamics is crucial. Since the dynamics of the flow around a moving vehicle form a complex inter-connected system, analyzing the diffuser's aerodynamic characteristics individually is not possible. This chapter will first introduce the most important aspects of the flow physics through the presentation of key academic articles. These tackle the problem applying varying degree of simplification in the testing procedure and in the car geometry (Section 2.1). The framework constructed will then be further expanded upon with by defying a 1D theoretical model to serve as a reference for all later discussions (Section 2.2).

2.1. Literature Review

Vehicle Aerodynamics is a crucial aspect of vehicle design as it allows for enhanced safety and significant performance gains. In general, passenger vehicles may be the subject of aerodynamic studies to reduce drag to maximise range and efficiency. This is increasingly important when contextualised in the current energy transition, where range is a major selling point of electric vehicles. Additionally, reducing the lift while managing drag makes passenger vehicles more stable and less prone to lift-off or tipping. The study of aerodynamics is one major area of attention also in the motorsport industry to enhance performance and gain competitive advantages against competitors. Sophisticated aerodynamics allows vehicles to achieve higher top speeds by reducing drag and reducing lap times by increasing downforce. Due to the interaction of tyres and the ground, an increase in downforce is directly linked to an increase in maximum grip and cornering speed through an effective larger normal force (linearly related to maximum force put through a tyre before slipping).

(a) Mercedes-AMG W13 2022 F1 contender [5]

(b) Ford GT Race car [6]

Figure 2.1: Underbody and diffuser geometry in motorsport applications

2.1.1. The Role of the Diffuser

The role of the underbody in generating high downforce with a relatively low drag penalty has been highlighted in Figure 1.1. An extreme take on the vehicle's underbody design is shown in Figure 2.1(a). Of significant importance to the correct functioning of the underbody as a mean to generate downforce is the diffuser. Figure 2.1(b) depicts a race car with a wing and a large diverging diffuser extending outwards at the car's rear. The vicinity of the ground to the vehicle's floor forces air to accelerate due to the immediate reduction in space available for the airflow to fill and travel through. Following Bernouilli's principle, air pressure must also decrease, generating a strong suction which is commonly described as downforce. This acceleration can be further increased by designing the underfloor similarly to an inverse-cambered wing. The added cambered section, referred to as the vehicle's diffuser, forces the flow to be deflected upwards by the "Diffuser upsweep" effect. This momentum exchange leads to additional downforce [7].

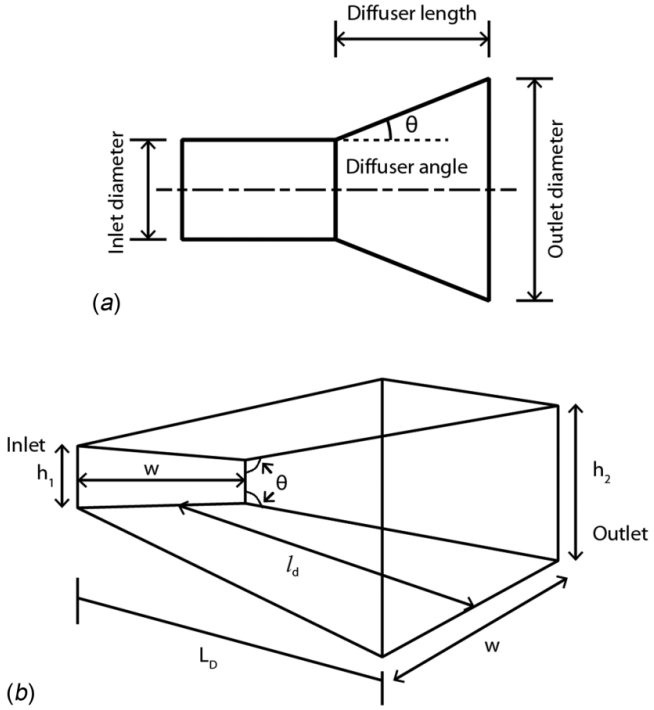

Figure 2.2: Schematic of a simplified diffuser [7]

A simple schematic of the floor and diffuser geometry and the main geometry parameters is reported in Figure 2.2. The inlet and outlet planes describe the slice between the vehicle and the ground at the location of the start and end of the diffuser. The measure of width is often assigned the value of $2d$. This is widely used to scale length variables. In addition to the previously described role of the diffuser, this portion of the underbody is responsible for transitioning the airflow from low pressure to atmospheric conditions at its outlet. This means that ignoring viscous effects and separation, any increase in area ratio (ratio between outlet and inlet diffuser areas) would force the flow beneath the vehicle to a higher velocity and lower pressure. In reality, increasing this parameter beyond a certain threshold inevitably leads to separation and a loss of efficiency.

The pressure distribution along the underbody of a simplified vehicle model fitted with a sloped diffuser is shown Figure 2.3. The initial acceleration phase, small recovery, strong suction peak at the diffuser inlet and final recovery to atmospheric conditions are typical to any underbody fitted with a diffuser. The downforce generated by this specific diffuser could be obtained by integrating the pressure force over the underbody area.

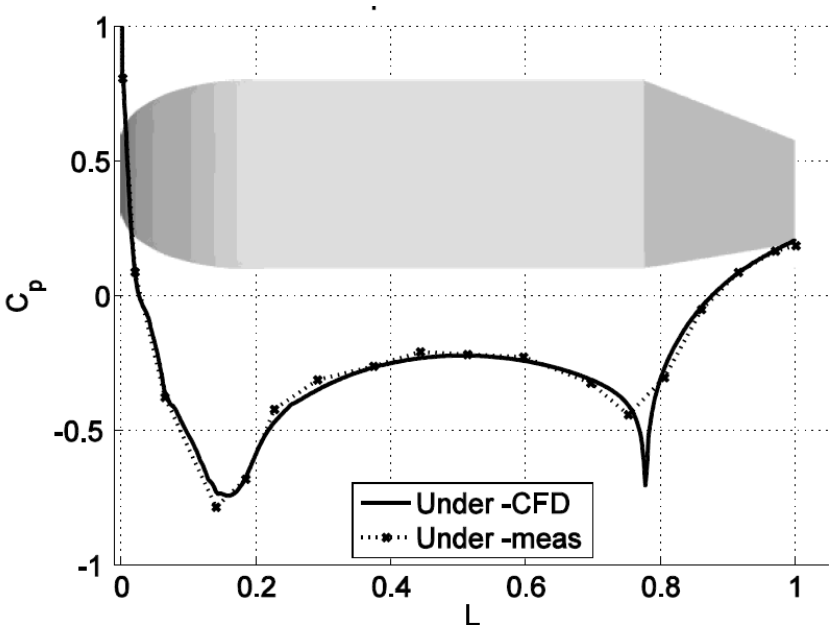

Figure 2.3: C_p distribution along the centerline of the bottom surface (flat floor and 9.4°diffuser) of Ahmed body obtained with pressure taps and CDF [8]

2.1.2. Testing of Diffusers with PIV, Oil Flow Visualization and CFD

It has been widely recognized that various parameters influence the flow dynamics in the diffuser and the underbody. The main geometrical quantities are the area ratio, the diffuser angle, its length, and the ride height. In addition, various studies were made on the effect of multi-channel diffusers [9] and diffusers sealed with side-skirts [10]. The dominant aerodynamic concepts and structures that dominate the flow in the diffuser are vortex generation and breakdown, separation and boundary layer growth.

Identification of Flow Regimes

Senior [11] presented a study of the diffuser flow through multiple wind tunnel experiments with a 1.3 m long Ahmed body fitted with a diffuser having a $2d$ value of 0.326. The model in question is shown in the schematic reported in Figure 2.4. The study was carried out with a rolling-belt floor simulation and boundary layer suction devices and at a wind speed of 20 m/s, achieving a Reynold's number of 6.6×10^6. The study provides a comprehensive comparison between LDA, (Planar) PIV, CFD, oil flow visualization and pressure taps to build a complete picture of the flowfield. The optical access required for PIV was enabled through the use of (partially) transparent side plates. Due to the wide range of flow measurement and visualization options, the author chose to only vary ride height.

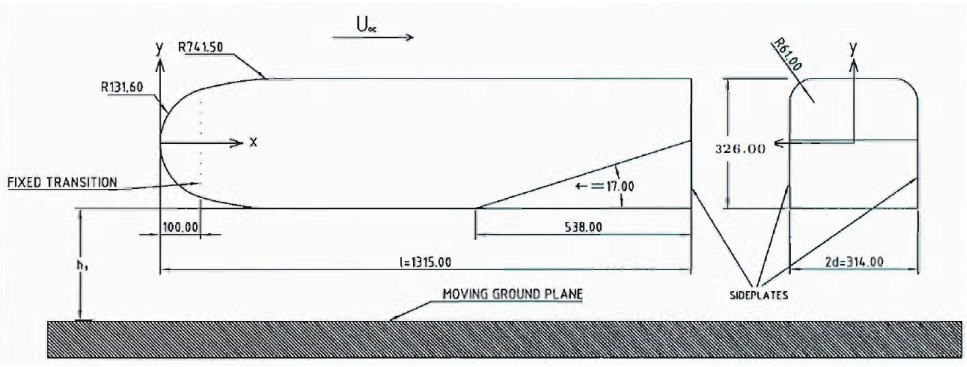

Figure 2.4: Schematic of wind-tunnel model used by Ref. [11] featuring a Ahmed body fitted with a diffuser and side skirts with no wheels on a rolling belt floor

One important result of the research reported in Ref. [11] was the identification of the four downforce variation regions as shown in Figure 2.6. The four regions, marked *A*, *B*, *C* and *D*, describe "downforce enhancement", "maximum downforce", "downforce reduction" and "constant low downforce". In inviscid theory, downforce should increase to infinity as ride height decreases while in reality, viscous effects limit maximum downforce due to choking in the underfloor region [7]. As demonstrated through the use of force balance measurements, downforce initially increases (lift becomes more negative) as ride height decreases until the start of the region *B*, where any further decrease in ride height leads to a small or negligible change in negative lift. In region *C*, downforce rapidly decreases with a small decrease in ride height, marking the location of flow of separation and the rise of asymmetric flow in the diffuser caused by a breakdown in one or both vortices. Finally, region *D* relates to a low downforce plateau with respect to ride height.

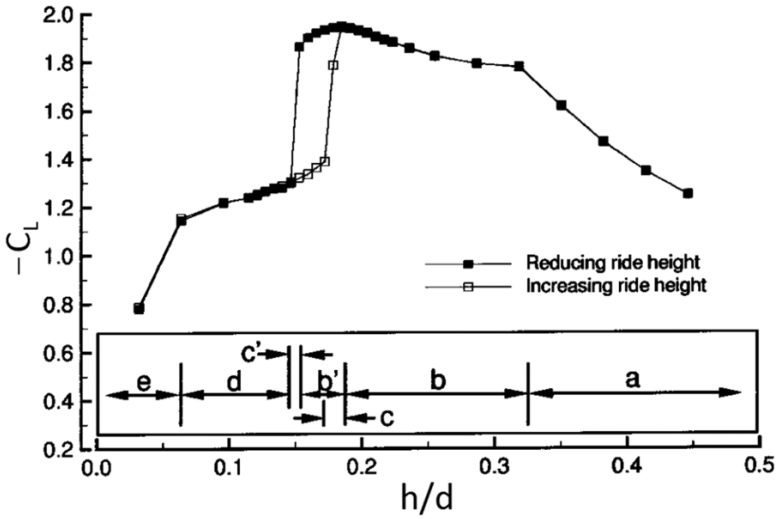

Figure 2.5: Variation of downforce in the diffuser with varying ride height when increasing and decreasing ride height forming a hysteresis loop [12]

Ref. [12] performed a similar experiment by tracking the 15-second average downforce for a set diffuser angle when varying ride height. The study concluded that when increasing or decreasing ride height produced different downforce levels for the same ride height. In other words, when increasing ride height, re-attachment was not seen to occur exactly where separation was seen when decreasing ride height, leading to the hysteresis loop shown in Figure 2.5. The loop arises from a difference in the location of Type *C* flow (downforce reduction zone).

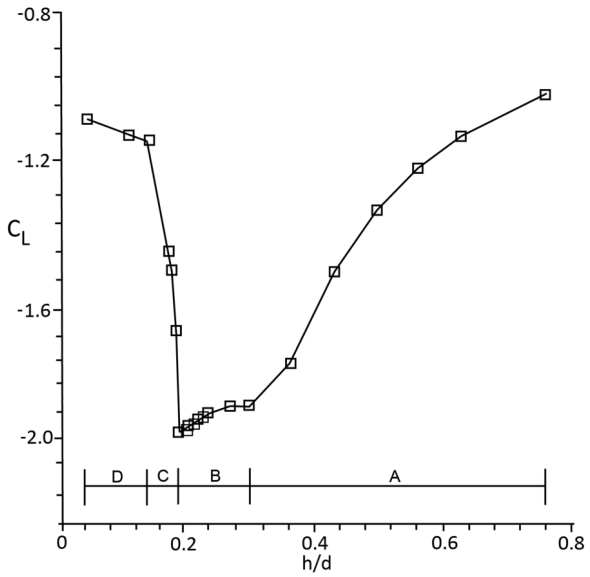

Figure 2.6: Variation of ride height for different ride heights averaged over 15 force balance measurements [11]

Visualization of vortex structures

Notably, the use of PIV in Ref. [11] leads to important cross-validation of results by confirming that the vortex pair in the diffuser dominates the flow in this region and that a large portion of downforce is generated through the effect known as "diffuser pumping" [11][7] by the vortex pair. Senior concludes that a drastic change in vortex flow occurs as ride height varies leading to large changes in the downforce generated "due to the low-pressure zones associated with these vortices". The author also mentions that the effect that leads to downforce reduction at low ride heights is linked to the presence of weak and asymmetric vortices in a (partially) chocked flow, not to boundary layer merging. Figure 2.7 displays three instantaneous vorticity plots and one averaged map of vorticity showing the vortex structure in a type *A* flow. The setup of Ref. [11] showcases the advantages of using PIV as a stand-alone measurement technique or when paired with another measurement method to better visualize the flowfield. However, it must be noted how such configuration requires a relatively large wind tunnel with a rolling belt and complicated boundary layer suction system. In addition, an upscaled version of this setup, with a more complex diffuser geometry, without transparent side plates and possibly wheels would be a large challenge.

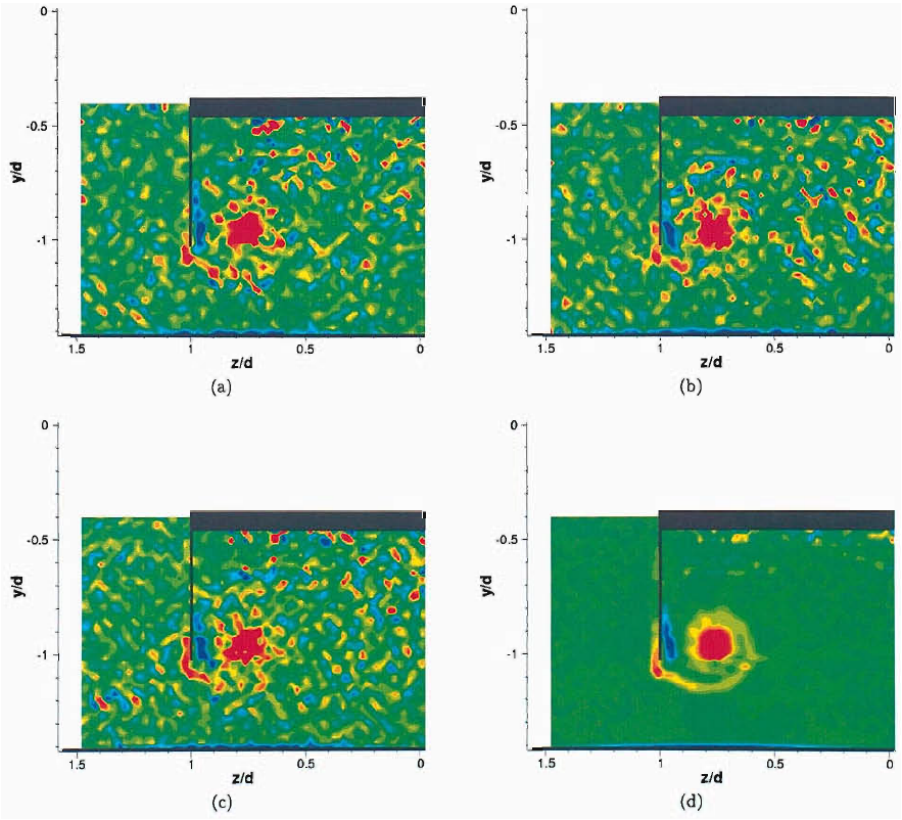

Figure 2.7: Instantaneous and averaged vorticity plots, generated with PIV, in a plane inside the diffuser showing the presence of the inlet-born vortex [11]

Side plates and advanced concepts

Side skirts or side plates are a common device used by aerodynamic designers to seal the underfloor region in order to minimize the pressure of the flow. The sealing prevents high(er) pressure air from entering the floor region disrupting the vortices and the accelerated underbody flow. A simple experiment with a fully sealed and unsealed venturi-style diffuser showed how the skirts provide larger downforce gains at relatively small diffuser angle (5°) while it caused a loss in downforce for 10°and 15°. This was attributed to diffuser stall [10]. This research showcases how skirts and side plates are effective ways to manage the flow to increase downforce but attention should be paid to prevent complete stall.

In recent years, more complex geometries such as multi-channel diffusers [9], curved diffusers [7], and diffusers fitted with strategically placed gaps [13] are being researched as performance margins reduce and competition increases in motorsport activities and while the automotive industry is forced to innovate to fit the current electric transition.

Oil flow visualization

Multiple studies have identified the vortex pair occurring in the vortex by using oil flow visualization technique. Images taken of the oil pattern in the diffuser after the experiment clearly characterize the flow by locating the location of vortices as well as possible asymmetries and separation bubbles. Figure 2.8(a) showcases the different flow patterns for different diffuser angles at maximum downforce ride height[1]. Ref. [10] describes how increasing diffuser angles leads to an earlier breakdown in the vortices as well as in an earlier rise in the symmetric central separation bubble. Ref. [12] also shows that the largest downforce is created at the higher diffuser angles tested (20°) while Refs. [9] and [14] found that the largest downforce

[1] $h_r/(d \times \theta = 0.66$, 0.69 and 0.58 respectively

occurs at a lower angle, in their case of 13°. This also matches with the findings reported in Ref. [15] which performed many experiments with diffuser angles at varying ride heights. It should be noted how Refs. [12] and [15] experimented in a wind tunnel with a rolling-belt floor system while Refs. [14] and [9] didn't. From these studies, it is clear that changes in the diffuser angle produce significant changes in vortex structure and separation. In addition, the ground simulation method employed could impact the results.

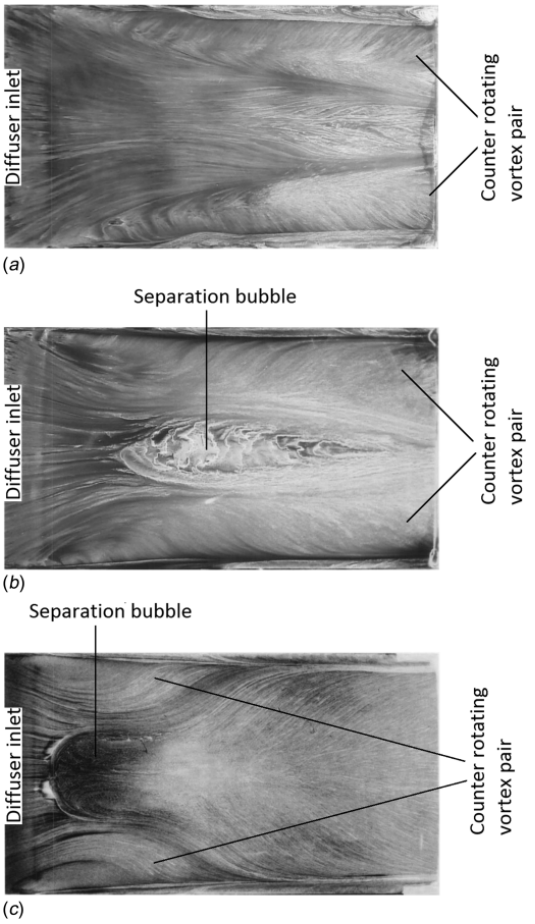

(a) Oil from visualization of diffuser flow for 5°, 10°, and 15°diffuser angles, at maximum downforce ride height, annotated in [7] from the experiment of [12]

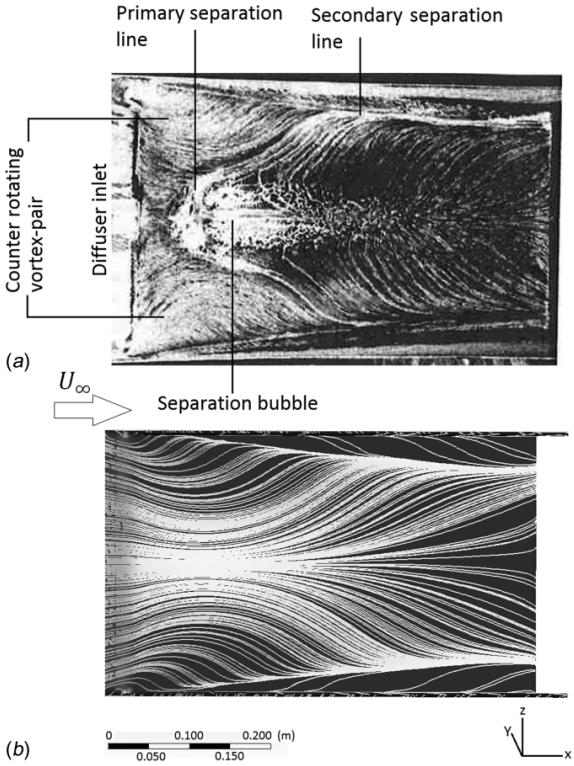

(b) Annotated oil flow visualization of diffuser [11] as presented in [7] (top) compared to CFD results presented in [7] based off [1] results

Figure 2.8: Oil flow visualization and CFD computation of diffuser flow at different regimes

Finally, Figure 2.8(b) shows how oil flow visualization techniques compare to CFD simulation to predict the location of separation and the vortices. Although some differences are visible, the simulation correctly predicted the ride height leading to maximum downforce as well as the presence of a separation bubble (emerging slightly more towards the rear in the CFD simulation).

Transition and setup considerations

It is worth noting that Ref. [12], Ref. [11], Ref. [16] all used a similar setup consisting of a rolling floor with boundary layer suction. These studies decided to fix transition before the diffuser inlet through the use of transition strips, perhaps to minimize the effects of Reynold's mismatch between the simulated case and a full-scale vehicle's diffuser case.

To summarize, this chapter displayed some of the recent developments and investigations in the field of underbody and diffuser aerodynamics. These references painted a complete picture

of the various tools used in flow visualization for these specific applications as well as highlighted the common limitations of these tests being linked to the simplicity of the models used, often without wheels or side skirts. Tools such as LDA, PIV (Planar, small-scale), Oil flow visualization and CFD are a few of the technologies that have been employed to study the effect of various geometrical parameters (ride height, area ratio, diffuser angle etc.)and diffuser configurations (skirts/no skirts, multi-channel etc). Developing a measurement technique that could bridge the gap between heavily simplified models and full-scale vehicles could help identify the flow structures which still require research such as the role of the wheels, the impact of a rougher ground plane as well as the removal of rolling-floor related errors.

2.2. Conceptual Model

A simplified model based on potential flow is here introduced. Here, an area-based 1D duct representation of the underbody of a vehicle is built. Later, 2D and 3D effects that explain the flow behaviour in a real scenario are discussed.

2.2.1. Mass Continuity Analysis

The 1D geometry utilized for this investigation is shown in Figure 2.9. This represents the centerline of a simplified underbody of a ground vehicle fitted with a diffuser. The real car has a sharp, splitter-like[2] leading edge of the floor plate while this model entails a rounded leading edge. Due to the definition of the coordinate system and dimensions defined and used later in the discussion of the results, the x-coordinate is expressed as length normalized with L_u, the underbody length: 550 mm. The radius of the inlet curve is 30 mm while the height of the central portion of the floor above the ground is 20 mm. These measures were set to impose a 5 to 2 height/area ratio between the free-stream and the floor region. This is the same that is observed in the real data that will be discussed in Section 7.1 (Figure 7.13).

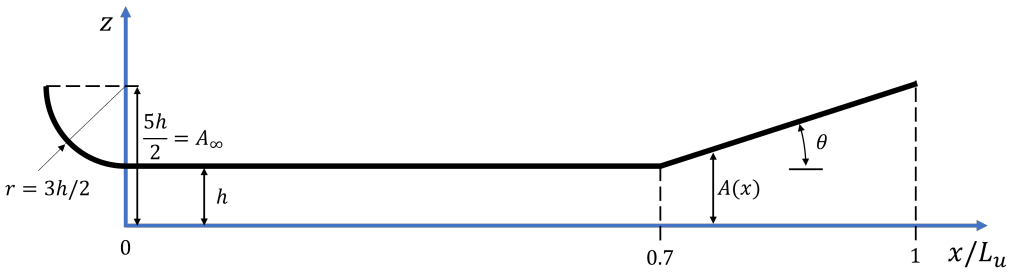

Figure 2.9: Schematic of the geometry used

Since this evaluation is based on a 1D potential flow model, the "cross-sectional" area of the "duct" created between the ground and the underbody surface is equal to the height ($z = A(x)$) times a constant width. The measure of this width is not important due to the mono-dimensionality of the method. The assumptions that govern the model discussed are presented below.

Assumptions

- **A1:** The flow is inviscid.

[2]A splitter is a flat surface often fitted on race cars which extends in front of the vehicle's bumper and virtually extends the floor. This is used to 1) Increase the floor length available for flow acceleration and 2) Force the stagnation flow to push on the top side of this surface creating a large pressure difference and thus (front) downforce.

- **A2:** The flow is incompressible.
- **A3:** The flow is mono-dimensional (1D).
- **A4:** The ratio between the height of the stagnating streamline, from the ground, in the free-stream and the height of the flat floor region is 5 to 2. In other words, the duct profile shown in Figure 2.9 has an area ratio of 5 to 2 between "inlet" and "throat".

Note that in this context, A4 is considered an assumption. This measure is the same as the real ratio of areas seen after processing the experimental data.

Given this framework, the mass flow through the duct must be constant due to continuity. In addition, due to assumption A2, ρ is also constant. This leads to the relationships shown in Equation 2.1.

$$\begin{aligned} \dot{m} &= \rho A u \\ \frac{\dot{m}}{\rho} &= Au = \text{const.} \end{aligned} \tag{2.1}$$

Set area ratio By fixing the area ratio between free-stream and floor to 5 to 2, the magnitude of streamwise speed (u) can be obtained at all sections of the duct: $u(x)/u_\infty = A_\infty/A(x)$ with $A_\infty = 50$ mm. Since u_∞ is an arbitrary constant, the speed is always used when normalized for this investigation. By imposing this constraint and using the equations shown in Equation 2.2, $C_p(x)$, at any x location can be defined as $1 - (A_\infty/A(x))^2$.

$$\begin{aligned} C_p &= 1 - (\frac{u}{U_\infty})^2 \\ C_p &= \frac{p - p_\infty}{\frac{1}{2}\rho_\infty U_\infty} = \frac{p - p_\infty}{q_\infty} \\ p &= C_p q_\infty + p_\infty \end{aligned} \tag{2.2}$$

This shows that as A and so the channel height narrows C_p becomes negative, implying a drop in pressure as velocity increases. The results of this analysis are shown in Figure 2.10.

Since the area ratio has been fixed between the free-stream and the floor, no velocity and pressure differences are seen in the underfloor region upstream of the diffuser among diffusers with different θ. The geometries differ in the expanding section. Here, the shape of the 20° diffuser forces the flow to expand from the flat floor to an outlet area which is larger than the free-stream one. For this reason, the streamwise velocity decreases below $1U$ (over-expansion). Similarly, the outlet of the 5° diffuser entails a relatively small outlet area which is not sufficient to fully expand the flow back to atmospheric conditions (under-expansion). In this 1D case, the only scenario where pressure can be fully recovered is when the diffuser's outlet area equals the free-stream area. Setting the area ratio to be constant for different diffusers is not a realistic approach since the area ratio itself is a consequence of the diffuser geometry and the propagation of its effects upstream. With this assumption, a floor with no diffuser would produce the lowest pressure through the duct and so, when integrated, the largest downforce. This is the opposite of what is expected for a fully attached and perfectly expanded flow.

Stagnation paradox Due to the way this model is set up, the region where a real, 3D, vehicle would experience stagnating flow, is actually characterized in the "set area ratio" model by $C_p = 0$, not by $C_p = 1$. Indeed, in this 1D model, stagnation cannot occur due to the lack

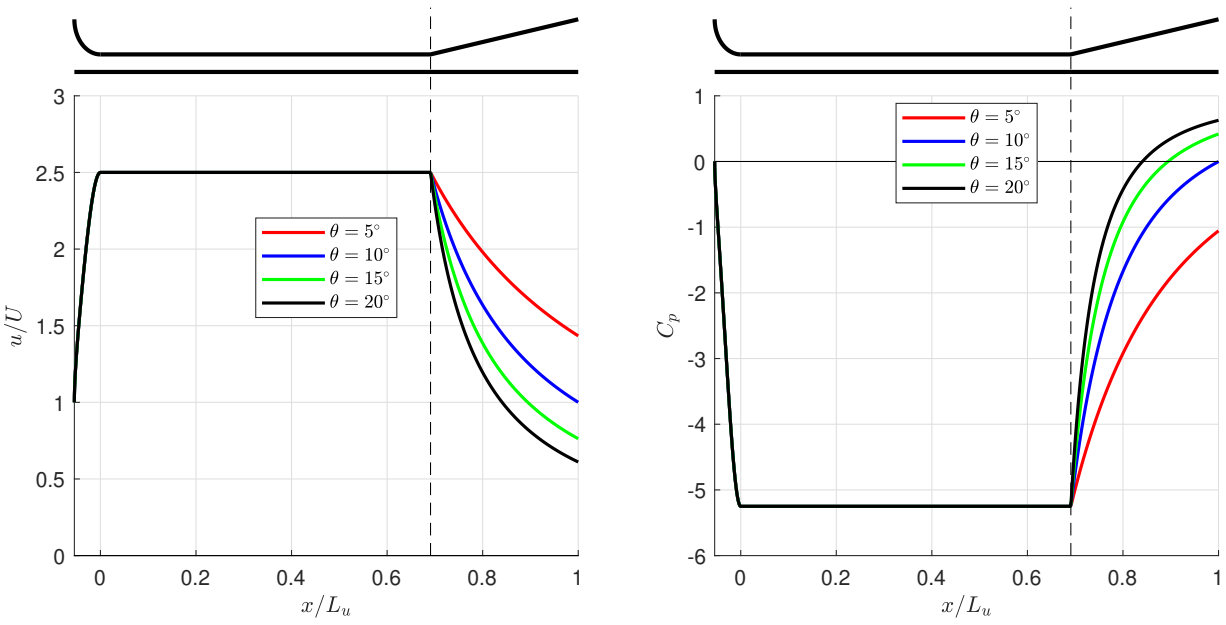

(a) **(b)**

Figure 2.10: Normalized speed and C_p through duct for different θ at fixed inlet to throat area ratio

of velocity variation in the direction perpendicular to the flow. $C_p = 0$ relates to free-stream conditions while $C_p = 1$ marks region where $u = 0$.

Set outlet pressure The discussion presented above is fully based on area variation through the channel by fixing the free-stream to "throat" area ratio. A more realistic approach would be to fix the outlet pressure to p_∞ to simulate perfect expansion and recovery to free-stream conditions. Ignoring separation, the flow speed can be integrated backwards (instead of forward) from the diffuser outlet ($x/L_u = 1$) to the diffuser inlet and the floor inlet. For this analysis, the curved inlet to the floor shown in Figure 2.9 is removed. The geometry now also matches with the floor geometry used in the actual experiments. The lack of set area constraint between free-stream and floor lets the diffuser's area ratio dictate pressure and speed throughout the whole domain.

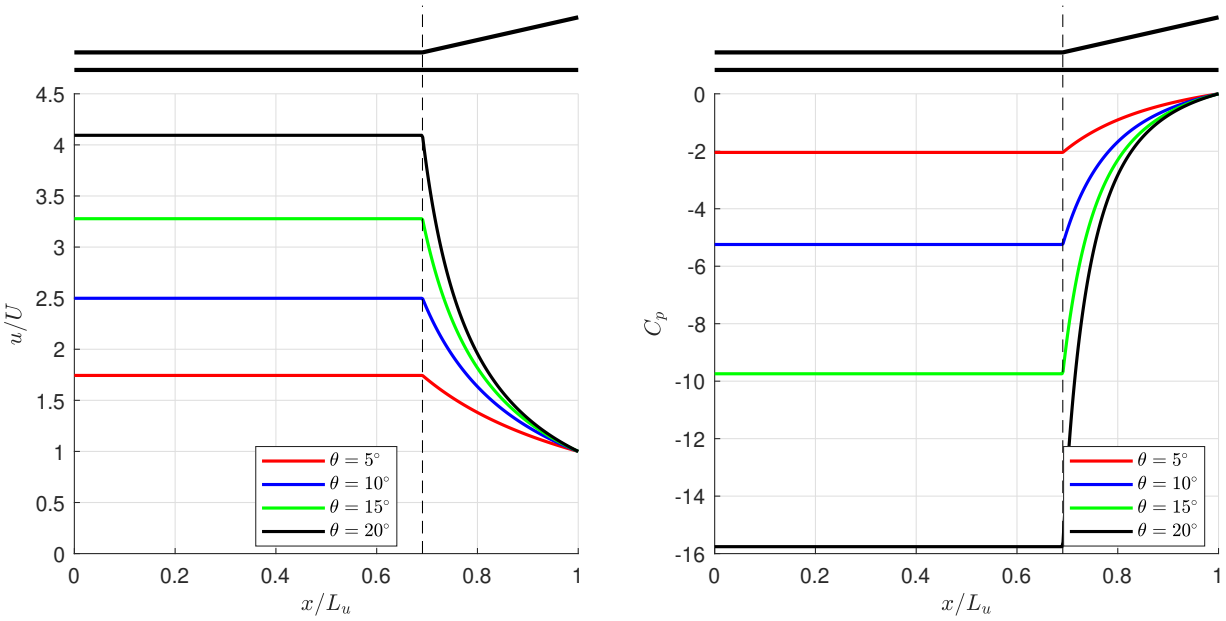

(a) **(b)**

Figure 2.11: Normalized speed and C_p through duct for different θ at fixed outlet pressure ($C_p(x/L_u = 1) = 0$)

The effect that this change has on the pressure and velocity in the floor is portrayed in Figure 2.11. As expected, a diffuser angle allows for a lower pressure to be maintained through the floor region. The relative differences (qualitative, not quantitative) between diffuser angles should hold in a non-separated 3D model.

When comparing this pressure distribution with Figure 2.3, it is clear that, while the general pattern and sign of the pressure coefficient are matched, there is a large disagreement in terms of pressure coefficient magnitude and shape along the duct (peaks). This suggests that the two peaks that are observed in the literature are to be attributed to flow curvature and viscosity-related effects that are not accounted for here. These effects are discussed in the next paragraphs.

2.2.2. 2D Effects

As the flow is squeezed through the entrance of the duct[3], a pressure gradient must exist to sustain this centripetal acceleration. Therefore, in a 2D version of this simplified case, the pressure gradient would point outward from the curved inlet, implying a low-pressure peak would exist on the curved surface. This effect is commonly observed on 2D plane airfoils, where additional suction is measured or predicted somewhere on the curved leading edge of the suction side. This is a 2D effect commonly referred to as centripetal acceleration leading to suction.

These effects can be appreciated through Figure 2.12. Here, experimental results show flow stagnating and being deflected around a car in close proximity to the ground. On the right, a conceptually equivalent scenario is presented with a high-pressure region in red and a low-pressure region in yellow. These source and sink-like regions, as commonly described in potential flow theory, represent the car's flow blockage and the subsequent suction which causes the streamlines to curve and straighten entering the floor-ground duct. It is this secondary low-pressure "bubble" which, in a 2D case, would result in a high-velocity peak. Following the same rationale, a vehicle fitted with a diffuser would exhibit another pressure peak at the inlet of the diffuser due to another instance of flow curvature and centripetal acceleration.

[3]In absence of a physical entrance nozzle, the streamlines will follow a naturally curved shape anyhow.

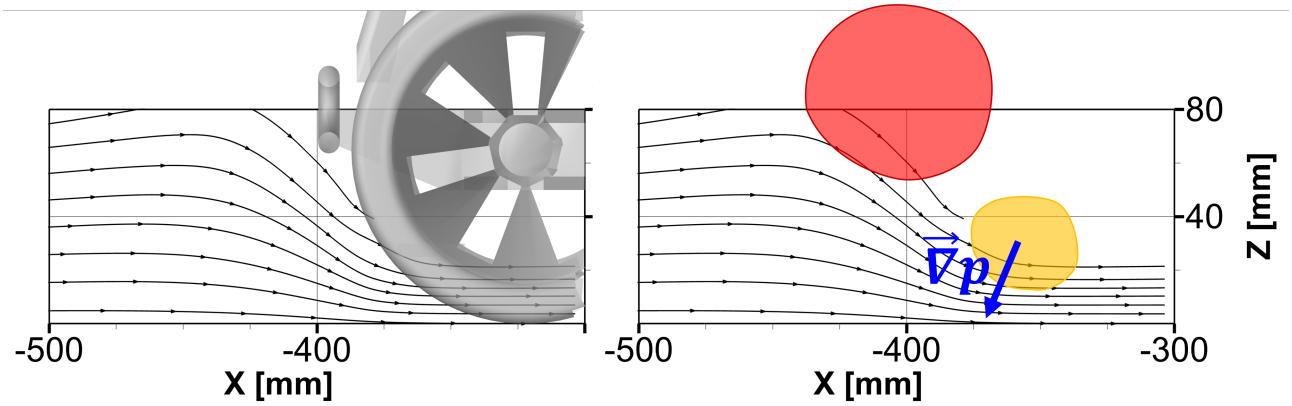

Figure 2.12: Streamlines stagnating and curving around and under model car (left) and equivalent model (right) with high pressure (source-like, red) area and low pressure (sink-like, yellow)

2.2.3. 3D Effects

In a real scenario, 3D effects would also play a role. These are a result of the finite nature of the floor (in this frame of reference, in the y direction). A finite floor will experience a strong difference between the pressure under the vehicle and on the sides of the vehicle. Ignoring the presence of wheels and other flow-perturbing appendices, the pressure just outside of the flow in the spanwise direction is close to the free-stream pressure. This causes air to be sucked into the floor region from the sides. This makes the mass flow under the vehicle to monotonically increase towards positive x.

Furthermore, the absence of tyres constitutes a large simplification of the model that cannot be overlooked. The wake, caused by 3D effects together with viscosity related effects, leads to a high-pressure zone in front and a low-pressure area at the back of each tyre. Depending on the size, shape and roughness of the tyres, these disturbances may create pressure gradients larger than the ones caused ground effect aerodynamics in the floor and the diffuser.

2.2.4. Viscosity and Turbulence Related Effects

In a viscous flow, a boundary layer would develop on surfaces. In a realistic experiment with a moving vehicle or wind tunnel experiment with a stationary vehicle and a rolling floor, a boundary layer will grow on the vehicle floor's surface causing deceleration of the flow. With perfect energy conservation, this deceleration would be compensated with an equal acceleration in the remaining portion of the unaffected flow, maintaining mass conservation. In practice, some of the energy is lost in highly turbulent regions and dissipated as heat. In the floor region, this effect, mixed with the decay of the centripetal acceleration that causes the low-pressure peaks discussed, leads to a "valley" of higher pressure in the central portion of the diffuser as shown in Figure 2.3.

Due to the fact that the flow under the vehicle travels at a streamwise velocity which is higher than free-stream, a boundary layer would grow on the ground as well. Considering a moving vehicle's frame of reference, the flow under the car travels at $u/U > 1$ while the ground moves at $u/U = 1$. Since the speed difference between the flow and the car is much smaller than between the flow and the car's underfloor, the boundary layer would grow much slower. Therefore, as the flow accelerates, this second boundary layer is expected to interfere more and more.

2.2.5. Typical Flow Characteristics of 3D Model

To conclude this chapter, connect the theory to reality and contextualize the literature, a series of observations of the 3D flow structures and patterns that can be made from everything

discussed are presented. Locations are addressed utilizing the key points and spatial position of objects depicted in Figure 2.13 are used often used. This figure depicts an Ahmed-body-like object fitted with a diffuser (with side plates). A side, rear and bottom view are shown, along with an isometric view of the rear-right side of the object in the bottom-right corner of Figure 2.13.

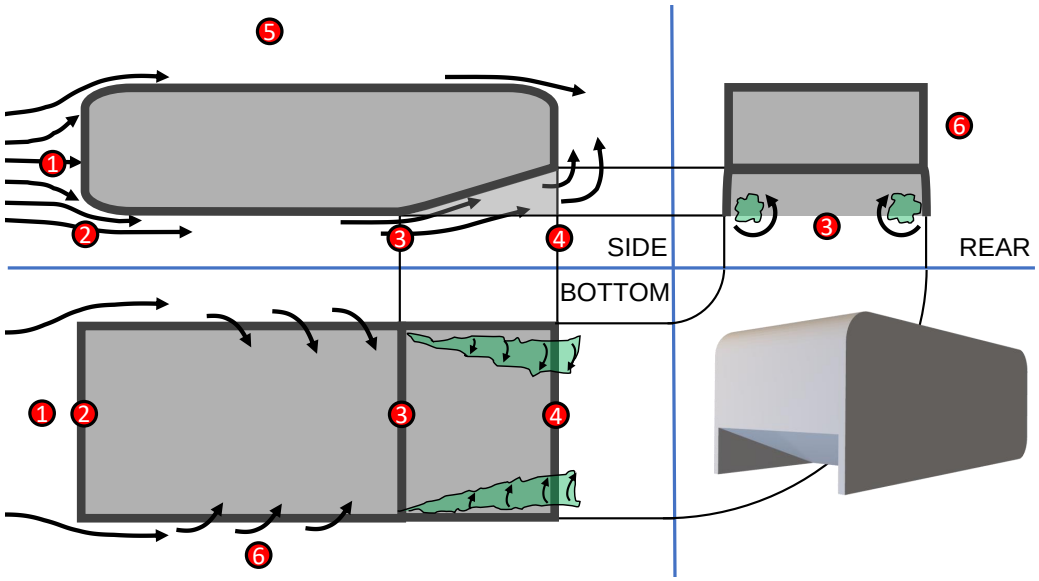

Figure 2.13: Schematic of 3D flow patterns on simplified car geometry with side plate fitted diffuser: side, bottom, rear and isometric 3D view.

- **Free-stream conditions and stagnation (1):** The free-stream, travelling with at U_∞ and at a pressure p_∞, stagnates at point **1**. Here, all kinetic energy is converted into pressure energy. Ignoring energy losses, the pressure p_1 equals the total pressure at the free-stream ($p_\infty + 0.5\rho_\infty U_\infty$).
- **Acceleration in the floor (2→3):** Air particles belonging to streamlines below the stagnation streamline curve around the vehicle and are forced into a smaller cross-sectional area. This causes the streamwise acceleration shown in Figure 2.10. In the floor, $p_{2\to3} < p_\infty$ and $u_{2\to3} > u_\infty$.
- **Streamline curvature and suction peak (2, 3):** In addition to the low pressure caused by area reduction, in region **2**, additional suction due to the centripetal acceleration occurs. This acceleration, provoked by a force, exists due to the presence of a positive pressure gradient outward normal to the leading edge of the floor. It is this pressure gradient that allows and forces the streamlines to curve. Therefore, p_2 is a local minimum in the region **2→3**. The same effect is expected at **3**, where (attached) flow bends upwards to follow the diffuser surface. These two peaks are referred to as first and second peak respectively throughout this study.
- **Pressure side:** At station **5**, the pressure can be considered to be equal to the one at free-stream ($p_5 = p_\infty$). The pressure difference between the floor in the region **2→3** and **5** is the main contributor to the downforce expected from this type of ground effect vehicle.
- **Expansion in the diffuser (3→4):** Due to the ratio between the height (and area) of the inlet (**3**) and outlet (**4**) of the diffuser, the flow passing through the diffuser is expanded. In absence of separation and turbulence, this expansion is optimal and the diffuser efficiently expands the flow from p_3 to p_∞ at **4**. Thanks to this physical constraint at the diffuser's outlet (**4**), the larger the area ratio between **4** and **3**, the lower the pressure at diffuser's inlet (**3**) and under the car (**2→3**) can be. For this reason, the expansion in the diffuser is

key in providing additional suction under the car, amplifying the streamwise acceleration discussed.

- **Entrainment and inflow:** Due to the finite width of the floor section, there exists an interface region between the low-pressure region in the floor (**2**→**3**) and the vehicle's sides (**6**). As done for the pressure surface of the vehicle at station **5**, the pressure at **6** can be considered to be the same as p_∞. Since the left and right parallel sides experience the same pressure delta, the side forces cancel out. However, due to the lower pressure in the underbody region, high-pressure air in **6** "leaks" into the floor (**2**→**3**). This increases the mass flow in the floor and compensates, in part, the process of boundary layer growth by injecting fresh flow from the sides.
- **Wake (4):** In the wake of the vehicle, a region of separated flow can exist. This depends on the geometry of the vehicle here.
- **Separation:** At the inlet of the diffuser, where the underbody presents a kink, separation can occur. When this happens, expansion is sub-optimal. This disrupts the pressure recovery which in a separation-free scenario would impose additional acceleration and suction in the floor (**2**→**3**). This relates to the (loss of) "diffuser pumping" [11] discussed in Section 2.1. For this reason, separation in the diffuser causes increased drag and more dramatic pressure losses which may lead to lift generation but also a reduction in flow velocity under the floor. The latter causes pressure to be higher, on average, under the car compared to the non-separated case, leading to a loss in downforce.
- **Vortices:** The spanwise forces explained to exist between under the floor (**2**→**3**) and the free-stream (**6**) are similar in the diffuser (**3**→**4**). The presence of a side plate creates a strong pressure differential between the inner diffuser volume and **6** ($p_{3\to4} < p_6$) as looked at from the rear-view (Figure 2.13). The presence of a pressure difference implies a force perpendicular to the side plate's surface similar to the working of a flat plate/airfoil. These side forces cancel out between the left and right side plates. Furthermore, this pressure difference causes the generation of counter-rotating vortices at the edge of the side plates. Again, this can be compared to the physical principles that generate vortices at the tips of finite wings. In the context of vehicle aerodynamics, these are the vortices that have been discussed (Section 2.1). These have also been linked to better sealing and flow stability in this region.

3

Particle Imaging Methods in Aerodynamics

Particle Image Velocimetry is a non-intrusive flow visualization technique which allows its user to gain valuable information about the complete 2D or 3D velocity field on a plane or in a volume. This tool, used to study the behaviour of flows, is particularly relevant for its ability to combine qualitative macroscopic flow visualization, with rather accurate quantitative flow measurement. In addition, the fact that the entirety of the flow is measured and captured in a single instant allows for the computation of (spatial) derivative-based variables such as vorticity and viscous dissipation [17].

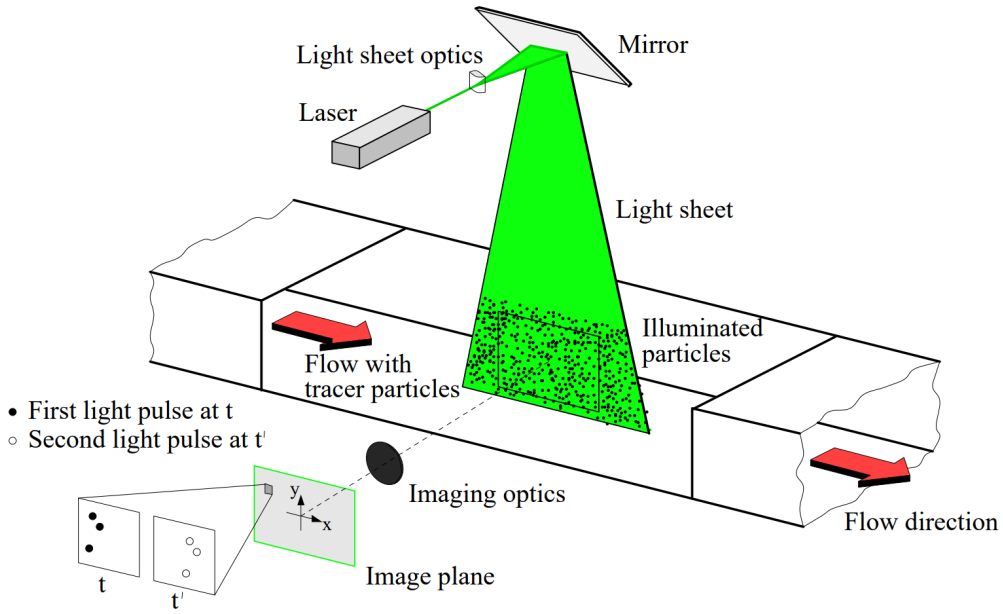

Figure 3.1: Planar PIV setup for wind tunnel measurement [18]

Generally speaking, PIV requires the use of cameras to capture the movement of small particles that have been injected into the flow. These particles are usually shined with a strong light, usually a laser or a powerful LED. The light emitted from these sources, usually diverted into a thin plane structure with the use of lenses, is reflected by the particles in the flow making them visible to the camera. When a fluid flow, rich with tracers, passes around a test model, the tracers will follow the fluid and thus visualise the path of the latter. Taking a pair of closely shot images of the flow reveals, after post processing, the velocity field of the illuminated particles in the camera's field of view. A general setup with all the main elements of a PIV experiment

is shown in Figure 3.1.

This specific flow visualization and measurement tool has been employed, as Passamore reports [19], in many different industries since the advent of the availability of more advanced imaging technology. In particular, the automotive industry has shown interest in this tool when discussing internal flows in portions of engines and channels. The study of external flow aerodynamics with PIV has been limited by the "relatively small number of specialist applications" [19], concerns about accuracy and technology limits (large scale, optical access). The following sections will detail the PIV methodology in all of its aspects (area/volume of interest, post-processing algorithms, test layout and tracer technology).

3.1. Volumetric PIV

The most simple type of PIV implementation requires one camera and one laser sheet, placed perpendicularly. This layout limits the data gathered to tracer displacement within the laser plane. Moreover, particles that move out of the plane in the time between the image pair is taken will not generate any data. This setup is satisfactory for evaluating 2D and usually symmetric flow. Significant advancements, heavily supported technology, were made in order to be able to paint a more complete picture of a velocity field. Various non-intrusive, tracer based technologies, along with the type of data they generate, are displayed in Figure 3.2. Indeed, Planar PIV, labelled in the diagram as "*PIV*", the type of PIV introduced before, generates a 2D map of velocity in two directions. More advanced types of PIV like stereo PIV (two cameras and a light plane) is able to also generate a 2D map of the velocity in the third dimensions. Finally, when the plane of observation is widened to a significant thickness, the variation of all three velocity components can be resolved inside the volume of interest at any instant in which the data is gathered.

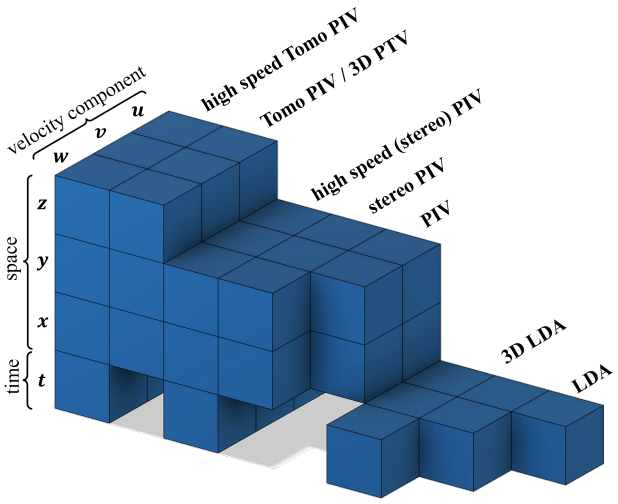

Figure 3.2: Evolution of non-intrusive flow visualization and measurement techniques and their ability to resolve certain velocity components and spatial and temporal derivatives. Adapted from [20] and [21].

It is this more advanced method, volumetric PIV [22], that has seen the most attention and growth through the development of true 3D particle tracking methods and tomographic PIV [23][20]. These methods provide the possibility to track individual particles in large 3D volumes which is useful for the study of large real domains without the use of scale models. Cross-correlated imaged produce a velocity vector for each interrogation window (capturing multiple particles) while particle tracking methods can produce a particle track which embeds velocity and acceleration for each individual particle. The removal of the spatial averaging of the

particle's velocity increases the effective data captured per image pixel. The ability to visualize the flow in large volumes, made possible by these technology and more advanced tracers it particularly suited to automotive applications considering the relatively large size of the vehicles. Perhaps the greatest feature of PIV is the ability to produce spatially-resolved velocity data which, despite being mostly of the averaged type, enables the identification of flow structures. This is crucial in automotive applications where managing and classifying air flows can only be achieved through a macroscopic visualization tool like PIV [19].

3.2. Image Processing: Shake the Box

The introduction of true 3D PIV technologies was possible also thanks to the development of more advanced processing algorithms. Indeed, apart from visual access and camera resolution, the main limit of PIV is the ability to correlate the data embedded in the digital images to velocity data. As the volume of interest gets larger, more particles may be in focus and the algorithms needed become more complex. The most widely used algorithm is the cross-correlation or auto-correlation algorithm. In simple terms, this computational process divides the two images of an image pair into smaller chunks, named interrogation windows and compares them with the image data at different locations of the image in the near vicinity. The algorithm is able, with statistical confidence, to evaluate the average particle velocity and direction in each interrogation window [24]. The main limitation of this process is that each of the image's pixels and each particle in each interrogation window does not produce a velocity vector while only one data point can be obtained for each interrogation window. For this reason, factors like particle size, fluid velocity and particle density determine the optimal smallest possible interrogation window size which yields data [17].

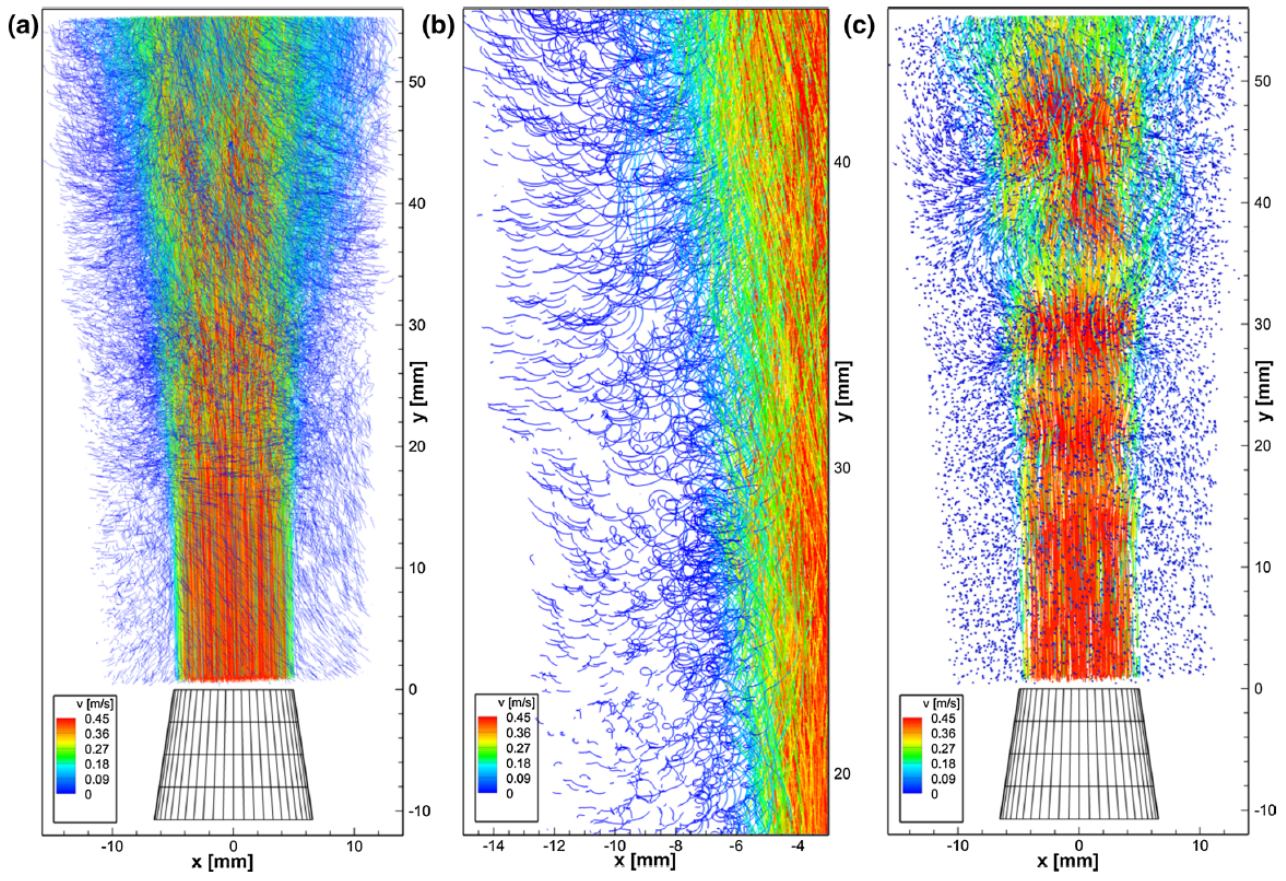

Figure 3.3: Particle tracks of a water jet, reconstructed by STB, extending for 100 frames colour-coded by streamwise velocity (a), detail of nozzle (b), single particle sith tail of 15 frames [3]

Ref. [3] proposed a new procedure to reconstruct the track of each individual particle in a large volume while maintaining high particle densities (up to 0.125 particles per pixel).

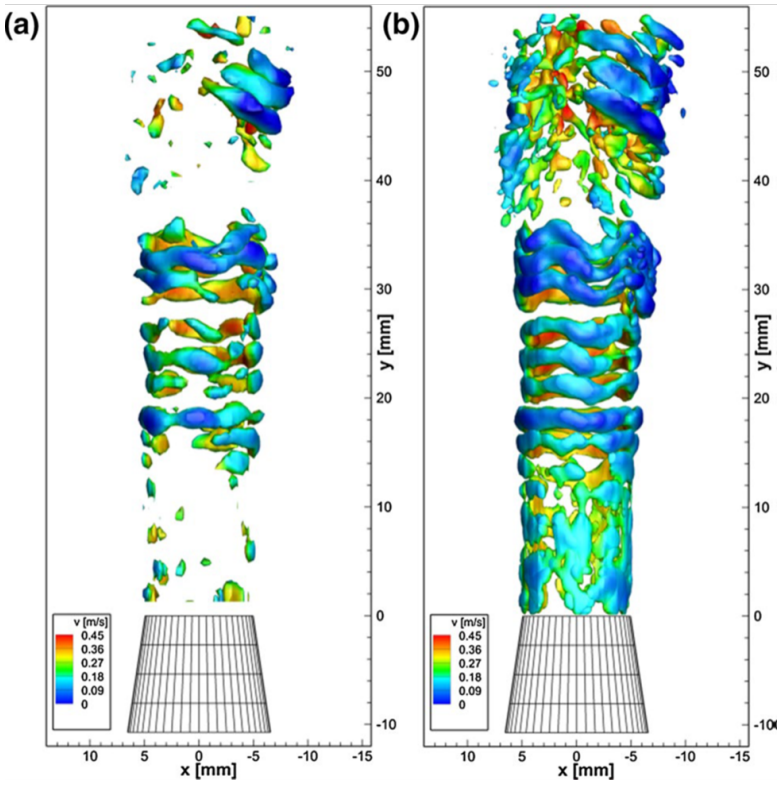

Figure 3.4: Isosurfaces of vorticity generated with TOMO-PIV (a) and Shake The Box (b) [3]

The presentation of this tracking method increased the accuracy of 3D-PTV and TOMO-PIV by a considerable amount by achieving a "nearly complete suppression of ghost particles" [3]. The presence of these particles is considered an important limitation of TOMO-PIV methods, especially at high particle densities due to their impact on the computed velocity field. Another large advantage of the method referenced, which itself incorporates advancements made in calibration, iterative triangulation and image matching, is the decrease in computation time by an effective reduction of iterations required for particle reconstruction. An example of the resulting particle tracks that this processing technique produces is shown in Figure 3.3. By further processing the scattered data to fit it to a cartesian grid through the process of "binning", Figure 3.4 shows isosurfaces of vorticity generated by processing the same images with TOMO-PIV and STB. It can be seen how yields a more detailed 3D map of vorticity.

3.3. Tracers: Helium Filled Soap Bubbles

Increasing the size of the the region of interest in a PIV experiment has been shown to be challenging considering the limits imposed by the reduced particle size of conventional tracers. Indeed, moving the camera further away to capture a larger region results in small tracers to reflect an insufficient amount of light in order to be distinguished from each other. Particles sized in the order of 1 µm such as industry standard fog/smoke particles are a viable option for planes of up to 900 cm^2 or volumes of 50 cm^3 [25] [26]. For this reason, a larger region of interest requires larger tracers with a more scattered light. The use of larger tracers brings a new set of challenges related to the buoyancy of the particle in the flow and to the fact that a larger particle disrupts the flow to a larger degree with respect to a smaller one.

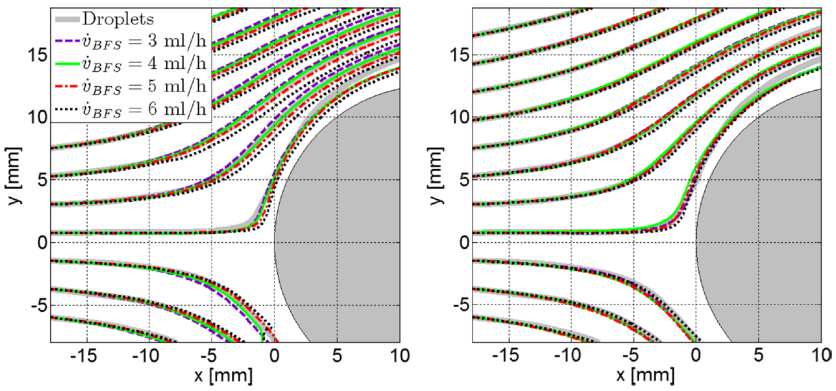

Figure 3.5: Averaged streamlines of air flow around a cylinder obtained from cross-correlation analysis of PIV images of tracers with different Bubble Fluid Solution (BFS) flow rates and two different Helium flow rates (left 4 l/h, right 5 l/h) [27]

The use of sub-millimetre naturally buoyant Helium Filled Soap Bubbles has been shown to be a valid alternative to fog particles as an enabler for larger scale tomographic PIV experiments [27]. Figure 3.5, depicts how the larger, naturally buoyant tracers compare to traditional fog droplets from in a wind tunnel experiment.

These particles take advantage of the positive buoyancy of Helium in order to produce large soap bubbles filled with the light gas through the use of nozzles. The specifically made nozzle, shown in Figure 3.6 can be adjusted with a different outlet diameter as well as soap, air and helium flow rates to produce consistently sized bubbles at the needed rate and location.

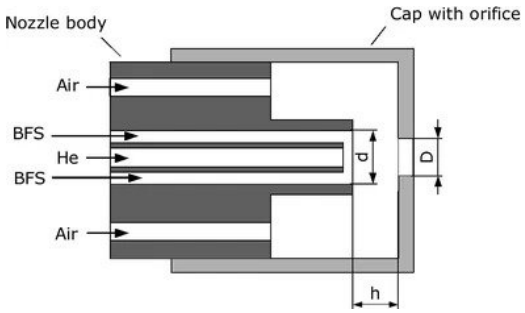

Figure 3.6: HFSB generator diagram [28]

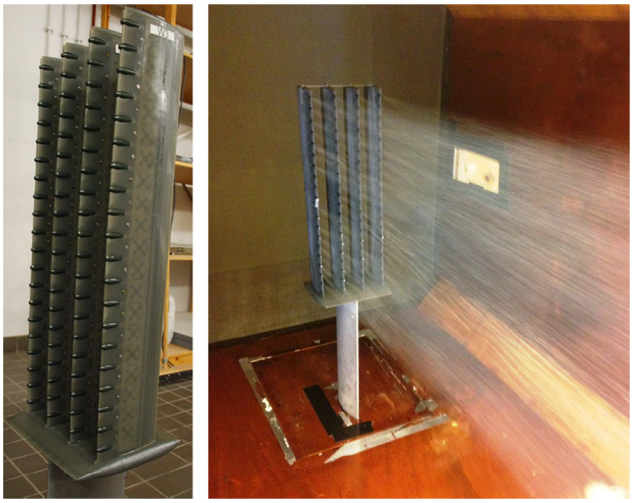

Figure 3.7: TU Delft's multi-nozzle seeding rake for HFSB generation utilized by Ref. [29]

3.4. Measurement Technique: Ring of Fire

One major objective of this research is to utilize Ring-of-Fire-style measurements in the specified automotive application, leveraging the increased realism gained by running vehicles in their natural environment, removing the use or need of rolling floors, boundary layer control or wind-tunnel corrections. The term "*Ring of Fire*", referring to a PIV measurement taken on-site, was first introduced by Terra et al [2] and literally alludes to the object moving through a high intensity light (fire) leaving behind a turbulent wake (ring). The aerodynamic measurement technique in question distinguishes itself from conventional wind-tunnel-based PIV measurements by removing the need of a wind tunnel and performing the measurement with a moving

object. In other words, the PIV setup is stationary like in a wind tunnel setup but it is the model that travels through stationary air rather than air blown around a stationary object, just like real vehicles do. The ROF setup utilized by [26] is shown in Figure 3.8.

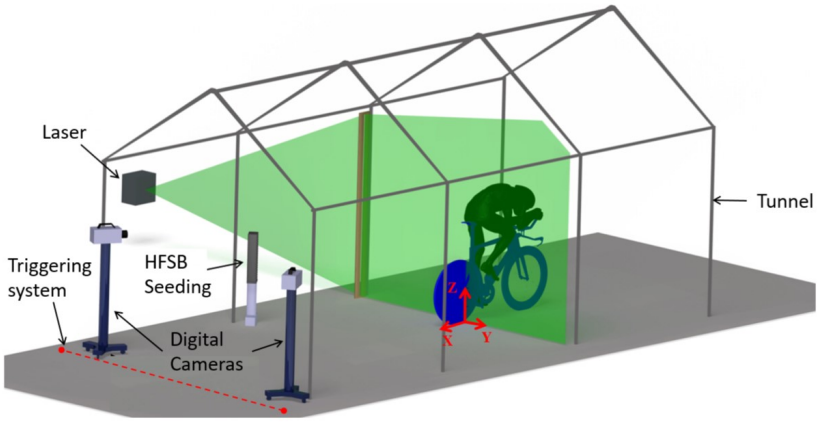

(a) Isometric view

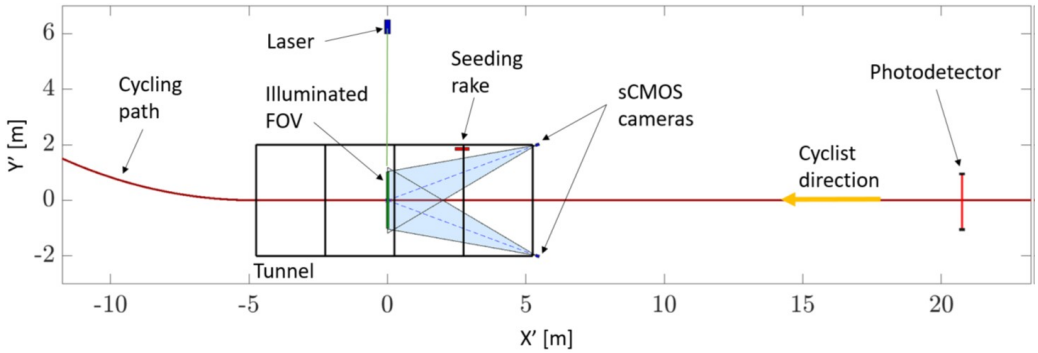

(b) Top view

Figure 3.8: ROF setup utilized by [26]

The principle of Ring of Fire aims to produce a much more realistic and possibly large-scale experiment using a real moving object. The use of a real moving object removes or reduces the challenges related to moving floors, multi-object interactions and curved path travel [2]. At the same time a few new challenges arise. These include: limitations related to the sensors that can be placed on the moving target [2], the uncertainty of the "flow conditions prior to the passage" and complications in producting homogeneous seeding with wind-tunnel optimized seeding devices [26].

In Ref. [2], the Ring of Fire measurement technique was utilized to evaluate the drag of a transiting spherical object by employing conservation of momentum in a control volume. Ref. [26] used it in a more applied context to study cycling aerodynamics through the use of a similar control volume approach to present the effect of different cyclist positions as well as the impact of drafting.

4

Objective & Research Questions

Starting from the goals generally in Chapter 1 and the literature review presented in Chapter 2 and Chapter 3, this chapter will re-focus the research objective by evaluating the research gap and define the leading research questions.

4.1. Research Gap

The literature review showcased a wide variety of studies concerning the effect of many geometry parameters of the diffuser. Complex geometries involving multiple channels and curved surfaces are often the object of research but they can be complicated to parameterize and are usually developed for ad-hoc applications. Therefore, studying the effect of curvature on the diffuser geometry may not produce many additional insights into the flow structure in the diffuser, especially through a novel experimental technique with unknown precision. Many authors constructed an experimental setup often utilizing a wind tunnel and rolling belt floor combination. The limitations of this configuration are size, optical access and an exponential cost increase associated with upscaling. Indeed, while some techniques may not require visual access at all, some, like PIV do. These have been used, with successful results on scaled Ahmed bodies.

As mentioned in Section 2.1, there is disagreement regarding which diffuser angle yields the highest downforce. In particular, [12] measured that the diffuser with the largest angle tested ($20°$) generated the most downforce while Refs. [9] and [14] found a downforce maximum at $\theta = 13°$.

Furthermore, considering the many obstructions (ground, wheels and the car itself) that hinder optical access to the flow under the vehicle, or the many simplifications that must be made, little research has been done on this region using PIV and more recent PTV methods. Interesting data was obtained ([11]) with experiments in a wind tunnel with a rolling floor by positioning cameras behind the car, inside the wind tunnel. However, employing more recent particle tracking technologies on wheeled vehicles in order to visualize the flow under the car hasn't been done before.

4.2. Objective

Considering the interesting gap in the research identified, the objective of this investigation is to take advantage of 3D PTV and Ring of Fire methodologies to characterize the flow in the diffuser of ground vehicles. In particular, identifying the mechanism of separation, how the diffuser affects the flow in the whole underbody region as well as quantitatively and qualitatively addressing changes in the flow structures between different diffuser geometries. Providing data-

driven answers to these goals would provide a different view on the existing problem to the academic community as well as showcase the potential of the technology introduced to be a valid substitute to other more established methodologies.

As discussed in Chapter 2, a wide range of flow characteristics can be replicated with relatively simple geometry changes. Therefore, it is proposed to keep the diffuser geometry simple and to choose a range of diffuser angles (θ) that are expected to show a variety of flow patterns (separation, separation bubbles, vortices, vortex weakening and breakdown). The length of the diffuser, its shape, the size of the side plates and the length and width of the flat floor shall be kept constant.

4.3. Research Questions

Specific technical research questions are defined here. These aim to narrowly define the important features of the research that will guide the design of the experiment and the study of the results. All research questions relate to an experimental campaign using a Ring of Fire style volumetric setup and a moving scaled car. LED light will shine the HFSB while the vehicle passes through the camera's field of view visualizing the movement of air beneath the car and inside the diffuser.

Diffuser geometry and flow characteristics

- *At which diffuser angle does flow separation occur?*
- *Which diffuser angle yields the highest downforce?*
- *How does the intensity of the counter-rotating pair of vortices in the diffuser vary when changing the diffuser angle?*

Convergence of results

- *How many runs are required for the average velocity field to converge with a rate of 2 %?*

Proof of concept setup and upscaling

- *What can be learnt by developing the proposed setup to benefit a future application on a motorsport vehicle?*
- *To what extent can the setup be upscaled to allow for a full-scale vehicle to be the subject of measurements?*

5

Experiment Setup

This chapter documents the design process of the physical experimental setup that was built and utilized in this project. First, a brief rationale to justify certain design choices is presented and then, the final design is described. The details regarding the steps taken to bring the setup to an operational stage and the routine followed in the data acquisition phase are described in Section 5.3.

5.1. Design Choices

The design of the experiment is based on the objectives of the experiment and the research. Therefore, some pre-determined requirements of the setup limit the design space. These are:

1. Obtain visual access to the inside of a car's diffuser.
2. Utilize PIV and PTV techniques on a moving vehicle.
3. Construct a scalable setup which can be quickly adapted to test larger/smaller ground vehicles or aerial vehicles in ground effect.
4. Provide a realistic testing space for vehicles in ground effect.

The experimental setup to be constructed features a multi-camera PTV system with LED illumination and HFSB tracers. Since the objective is to characterize the flow in the diffuser and underbody of vehicles, the particle tracking is performed within a large 3D volume. This requires a lot of light to be reflected by particles. Therfore, the combination of large-neutrally-buoyant Helium Filled Soap Bubbles and LED illumination is the obvious choice. Considering possible future iterations of this experiment with an upscaled setup, using HFSB and LED illumination is the best option. The test vehicle will traverse the measurement domain in a similar fashion as the Ring of Fire experiments described in Section 3.4.

Track layout A clear feature of the setup is a track or dedicated space where the vehicle accelerates. The track must allow for the vehicle to move on it freely while allowing cameras and sensors "see" under the car. An example of an elevated track featuring 4 cameras and 2 illumination units mounted underneath an elevated track is shown in Figure 5.1.

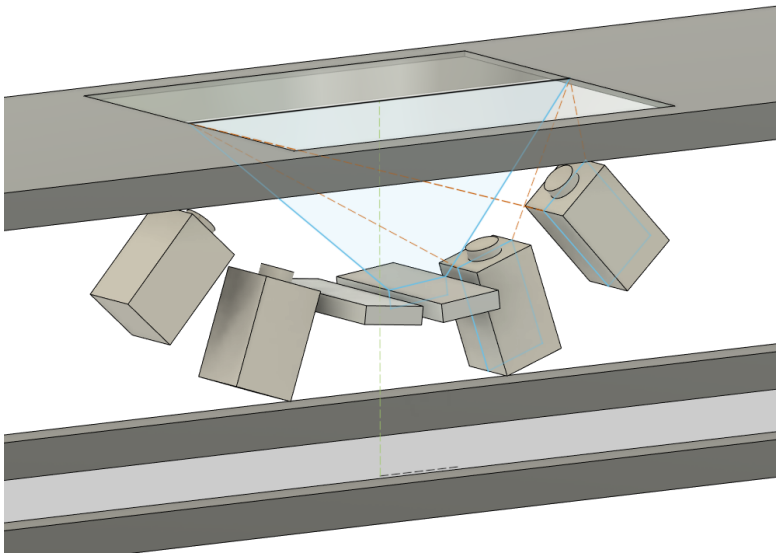

Figure 5.1: Preliminary experiment design with elevated track and viewing window

The most attractive option among those considered was the outdoor trench design where all equipment is placed underground while the car model travels on a pre-existing paved road. This option removes the need to construct a large dedicated and elevated track and concentrates the design efforts in the location where the measurements are taken. The outdoor placement of the setup reduces the space limitations that an indoor experiment would entail.

Vehicle type & size The features that characterize the optimal vehicle are: ready-to-drive capability, self-powered, size (larger preferred), speed (faster preferred) and availability. The criteria of speed and size are rather trivial as they connect with the scalability and realism setup features. Indeed, a larger and faster vehicle would yield a better Reynolds number similarity to full-scale race cars. Availability relates to the ease of access to the vehicle and the possibility of purchasing it or acquiring it within a timeframe in the order of weeks.

Narrowing down the options to a scaled Ahmed body, great for comparison to literature due to wide-spread use in existing literature, and an RC car, it was chosen to go for a relatively large RC car due to its realism (wheels, suspension and less blunt shape compared to an Ahmed body) and more challenging and complex mechanical build. In addition, an off-the-shelf RC car would also come packaged with a propulsion system. The details of the vehicle chosen will be listed in the next section.

5.2. Final Experiment Design

The design and construction of the experimental setup was a multi-disciplinary activity that was set to: provide visual access to the inside of a car's diffuser by placing multiple cameras directly under the moving vehicle, employ recently matured large-scale PTV and produce a scalable setup that can be readily adapted to test larger vehicles in ground effect. The PTV setup constructed has been designed so to gain unprecedented visual access below the vehicle by positioning the cameras in the ground, under the passing vehicle. The advantage of a field experiment where the vehicle moves is found in the realism associated with the observation of stationary air bending around a moving vehicle, impossible to test in a wind tunnel. This removes the need for ground-effect simulating devices such as rolling belts and the associated visual obstruction that these entail.

The facility built to enable this experiment is located on a 100 m paved stretch on the premises of the Flow Physics and Technology Laboratories of the Aerospace Engineering faculty of TU Delft in Delft, the Netherlands. The experiments took place at this location from the 22nd of November 2023 until the 4th of December 2023.

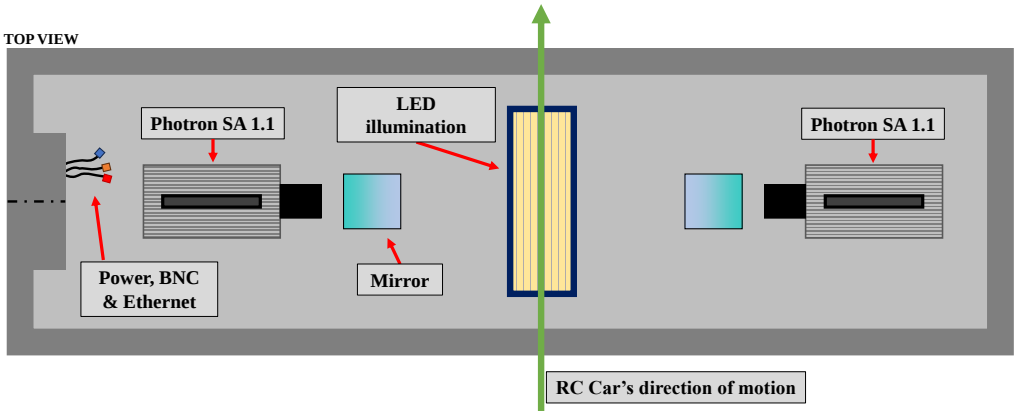

Figure 5.2: Top view of the experimental setup

The schematic side and top view of the setup are shown in Figure 5.3 and Figure 5.2. A concrete shell with an internal volume of 2 m (length) by 43 cm (width) by 40 cm (depth) was placed in the ground. These walls create the underground volume inside which the technical equipment is placed. Two Photron SA1.1 cameras and one LaVision LED light source are mounted inside the concrete shell. Each camera faces a mirror that allows them to view the same portion of the vehicle's diffuser through a transparent 12 mm thick polycarbonate sheet[1] while obtaining the correct focal length. The mirror layout allows the cameras to mount a 35 mm lens instead of a macro lens (short focal length) and achieve a square field of view measuring 20 by 20 cm at the location of the transparent sheet. The light cone from the LED illumination does not reach all 20 cm due to physical limits. The actual illuminated region was further limited to contain the size of the reflections in the images. The actual area (in plane with Figure 5.2) where particles are illuminated is 8 by 20 cm. The depth of field of the cameras, set at an $f_{\#}$ of 16, is larger than 10 cm, the field depth used for calibration. This $f_{\#}$ was chosen as a trade-off between the largest depth of field and sufficient light intensity to track particles. In addition, this depth of field ensures that particles are in focus also inside the diffuser with the "deepest" underbody height ($\theta = 20°$). With this setup, the field of view is insufficient to observe the full width of the diffuser and floor. The pilot-induced error which results in a slightly different passage position for each run allows to mitigate this limitation by effectively scanning the car passage after passage.

The cameras and light are powered and connected to a computer in the IRIS facility which serves as the control room. This building is situated just beside the road where the trench is interrated. The cables run underground, through a piping system, to reach the control room. The IRIS facility is also the host of the fluid supply unit generating the bubbles. The latter is connected to a Helium tank, an air compressor and a soap reservoir. These fluids run through pipes back to the point of measurement where they meet the bubble-generating nozzle.

The nozzle is mounted on a wooden box which serves as bubble containment as well as light shield. The face of the box in contact with the ground and two parallel sides are removed and fitted with roll-up curtains, forming a tunnel for the vehicle to pass through as shown in Figure 5.3. The wooden construction is a 3-sided C profile 50 cm tall and 120 cm wide

[1] $2140 \times 615 \times 12$ mm Lexan^{TM} Polycarbonate

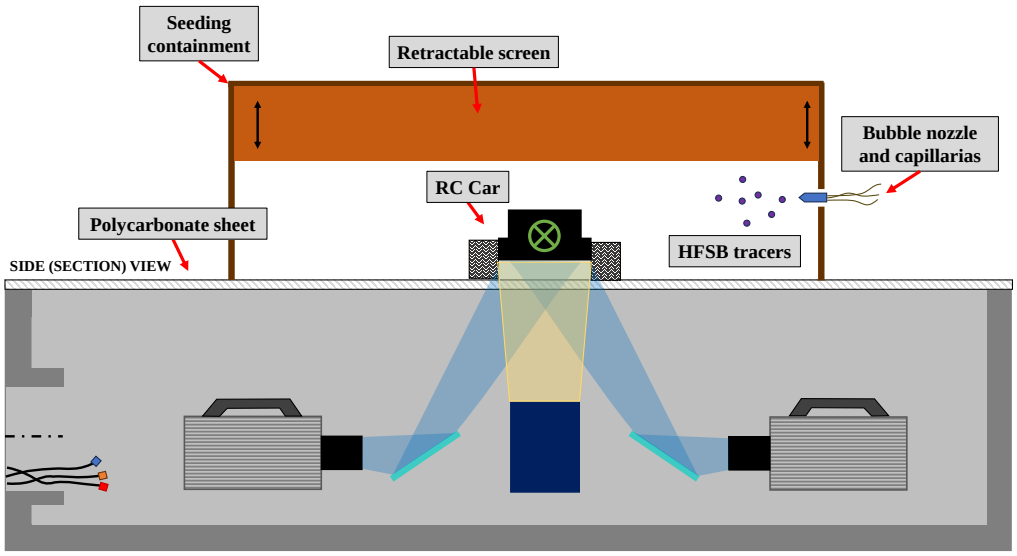

Figure 5.3: Side view of the experimental setup with annotated optical path through mirrors

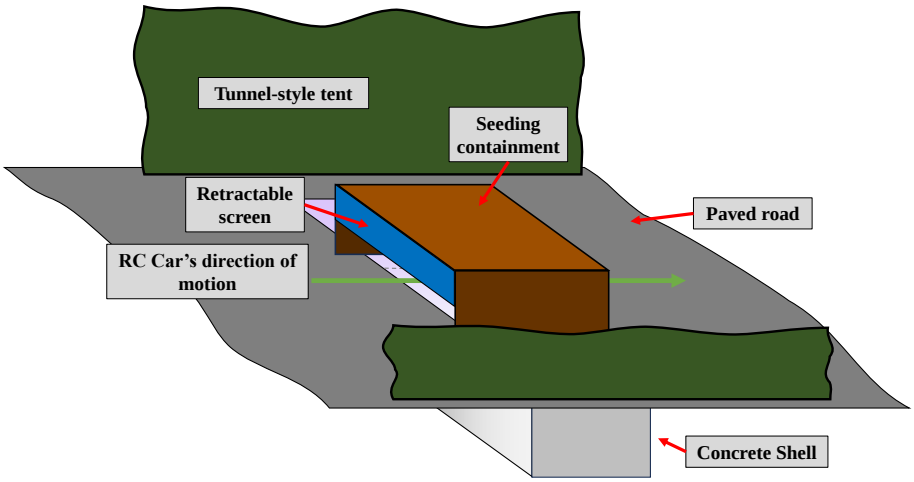

Figure 5.4: Global view of experimental setup

with a depth of 70 cm. Running the bubble generator for 1 minute is required to achieve the target bubble density of 1 bubble per cm^3. After tracers have accumulated sufficiently in this enclosure, the experiment can start and the curtains can be lifted to allow for contact between the air filled with bubbles in the wooden box and the moving vehicle. To further protect the measurement area from potential sudden water and wind gusts, a tent was erected around the measurement zone. When in operation, two of the sides of the tent remain open to form a large tunnel. The positioning of the tent, the containment box and the curtains relative to the underground concrete shell is shown in Figure 5.4. Figure 5.5 shows a real picture of the vehicle moving towards the measurement zone. In this figure, cabling from the underground light and cameras can be seen to exit a pipe on the right and enter the control room. The tent covers all equipment while the operator is busy opening the curtains to expose the illuminated bubbles inside.

The vehicle involved in the experimental campaign is a radio-controlled battery-powered high-performance scaled vehicle. This wheeled car is 505 mm long, 365 mm wide, 175 mm tall and weighs 2.5 kg. On flat ground, and with the 7.4 V battery, the vehicle was tested to be able to reach 15 m/s. With the more performance-oriented 11.1 V battery, the car is estimated to

Figure 5.5: Photo of RC car approaching measurement area

be able to reach 22 m/s. Overall, the test speed was limited on the remote controller to better control the position of the vehicle at the measurement zone and minimize bouncing. With this power limit, the average test speed was measured to be 6 m/s.

This vehicle was fitted with a custom-made 20 cm wide and 37 cm long flat floor on which four different 3D printed diffuser models could be mounted. Four 3D printed diffusers with side plates, 170 cm long and with varying angles (5°, 10°, 15° and 20°), were designed to be mounted and removed when needed to produce the necessary data. Figure 5.7(b) shows the vehicle painted and fitted with the 5° diffuser. A view of the flat floor, with three rows of white markers is shown in Figure 5.7(a). These markers are used in post-processing to track the speed and position of the car in order to align different tracks with each other. A more extensive view of the dimensions and assembly of the completed car is included in Appendix E.

The RC car chosen travels on the paved road for 20 m accelerating to 6 m/s. The road is covered with multiple 2 by 1m, 1cm thick plastic sheets which help smooth out the existing paved road. An aerial view of the acceleration path, control room and protective tent is reported in Figure 5.6. 40 cm before the car enters the field of view of the cameras (point of data collection), the RC vehicle trips a laser photodetector which in turn triggers image acquisition by the cameras. In the moments that follow, 300 pairs of images of the floor and diffuser of the vehicle are captured at 1000 Hz.

Reynolds similarity The realism of the proposed experimental setup, an important aspect of consideration, is addressed not only in terms of style of operation but also through Reynolds number similarity between the one that characterizes the experiment and the one of a full-scale racing vehicle. Considering the limited resources, reproducing the Reynolds number of a fast-moving full-size race car $[O^7]$[2] was not possible. The proposed setup targets Re in the order of $[O^5]$[3] and is therefore a good initial step in the right direction. The same setup could host a full-scale car with a characteristic width of 1.5 m travelling at 14 m/s, achieving a Reynolds number in the order of $[O^6]$.

[2]Based on a 2 m wide vehicle travelling at 80 m/s.
[3]Based on a 0.4 m wide vehicle travelling at 10 m/s

Figure 5.6: Aerial view of the control room, tent and track with annotated (red arrow) acceleration path of car

Additional considerations

- **Bubble density:** The target equilibrium (asymptotic) bubble density is 1 bubble for each cm^3. Managing this parameter in practice cannot be done quantitatively but has to be done by an expert observer through physical observation of the domain. It was found that 1 minute of continuous operation of the nozzle is sufficient to reach the target particle density.
- **Transparent cover:** The choice of material and thickness of the transparent cover that would allow the car to pass over while providing optical access has been extensively discussed. Indeed for safety reasons, a thicker plate is best. However, a thick sheet would reduce the amount of light transmitted and increase reflections. After obtaining the material properties datasheet of Lexan^{TM} (Polycarbonate) and Perspex (Plexiglass) and performing FEM simulations for the case of an accidental heavy-duty vehicle passage on the plate (see Appendix F), a Lexan^{TM} polycarbonate element 12 mm thick was chosen. The transparent top is unclamped and laid on the edges of the concrete walls (10 cm wide along the 4-side perimeter). In the end, the Lexan^{TM} sheet with the already mentioned dimension was chosen for its ability to withstand heavy loads without ultimate failure (large bending is not considered a failure).

5.2.1. Inventory

The setup described comprises many different components and essential connectors. Their quantity and description are presented in Table 5.1.

5.3. Testing Routine

A day of testing begins with a 2h preparation and calibration phase. The area of the experiment is cleared of debris, dust and any excess of water. Then, the cameras and light are lowered into the hole. These devices are connected to the underground power and data cables which have previously been routed through the pipes connecting the IRIS facility to the concrete trench. The beam on which the equipment is mounted on is aligned with dedicated marks on the floor to match the desired position. Back in the control room, an intensity calibration is done on the cameras along with a geometric calibration and a volume self-calibration. The geometric calibration is performed by snapping two pairs of images of the calibration plate (dotted sheet)

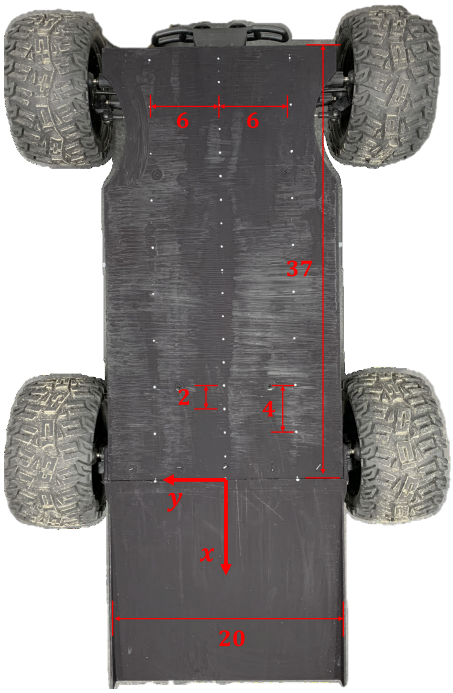

(a) RC Car floor and diffuser with annotated dimensions

(b) RC Car fitted with 5° diffuser

at different planes (xy planes at $z = 0$ and $z = 100$ mm). As the compressor and Fluid Supply Unit are switched on, the bubbles begin to fill the closed containment box and the volume self-calibration is done. Using Shake-the-Box, the calibration data is utilized to perform the particle tracking on a sample set of images to check for the correct functioning of the system.

As the system is operational, runs can be made and captured. Each of these takes about 3 minutes. In the control room, an operator sets the recording mode on DaVis. The second operator checks the seeding in the box and alerts the vehicle's pilot when ready. As the car begins its short journey, the second operator lifts the curtains by rolling them up fully. The car trips the photodetector triggering image acquisition. A view from inside the seeding containment box before the passage of the car and with the car in view is shown in Figure 5.8. The pilot then reverses the RC car back to its original position as the second operator closes the curtains to begin filling the volume back with bubbles. After briefly checking if seeding is sufficient and if the car is centred in the view, the acquired images are saved or discarded. The process is then ready to be repeated.

(a) **(b)** **(c)**

Figure 5.8: Bubble cloud in seeding enclosure after lifting the curtains: before the passage of the car (a), with the approaching car (b) and with car exiting the measurement region (c)

Following this procedure 20 times per diffuser angle allows for the generation of a sufficiently large set of images, that, when joined together, should form a statistically converged velocity

Quantity	Item
2	Photron SA1.1 Cameras
1	LaVision LED-Flashlight 300
1	Laser photodetector
7	BNC connector (2×Camera, 2×LED, 1×Photodetector)
2	Ethernet connector (1×Camera)
3	LaVision Power cables
1	Power extension
1	Assembled rail to mount LED and cameras on
1	Custom-made resin printed HFSB nozzle
1	Air compressor (max 8 bar)
1	Helium Bottle
1	Fluid Supply Unit (FSU)
2	Mirrors: front plated, 5 by 7 cm
1	Wooden 50 by 120 cm C profile for seeding containment: extruded 70 cm
2	Roll up curtains (mounted on the two open sides of the wood box)
1	Heavy duty tent: 6 m long with a cross-section of 2 by 2 m
10	Plastic road covering plates: 2 m long, 1 m wide and 1 cm thick
1	RC car: Maverick Quantum brushless
2	LiPo batteries
4	3D printed diffusers with $\theta = [5°, 10°, 15°, 20°]$ (technical drawings in Appendix E)
1	PC with DaVis software
1	Monitor
1	LaVision Programmable Timing Unit
1	Lexan^{TM} polycarbonate transparent plate: 2140 by 615 mm and 12 mm thick

Table 5.1: Inventory of experimental setup equipment

field. Since data from a single passage can produce a limited number of particle tracks, insufficient to fill the whole domain, patterns and important flow structures will likely be found and revealed only once the runs are averaged[4]. By comparing the results of this statistical analysis for different diffuser angles, conclusions will be drawn on the effect of the variation of this geometrical parameter (θ) on the flow behaviour in the underbody region of the vehicle.

[4]Multiple frames capturing the same portion of the car be can also be averaged to capture an already averaged field. This is possible after converting the tracks from the static laboratory frame of reference to the vehicle's moving reference frame.

6

Data Processing

This chapter describes the data processing activities that have been performed after the experimental campaign and the raw images have been stored. All data treatment steps between the images and final results chapters are shown in Figure 6.1.

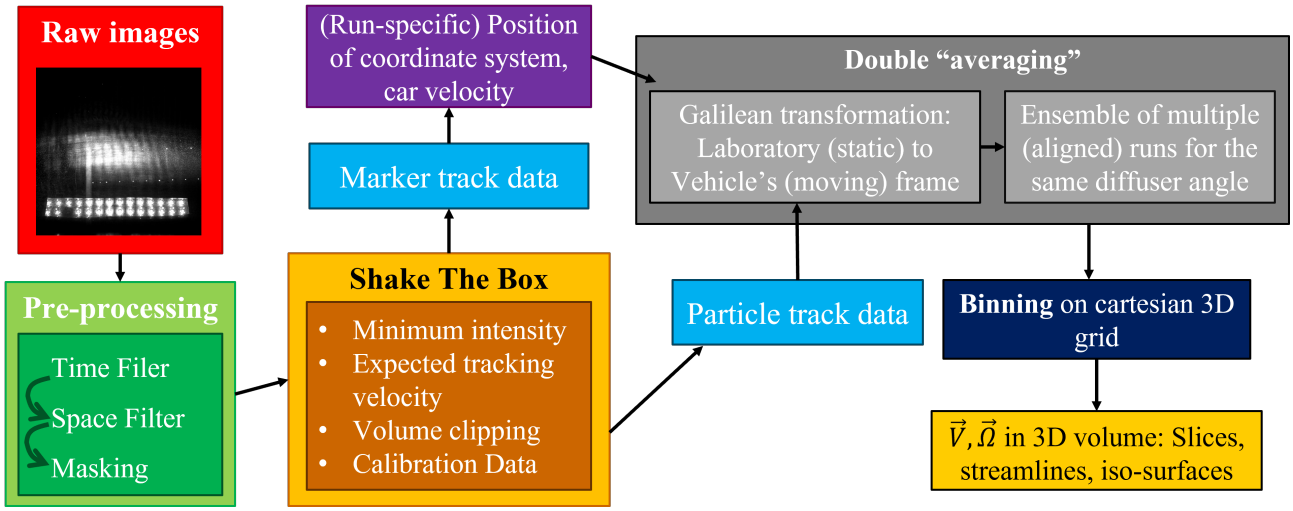

Figure 6.1: Outline of data treatment loop

The important phase generally termed "double averaging" takes place in two steps: a Galilean coordinate transformation and the merging of multiple (aligned) track files. Merging data from different runs and binning them together allows to mitigate run-specific issues related to seeding and passage position by effectively averaging the data from the available passages for each diffuser angle.

6.1. Pre-Processing

Before applying the particle tracking algorithm to the images to produce particle tracks, the images must be treated to increase the chance of particle detection and successful tracking by Shake-The-Box.

1. **Subtract Time-Filter:** The raw images present many artefacts which shall not be tracked. These include bubbles stuck on the glass surface as well as the light reflection on the glass. The built-in Davis function `SubtractTimeFilter` allows the user to select the number of frames over which an average is computed. This average of n frames is then

subtracted from each frame. This way, static objects become part of the subtracted element, disappearing from the final. The weakness of this process is that small vibrations induced by the passage of the car make stationary reflections or bubbles move by a few pixels. Therefore, after this type of processing, some pulsating reflections are left in the image. In general, this was not a problem as the reflections covered a part of the image which was anyway not sufficiently illuminated to detect particles. More importantly, real particles that are stationary may be involuntarily removed.

2. **Subtract Space Filter:** This process, also known as subtract sliding minimum takes care of removing large bright spots. This is especially useful for removing artefacts produced from the previous operation.
3. **Masking:** Some passages of the vehicle are offset to one side more than average. This makes the tyre occupy a large portion of the view. Since these runs still contain useful particle data, the images are cropped to remove the tyres. Leaving these images in full would lead to the tracking algorithm Shake-The-Box finding a large number of particle tracks where the bright tyres are seen. Removing these in post-processing is complicated and not very effective.
4. **Rotation:** There exist some runs with high particle density where the car passes at a high angle. This occurs when the car's motion is not managed precisely and it crosses the measurement domain travelling sideways with a velocity $v \neq 0$. Tracking the markers allows for this passing angle to be computed and to correct all particle tracks by applying a spatial rotation transformation.

The result of these operations on one image is reported in Figure 6.2.

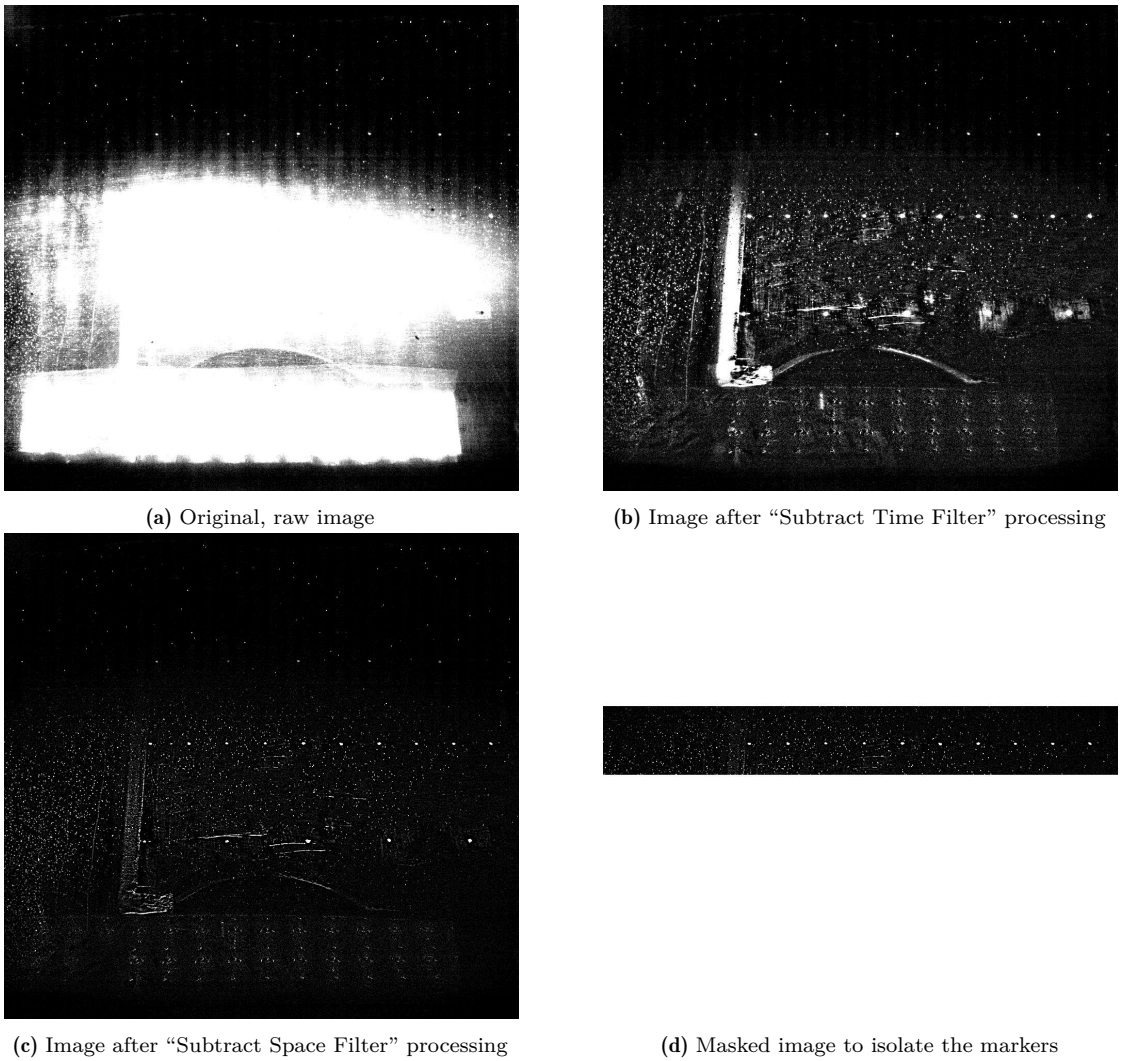

(a) Original, raw image

(b) Image after "Subtract Time Filter" processing

(c) Image after "Subtract Space Filter" processing

(d) Masked image to isolate the markers

Figure 6.2: Images from frame 130/300 of camera 1 for passage number 8 of $\theta = 20°$ after successive pre-processing steps featuring the same intensity scaling ("colormap" range)

6.2. Particle Tracking with Shake-The-Box

The actual particle tracking is the main processing phase of the data of the experiment. The particle tracking velocimetry (PTV) processing with Shake-the-Box is performed in the Davis environment. Here, the most important parameters of Shake-the-Box are discussed.

- **Volume:** The function requires three spatial ranges (one for each dimension) inside which to attempt to track particles. These are fixed for each testing day as they are limited by the volume used for the geometric and volume self-calibration.
- **Intensity Threshold:** Like all images, the raw data includes non-negligible noise levels. For this reason, it is important to specify a minimum intensity, in counts, that the program can interpret as a particle. Everything below this threshold will be discarded. For reference, markers have an intensity of around 1000, particles in the center of the view of 200 while particles away from the center or farther deep in the volume can range between 50 and 100 counts. Occasional bright spots due to reflective paint, water droplets and light reflections can span the whole dynamic range of the camera. For this reason, these shall be removed as best as possible with image pre-processing. Selecting a threshold is a compromise between tracking few particles with little or no outliers and tracking a lot of particles with many outliers.

- **Tracking velocity:** Perhaps the most important setting parameter, this control allows the user to exclude particles that do not fall within a certain velocity range. This is useful to remove outliers or bad tracks of noise or other non-particle elements. These velocity ranges are set by specifying a mean velocity in all 3 dimensions along with an allowed delta from this mean that tracked particles can travel at. A mistake in this field would compromise the data by clipping all particles outside the velocity field. Again, this parameter is a compromise between allowing all particles and restricting the domain dangerously close to the edge of clipping. The balance was found with $u \in [2 \pm 5] = [-3, 7]$ m/s, $v \in [0 \pm 4] = [-4, 4]$ m/s and $w \in [0 \pm 3] = [-3, 3]$ m/s. In practice, this setting was used as a preliminary outlier removal tool.
- **Advanced settings:** There exist more advanced settings that have been tweaked by analyzing test tracks. These all attempt to increase the number of tracked particles.
  - Multi-passes was set to 3. This makes the algorithm perform the tracking multiple times, both from frame 1 to 300 and backwards to "catch" particles that would otherwise not be tracked.
  - Maximum relative particle shift was increased from 20% to 30%. Maximum absolute particle shift was increased from 1 to 2. These settings attempt to increase the detection of particles that feature high accelerations. These are especially important in the wake and in separated regions where sharp velocity changes (magnitude and direction) are expected.

The outcome of the particle tracking algorithm is shown visually in Figure 6.3. The chosen frame shows the tracked bubbles before the passage of the car (slow-moving, blue cloud) being struck by the model car. In this visualization, the red, high-speed tracks are not real particles but belong to the car's front bumper and markers. The evenly spaced row of red tracks represents the tracked markers and their position can be used to locate the car in 3D space. Since the car occupies a large portion of the domain, the only tracks that can be seen after and through the car's passage are the blue (negative u) particles that therefore exist under the floor. It is this set of particles that represent the most interesting aspect of this experiment.

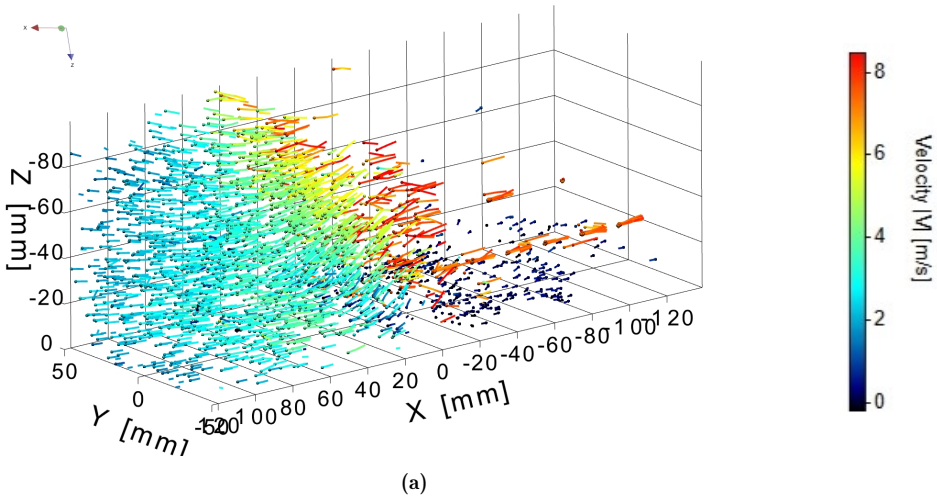

(a)

Figure 6.3: Particle tracks color-coded by streamwise velocity plotted on original axis as output from DaVis

The actual track data for one full run consists of a large text file containing 300 zones, one for each frame, each including a row for each particle that is successfully tracked in that frame. Each particle has an associated, run-unique track ID along with all positional and velocity

information. Data from one run can occupy between 50 and 200 Mb with a typical number of lines in the order of 500'000.

```
TITLE = "5 deg Run 1"
VARIABLES = "x" "y" "z" "Vx" "Vy" "Vz" "|V|" "trackID"
ZONE T="Snapshot 0000"
29.2798 -4.4402 -29.1171  6.6634 -2.6744  0.1053 7.1891 1
45.5607  3.0590 -16.9270  5.9040  0.4678  1.6653 6.1527 2
51.6562 -3.8666 -25.0296 -0.1442 -3.7111 -2.3174 4.3767 3
ZONE T="Snapshot 0001"
35.6215 -6.3210 -29.0565  6.0208 -1.0877  0.0158 6.1174 1
50.8283  3.0951 -15.3255  4.6316 -0.3957  1.5375 4.8574 3
51.2035 -7.5089 -26.8372 -0.7614 -3.5385 -1.2975 3.7724 4
```

The structure of these files is as shown in the text extract above. Here, 3 particles are found in the first timestep (see `trackID` in the example). Particles 1 and 3 are successfully triangulated in frame 2 leading to a particle track.

6.3. Galilean Transformation

A Galilean transformation is used to translate positional data in multiple dimensions from a static frame of reference to a moving frame of reference or vice-versa. This is a needed process for this application in order to represent data in a more intuitive frame of reference which makes drawing conclusions and making observations easier. In addition, charts and plots from literature are commonly expressed in a static, laboratory, "wind-tunnel-like" frame of reference. Conforming to this norm is crucial to make accurate and insightful comparisons.

In this case, the static frame of reference, referred to as the laboratory frame, is the frame, set during the calibration of the equipment in the DaVis software (X'). The actual position of this coordinate system is not important as the transformation is necessary in any case. The moving frame of reference is located on the ground, just below the last marker before the start of the diffuser and moves together with the vehicle at a speed equal to it. This will be referred to as the vehicle's moving frame of reference (X). This coordinate system is placed at ground level rather than on the marker itself due to the sometimes unpredictable motion of the car in the z direction. The definition of the z axis coincides with the one of the laboratory frame of reference where tracks are defined. The vehicle's frame entails a constant, measurable velocity in the x direction which equals the velocity of the markers, and so of the car, for each run. This is the same speed used to normalize the velocity data in each run before the merging process. The x direction is also flipped between the laboratory and the moving vehicle's frame of reference. This was done to align positive x with the (converted) flow direction.

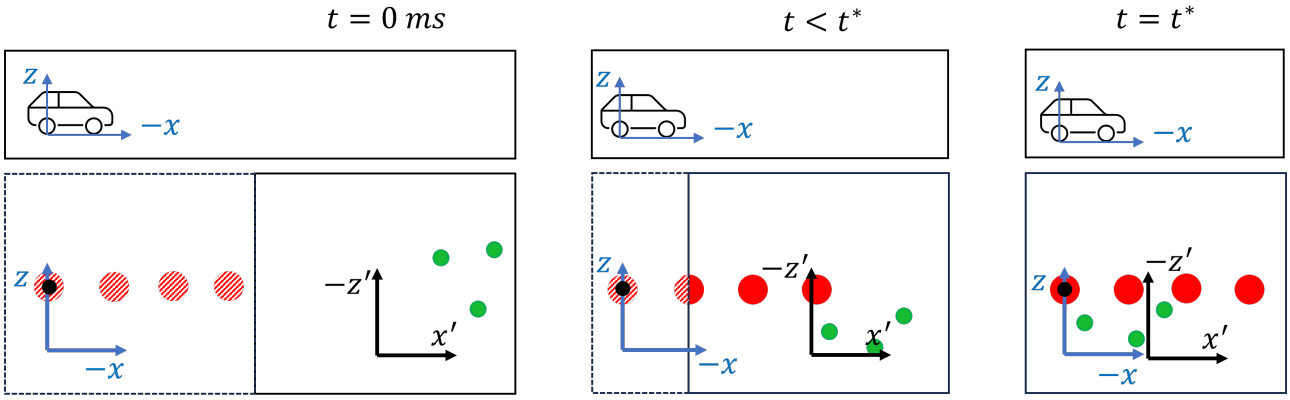

Figure 6.4: Schematic of tracked markers at different times including the relative positions of the frames of reference X and $X^{'}$

Figure 6.4 graphically shows the relative position of the two frames of reference in three sample snapshots. Due to the fact that the field of view is limited, the position of the translating coordinate system cannot be obtained already at t=0. A key snapshot t^* is therefore introduced. By animating the tracks of the markers (red circles in the diagram), it is possible to identify a snapshot where the last marker on the car's floor, and so the coordinate system, is clearly in view. Due to the limited field of view and even more restricted region where particles and markers can be tracked, some runs only allow for the tracking of the side rows of markers. The "sideways" offset y_o is therefore used to obtain the location of the last central marker, the vehicle's frame origin, when the latter cannot be obtained directly. This offset is −60 mm when the tracked markers belong to the right row, +60 mm when they belong to the left row and +0 mm when the central row of markers is tracked.

$$\begin{aligned} -x &= x^{'} - x_m^* - u_m(t - t^*); \quad y = y^{'} - y_m^* - y_o; \quad z^{'} = z \\ -u &= u^{'} - u_m; \quad v = v^{'}; \quad w = w^{'} \\ t &= t^{'} \end{aligned} \tag{6.1}$$

By considering the position of the markers at this time (t^*), and their velocity in the x direction (u_m), the definition of the vehicle's frame of reference can be drawn as shown in Equation 6.1. Here, $x_m(t)$ is the position of the last marker in the laboratory frame of reference. Its position at the key frame is x_m^* ($x_m(t^*) = x_m^*$). For clarity reasons, reference to the time dependence of x, $x^{'}$, y, $y^{'}$ etc. is omitted. These should read as $x(t)$, $x^{'}(t)$, $y(t)$ and $y^{'}(t)$. The variable u_m, x_m^*, y_m^* and y_o are constants and therefore not time-dependent. This formulation makes the two coordinate systems differ by a simple translation of $[x_m^*, y_m^*]$ at $t = t^*$. This shift would be [0,0] if there would exist a snapshot where the two coordinate systems would overlap (last marker passes through laboratory frame origin). This is possible but unlikely to be captured. The velocity u_m is the average speed in the $x^{'}$ direction of the markers as captured in one run. An average of 6 markers are visible for 50 snapshots, leading to a total of 300 velocity data points per run. Averaging the available velocity of the tracked marker tracks produces an accurate estimate of the velocity of the car itself.

In practice, the routine that enables this transformation starts by obtaining the 3D coordinates of the last marker at t^*: $\vec{X_m}(t^*) = [x_m^*, y_m^*, z_m^*]$. As explained before, three rows of white, reflective markers are painted on the vehicle's floor. The rear-most marker of the central row coincides with the origin of the vehicle's frame of reference ($\vec{X_m}(t^*) = \vec{O}(t^*)$).

Next, the (x) position of the vehicle's coordinate system, defined in the laboratory system,

is found at $t = 0$ to be $O_{x,t=0} = x^*_m - u_m t^*$. The y coordinate of the vehicle's coordinate system extrapolated at $t = 0$ equals y^*_m since the vehicle's motion does not affect this axis ($O_{y,t=0} = y^*_m$). The sideways offset discussed is added or subtracted when necessary. This step is done to avoid defining the coordinates of the particles in the vehicle's frame of reference (x, y, z) with the run dependent t^* inside the processing loop. u_m is also run dependent but it is more easily retrieved and kept track of. This also makes the frame definition (x) more intuitive: $-x(t) = x^{'} - O_{x,t=0} - u_m t$. After obtaining the translation data, all tracked particles of a run are processed with this translation. These simplifications lead to the definition of the particle position and velocity with the constant origin position at $t = 0$, t and the vehicle's speed as shown in Equation 6.2.

$$\begin{aligned} -x(t) &= x^{'}(t) - O_{x,t=0} - u_m t; \quad y(t) = y^{'}(t) - O^{'}_{y,t=0}; \quad z(t) = -z^{'}(t) \\ -u(t) &= u^{'}(t) - u_m; \quad v(t) = v^{'}(t); \quad w(t) = w^{'}(t) \\ t &= t^{'} \end{aligned} \tag{6.2}$$

The code implementation of this procedure is included in Appendix A. Dedicated functions locate and separate the data blocks of each timestep, obtain the position of the markers at t^*, extrapolate the position of the coordinate frame `cys_t0` at $t = 0$ and estimate the vehicle's velocity `Vx_car`. Inside the loop, the actual array of variables for the current time step is found. After, the coordinate system transformation and the outlier removal are performed.

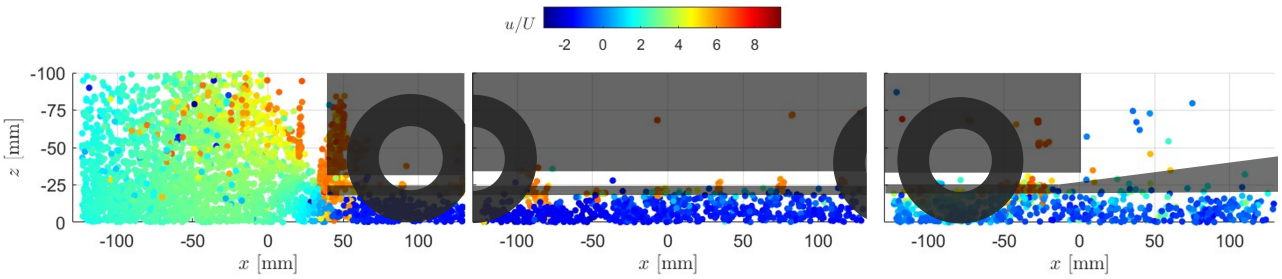

(a) $t = 110$ ms **(b)** $t = 145$ ms **(c)** $t = 180$ ms

Figure 6.5: Particle data of three snapshots in the laboratory frame of reference

Three snapshots of the tracked particles in the laboratory frame of reference are shown in Figure 6.5 as seen from the side (xz plane). Reflecting the static nature of the cameras, the size of the field of view is fixed between $-120 < x < 120$, while the car is seen to move through the domain from right to left. The simplified shapes superimposed on the particle data show the tires, the flat floor and the diffuser at the rear of the car. The three frames capture the front of the car striking the could of static[1] particles (Figure 6.5(a)), the car in the middle of the camera's field of view with many particles under the car moving opposite of the car (Figure 6.5(b)) and car's rear and diffuser leaving the camera's view (Figure 6.5(c)). When converted and joined together, these three frames form the particle cloud shown in Figure 6.6. The orange cloud of particles in Figure 6.5(a), represents tracks of the front of the car and markers travelling at the speed of the car ($\sim$ 6 m/s). After the conversion, these particles appear stationary in the vehicle's frame of reference (Figure 6.6) and are characterized by a light blue colour ($u/U = 0$). Due to the nature of the transformation, the last marker, matching with the start of the diffuser, is located at $[0, 0, 0]$.

[1]Particles are initially static but as the car approaches, the moving high-pressure wave in front for the car leads to a gradual acceleration of the particles in the direction of the coming car, before its physical arrival.

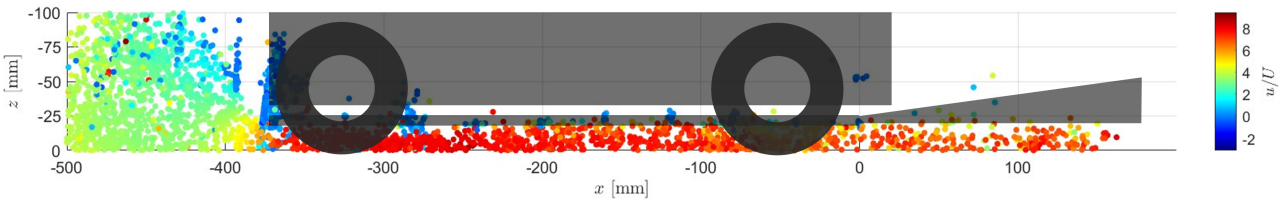

Figure 6.6: Particle data of three snapshots in the vehicle's frame of reference (converted position and velocity)

The result is a data file where the time dimension has been converted into space. The original data blocks relating to each frame or snapshot have no value anymore and all particles can be joined together in one large cloud of particles that fill the entire volume where bubbles were able to reach as the car passed. In other words, the passage of the car creates a panorama-like effect as the cameras "scan" the vehicle in motion. Data is now arranged in a single snapshot where particles fill a volume much larger than the actual field of view as shown in Figure 6.6 and Figure 6.7. Here, green particles originally from different timesteps are joint together to complete a complete particle cloud for one passage.

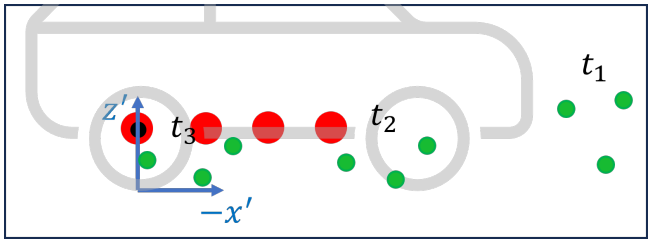

Figure 6.7: Data from multiple timesteps joint in one frame after the Galilean transformation

Note on units The actual data is not ordered by time but by snapshots. These are separated by a time step Δt equal to $1/f$ where f is the acquisition frequency of the data: 1000 Hz. This implies that the real-time interval between each snapshot is 1 ms. Therefore, the snapshot count s can be used as time variable t measuring time in milliseconds and are interchangeable. The tracking and data acquisition software DaVis outputs spatial coordinates in millimetres (mm) and velocities in meters per second (m/s). In the coordinate system definition shown in Equation 6.1, x, x_m^* are expressed in mm, u_m in m/s and t in ms (10^3 m = m/s $\times$ 10^3 s).

Velocity scaling Adjusting the position of each particle with this transformation also takes care of scaling and aligning the tracks from passages where the car passed with a different velocity. The main assumption concerning the passage of the vehicles is that acceleration is negligible and that the car moves in x only. This means that the angle between the x axis and the real vehicle's velocity vector is assumed to be 0°. In reality, this angle was measured to range within ±2° for most runs. In cases where the angle was larger than this threshold, the data was subject to a rotation operation or discarded altogether.

Cross-run averaging The second average type which completes the "double averaging" is carried out by simply joining all particle clouds for each run of a diffuser angle. This procedure was made possible by the transformation explained in this section.

6.4. Outlier Detection and Removal

The particle tracks that DaVis outputs include many wrongly tracked particles that should not be mixed with "real" tracks. These arise from reflections on the car's floor, reflections on

the glass, static bubbles stuck on the glass, triangulation errors leading to ghost particles, and tracks of non-bubble objects. These "fake" tracks are particularly numerous in this experimental campaign due to the use of two cameras only. The addition of another camera would help remove some of these particles by providing a third viewpoint to the particles.

As mentioned at the end of Chapter 5, each run's file entailed around 500'000 rows representing the same number of particles distributed over all the available frames. The effect of the outlier removal process can be quantified by observing that the file size and the number of particle rows decrease by 40% in "good" runs[2] and up until 70% in runs with lots of tracks linked to reflections and non-bubble objects.

- **Markers and car appendices**: These non-bubble tracks are removed by considering the known velocity of the car for every run. In the transformed data set, these tracks are stationary. In the portion of space domain that the car occupies, the real tracers find themselves in the floor region. Ignoring the insignificant particles that would track fully reversed or stationary particles in the boundary layer of the floor, it is not physical that particles in this region would be stationary. This makes the removal of these outliers quite trivial.
- **Stagnation cloud**: In the portion of the flow upstream of the car, the tracks form a homogeneous cloud with easily predictable and visible slow-down patterns. Due to triangulation errors in this high particle density region, there exist many "fake" tracks with high velocity in all directions and erratic behaviour. These are removed by imposing a maximum velocity limit in all directions in this portion of the domain.
- **Tracks crossing surfaces**: There exist some tracked particles that occupy the inside of the car or are above the diffuser. These cannot possibly have been captured by the cameras as the car hinders visual access to these regions. These tracks are removed by considering their position with respect to the position of the car and the diffuser (different geometry angles are accounted for). To account for the moving of the vehicle through the run, especially, in the z direction, the boundaries have an offset compared to the real edges of the car.

These conditions, which are implemented in the code snipped presented in Section 6.3 are formulated mathematically as shown in Equation 6.3. Spatial coordinates are evaluated when measured in mm while velocities in m/s.

$$
\begin{aligned}
&\texttt{Flag particle IF} \\
&\qquad (u < U_{floor} \quad \texttt{AND} \quad -380 < x < 20) \\
&\texttt{OR} \quad (u < U_{stag} \quad \texttt{AND} \quad x < -380) \\
&\texttt{OR} \quad \left(\frac{-z-25}{x-10} < tan(\theta) \quad \texttt{AND} \quad |y| < 100 \quad \texttt{AND} \quad 10 < x < 180\right) \\
&\texttt{OR} \quad (-360 < x < 10 \quad \texttt{AND} \quad -z > 25 \quad \texttt{AND} \quad |y| < 100)
\end{aligned}
\tag{6.3}
$$

The first and second conditions take care of removing the front bumper and marker-related tracks respectively. The two different speed thresholds are necessary (U_{floor} & U_{stag}) since the separation between real and outlier tracks is larger or smaller thus allowing for a more aggressive cutout distinguishing outliers. For instance, marker-related tracks are characterized

[2]In this context, a good run presents a large number of "true" particles and little to no outliers or tracks of the car. Generally, the passage of the car in these runs is well-centred so that only the floor, diffuser, markers and bubbles in these regions are visible.

by speeds close to $u = 0$ while airflow underneath the floor is much faster ($u > 1$) throughout the whole range where this condition is active. On the other hand, in the stagnation cloud, the particles show different speeds ranging from close to $u = 0$ up to $u = 1$. For this reason, in the stagnation cloud, the threshold is more relaxed to prevent the removal of real tracks. The last two conditions take care of removing particles above the diffuser and floor respectively.

An important feature of this outlier detection tool is that rather than flagging the single particle data row, the tool retrieves the track ID to which the outlier particle belongs and then proceeds to remove the whole track by deleting all particles with this track ID. This is useful for those tracks that for instance cross the diffuser surface (third condition) and present a portion in the unphysical domain and another in the physical one.

6.5. Binning

After the outlier removal script is run and the joining particles for all available runs for a diffuser angle, the scattered data must be interpolated on a Cartesian grid for easier exporting and analysis. This procedure is the objective of the "Binner" software [30]. In this context, binning refers to a type of 3D barplot-style grouping of the tracks according to their spatial coordinates.

The program used was initialized with the following settings:

- **BinSize:** The main parameter of the program, BinSize, sets the dimension, in mm, of the 3D bin and so the 3D mesh on which the scattered data will be interpolated. This variable was set to 15 mm. Smaller binsizes are able to resolve smaller flow structures but potentially lead to data loss since there may not be enough particles in the resulting smaller 3D volume to fit data. The selected value is therefore the tested minimum value that yields a large volume of valid bins.
- **Overlap:** To increase robustness, an overlap of 75% between bins was set. This leads to an effective vector spacing which is below the set binsize of 15 mm. With the mentioned settings, the vector spacing becomes 3.75 mm.
- **Minimum particle count:** Due to the scattered nature of the data, there exist some regions where few or no particles exist. By setting this parameter to 1, one particle is enough to generate a valid data-filled bin in the mesh. Excluding data points generated from just a few particles is done in the software used to generate the figures.
- **Ensemble averaging mode:** This parameter controls how the variable's values of each bin is found from the particles that belong to each of these bins. By selecting `linear`, a linear fit is done on the data of each bin and then saving the solution of the linear fit at the centre of the bin at the bin's location.

6.6. Further Processing

These extra steps are part of those data processing activities used to manipulate the data to produce coherent plots, more robust visualizations and clearer plots.

Blanking When displaying results, all cells that have an associated "number of particles" below 5 are "blanked": not shown. The number of particles variable associated with each mesh cell represents the number of particles used for binning and so to obtain values for velocity and acceleration. In Section 7.1, the variation of particle count throughout will be shown visually.

Slice averaging When displaying slices, the simplest and most direct way to present the data is by showing the variation of the desired variable on the mesh cells at one specific x, y or z coordinate depending on the type of slice shown. Displaying such slice may be useful to show the trends in the direction perpendicular to the slice when paired with other slices but on its own, it may be dominated by local fluctuations caused by noise and unsteady structures. Even if the binning process effectively averages variables within a small volume (3.75 mm sided cube), local unsteady fluctuations that have a characteristic size just above this bin cube may still remain visible in a slice generated by a plane of data vectors. Averaging the data on all available parallel slices normal to one of the major axes is not a possibly since important trends in the slice's normal direction are averaged out. For this reason, many of the slices shown on their own are obtained by averaging 5 neighbouring slices. This allows to average out noise and unsteady fluctuations that do not help to characterize the flow while still capturing the macroscopic flow variations within the slice and in the direction perpendicular to it. In the case of a slice that cuts the vehicle in half longitudinally ($y = 0$), the slices to be averaged for this visualization belong to the region $y = 0 \pm 1$ cm. Considering that the diffuser is 20 cm wide, this equals to 10% of the total width.

Surface plot of velocity and pressure Utilizing simplified flow equations and a few assumptions, it will be shown that an approximate curve for pressure on the underbody's surface's centerline can be obtained. This was done to attempt to replicate this common type of visualization that connects well with the actual force generated by a body. First, 5 slices around the midplane of the vehicle are obtained and averaged. The 2D meshed data can then be linearly interpolated on an arbitrary probing line. Due to the way the simplified equations work, viscosity is not accounted for. Therefore, the data processed must be outside of any boundary layer and turbulent areas to yield the best results possible. The probe line chosen, on which data is obtained, is the centerline of the 2D duct formed between the underbody's profile and the ground ($z = 12.5$ mm, $y = 0$ mm, $-370 < x < 180$ mm).

6.7. Data Presentation and Extraction of Results

The experimental campaign and data processing phases produced four large 3D volumes where variables are stored on a $69 \times 607 \times 29$ ($\sim 1.2 \times 10^6$ points) grid. These variables include x, y, z, u, v, w, a few derived variables such as vorticity[3] and data quality indicators like np, the number of particles in each cell. Slicing, tracing, plotting and sectioning this data set in order to characterize the flow and answer the research questions is the end result of this investigation.

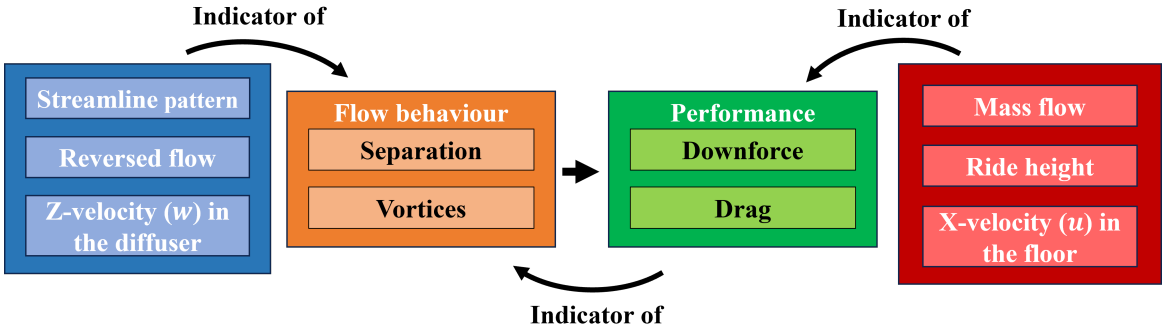

Figure 6.8: Logical chart of performance and flow indicators

[3]Although technically easy to obtain or readily available, these variables were not used to support discussion as they did not provide strong patterns and observable trends.

Concerning the "Flow Behaviour" aspect, separation and vortices are the main features expected. Separation is the mechanism by which the fluid flow detaches from the surface. This introduces drag forces as well as inefficiencies in aerodynamic devices such as wings and diffusers. Indeed, due to the fact that separated flow does not follow surfaces, the effective shape of wings and diffuser changes in an uncontrollable way. From a vehicle's point of view, a separation bubble in the diffuser would result in a pocket of low-pressure air which would pull the vehicle backwards (drag).

Vortex-like structures are key to the flow behaviour of the diffuser as seen in Section 2.1. The direct effect of the presence of these structures is an added sealing effect to the diffuser which helps to maintain low pressure inside the diffuser volume. These are harder to detect using the indicators listed above. These indicators are particularly useful due to the fact that the experimental technique used entails a weakness with respect to the visualization of separated flow. Indeed, PIV and PTV require tracers, the bubbles, to reach a specific 3D location for data to exist in that location. The nature of separated flow is characterized by a lack of motion in the separated region. For this reason, observing where data is available and where it isn't can also provide insights about possible regions of separated flow. The fact that the vehicle "strikes" a small volume filled with particles only worsens this effect. Indeed, the transient motion of the car does not provide the time necessary for fresh tracers to be sucked into separated regions and produce data at these locations.

The following properties have been identified to be key in describing the flow field and have been linked to the performance of diffusers.

- **Streamlines:** Surface and volume streamlines or velocity vectors can provide information about the direction of the flow which velocity contours show in a less intuitive and direct way. Streamlines do not provide an idea about the magnitude of the flow velocity. This is why a streamline visualization is always coupled with a velocity contour of planar ($\sqrt{v^2 + w^2}$ on an x slice for instance) or perpendicular velocity. In the context of diffuser aerodynamics, streamlines that follow the surface can indicate attached flow while when they clearly follow a different path, they can indicate a separation region.
- **Streamwise (X) Velocity**: Considering the application of Bernoulli's principle introduced in Section 2.2, pressure in the underbody is low when velocity is high and high when velocity is low vice-versa. In particular, the literature presented in Figure 2.3 forecasts the presence of two suction peaks or high-velocity regions at the floor inlet and diffuser inlet. Lower pressure in the floor region is linked to higher downforce and so better aerodynamic performance of the diffuser. By means of the "pumping effect", more effective expansion in the diffuser region generates stronger suction in the floor which is indicated by a higher streamwise velocity. In addition, this indicator can clearly identify reversed flow which would unequivocally mark a region of separated flow.
- **Spanwise (Y) Velocity:** The spanwise motion of the flow can be an interesting indicator to quantify the magnitude of 3D effects. The loss or gain of mass flow can also be qualitatively appreciated by noticing the direction of the flow through the sides of the vehicle.
- **Vertical (Z) Velocity:** Similar to the information provided by streamlines, the vertical velocity component (w) can be useful to construct a clear picture of particle movement in the diffuser. Again, upward motion can be linked to attached flow. With a map of w, the shear layer in the wake can also be located.
- **Mass flow**: Through a constant area and considering density constant, mass flow is directly proportional to streamwise velocity. For the purpose of producing downforce,

the ultimate goal would be to increase the mass flow in the floor through the use of a well-studied diffuser geometry. Mass flow variation through the floor can also provide useful insight of cross flow motion which would cause additional or leakage of flow.

- **Downforce**: Although downforce is not directly a result of the experimental setup, with the use of a few assumptions, an approximation can be made in order to compare the different diffusers. This can be considered the most important performance parameter but also the one computed with the most uncertainty.
- **Ride height**: Being the direct result of the dynamic forces on the car, the ride height can be an indicator of downforce. Due to the fact that the suspension setup was kept constant throughout the whole experimental campaign, a lower average ride height for a diffuser angle can be considered a byproduct of higher downforce generation.

The chart shown in Figure 6.8 and the explanation provided above highlight how tightly related all these features are. Separated flow or increased separation strength can be a cause of general performance loss. On the other hand, a lack of vortical structures, providing effective sealing to the diffuser, can lead to spillage of low-pressure flow, less effective expansion in the diffuser and so less downforce in the floor. It can be then said that the observations made upstream of the diffuser with regard to streamwise velocity, mass flow and ride height are caused by the presence of the diffuser and are themselves indicators of the state of separated flow and vortical structures. For instance, observing the streamline pattern in the diffuser can hint towards the identification of separation. This in turn determines the performance the specific diffuser would achieve. Similarly, tracking the mass flow through the floor is a useful indicator of leaking and spillage effects and can be linked to downforce generation (or a loss of downforce).

Considering that the main purpose of the diffuser is to enable the generation of downforce in the floor region, being able to assess the relative changes in the performance of different diffusers would be a key feature of this experimental setup. The initial objective, which led to the choices made when designing the experiment, was not to quantify the downforce or pressure variations but after exploring the obtained data set, some interesting observations can be made concerning these parameters thanks to assumptions and simplifications.

7

Results

In this chapter, the results obtained after processing are presented and discussed. First, in Section 7.1, slices, streamlines and contour plots will be used to describe and discuss the flowfield for the different diffusers. Later, in Section 7.2, a more quantitative approach will be presented to gather information on the indicators of downforce, pressure and mass flow. Finally, Section 7.3 reports the results obtained when analyzing the convergence of the flow field when increasing the number of passages merged before binning.

7.1. Macroscopic Observations

In order to characterize the flow and compare the flow features of different diffuser geometries, a constant frame of reference was established. This is the same one imposed during the data processing phase and results in data aligned along the three axes shown in Figure 7.1.

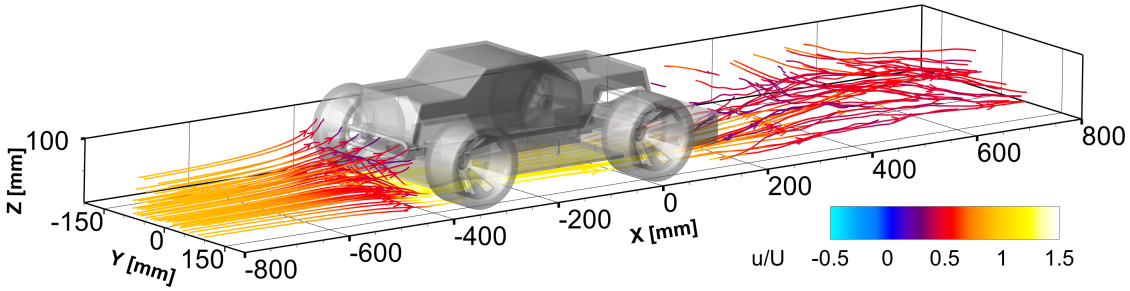

Figure 7.1: Full vehicle CAD model with diffuser $\theta = 15°$ showing axis direction and 3D streamlines colour-coded by streamwise velocity

Slices in X, Y and X shown in the next sections are extracted from this frame of reference. When necessary, an additional orientation guide will be provided.

Particle distributions Due to the nature of the data, it is not possible to populate an entire volume with valid cells. Figure 7.2 highlights the areas of exceptional particle density (purple) and those of unacceptable density (yellow) on the $y = 0$ mm slice. The blanking process introduced before takes care of ignoring cells where the particle count is below 5, the chosen threshold. As expected, the region before the passage of the car is densely packed with data and all corners of the volume have values of the variables. This is the case since these regions are built from particle images which capture bubbles soon after the opening of the curtains. Regions at higher x values are computed, on average, by later timesteps. Natural diffusion of

the bubbles after the opening of the bubble enclosure, added to the dispersion caused by the passage of the car results in some regions with gaps in the wake of the car. Finally, in separated or highly turbulent flow, typical of larger diffuser angles, bubbles require even more time to populate the domain to a density similar to other regions.

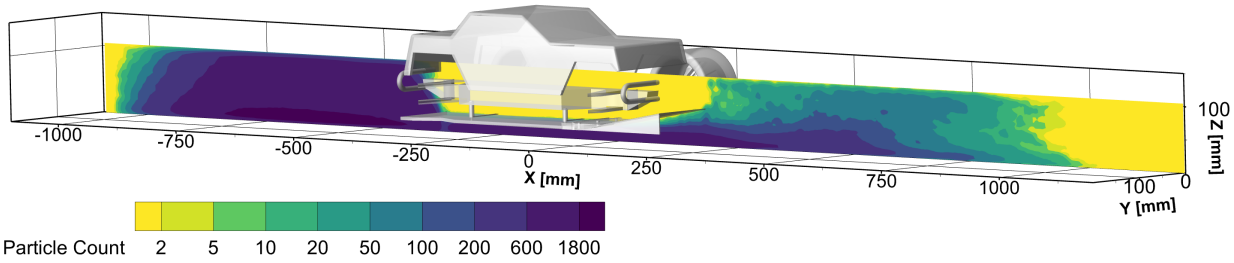

Figure 7.2: Contours of number of particles on each cell of the mesh

The region inside the car and above the diffuser shows no particles. This is due to the placement of the cameras, looking from below the vehicle and the vehicle's physical obstruction. It is also interesting to note that the edges of the domain in the x direction show a progressive drop in particle count. This is the consequence of the Galilean transformation and the finite nature of the time steps used (and available) for the transformation. Indeed, while "converting time into space", many frames are available to populate the central part of the domain while only a few are for the edges. Finally, the local drop in particles at the inlet of the floor is to be attributed to the time filter. Indeed, in the original frame of reference, this is the location where particles change the direction of motion in the x direction[1]. Changing direction implies that there may be one moment when the cameras capture a real particle appearing stationary. The filter may thus remove these particles as if they were outliers or smudges on the glass. Overall, this is not an issue since the filter has a length of 3 frames and it is unlikely that a particle remains stationary for that amount of time.

As a final remark on data quality, note that the case $\theta = 5°$ was the first tested. For this reason, the experimental routine was not yet fully optimized. Specifically, the opening of the curtain was not timed well. Indeed, opening the curtain too early led to many tracers escaping before the passage of the car therefore reducing the number of tracked particles for this case.

7.1.1. Streamwise (X) Velocity

A ground effect vehicle fitted with a flat floor is expected to present flow acceleration under the floor which relates to a lower pressure area. The vehicle's presence forces the air to deflect around it. Below the car, the ground imposes an additional solid-wall constraint which further constricts airflow into a converging duct-like structure. Considering mass conservation, the air experiences an acceleration here. Due to the 2D effects discussed in Section 2.2, the curvature of the flow is also characterized by additional low-pressure and high-velocity regions. These local maximums were described through the work of Ref. [8] and shown in Figure 2.3. The streamwise variation of u, obtained with the setup constructed, is shown in Figure 7.3. Here, the vehicle fitted with the four diffusers is shown from the side with flooded contours of normalized streamwise velocity. The choice of contour values highlights the acceleration fronts at the floor inlet and the faster-than-free-stream ($u/U > 1$) flow throughout the whole floor. To varying extents, all diffusers present high-velocity peaks where the flow is expected to curve ($x \approx -350$ mm and $x \approx 0$ mm). These local maximums of u/U, located at the floor's inlet region and at

[1] In the transformed frame of reference, these particles cross the $u/U = 1$ threshold from below.

Table 7.1: Streamwise average and maximum velocity for different diffuser angles

Angle	**5°**	**10°**	**15°**	**20°**
$\bar{u}/U$ @ -350 mm	1.12	1.25	1.23	1.21
$u_{max,1}/U$	1.28	1.31	1.32	1.29
$u_{max,2}/U$	1.22	1.28	1.32	1.24

the diffuser inlet are respectively referred to as first and second's peak locations.

Different diffuser angles are marked by different maximum velocities under the floor and different average velocities. To quantitatively characterize the flow the magnitude of the peaks and the average normalized u velocity within a $x = -350$ mm slice are reported in Table 7.1. The average velocity on the $x = -350$ mm slice provides an indication of mass flow through the floor's inlet for the different diffusers.

Due to the binning process, the maximums found are not outliers and exist within a region of smoothly varying values of u/U. In addition, the slices portrayed in Figure 7.3 are the result of the averaging of 5 slices in the vicinity of $y = 0$. The effective "width" of the data used to display the slice is 2 cm, the central 10% of the diffuser.

Figure 7.4 shows the velocity profile at $x = -350$, -175 and 10 mm (and at $y = 0$ mm) at varying z. According to the frame of reference established, these locations correspond to the inlet of the floor region, the middle of the floor and the diffuser inlet. These can also be described as "first peak", middle and "second peak" locations. At $x = -350$ mm, u/U is above 1 and is similar among the different diffusers as shown in Figure 7.4(a). As the flow traverses the underbody region, a boundary layer grows on the floor's surface, leading to a familiar boundary layer profile with a minimum close to the floor's surface, at $z = 25$ mm as shown in Figure 7.4(b). Finally, Figure 7.4(c) reports the development of the velocity profile at $x = 10$. Here the deceleration due to the boundary layer that originates from the surface at $z = 25$ mm is mitigated by the acceleration of the flow due to flow curvature. Indeed, the presence of the diffuser was seen to produce a strong streamwise acceleration at this specific x location thus forming the already discussed "second (low) pressure peak". This mechanism is in line with the local maximums tabulated in Table 7.1 and the general trends shown in Figure 7.3. At the diffuser inlet, the case with $\theta = 15°$ exhibits the largest streamwise velocity, which matches with the "second" peak velocity maximum of $u/U = 1.32$. All diffusers present a central lower-speed valley for $10 < z < 20$ mm. Fastest velocities are observed on the ground. In the absence of the diffuser, streamwise velocity would be monotonically decreasing from $z = 0$ mm (ground) until $z = 25$ mm (floor's surface) similarly to as seen in Figure 7.4(b).

The development of the boundary layer and velocity profile and its difference between diffuser angles is highlighted in Figure 7.5 where curves for the same diffuser are shown at different locations. The line $u/U = 0$ is positioned at the x location that the velocity profile belongs to. The car with slanted diffuser and solid ground are also annotated. The chart highlights the region where the airflow is accelerated beyond $u/U = 1$ (beyond the dashed line). As already discussed, the diffuser with $\theta = 15°$ is the most effective at accelerating the flow under the car both near the inlet of the diffuser but also close to the inlet of the floor itself. The same plots for $\theta = 10°$ and $\theta = 20°$ are included in Appendix B.

Looking closer to the flow in the diffuser, Figure 7.6 shows again a flooded contour of u/U featuring streamlines. The same slice-averaging process discussed before was applied here to

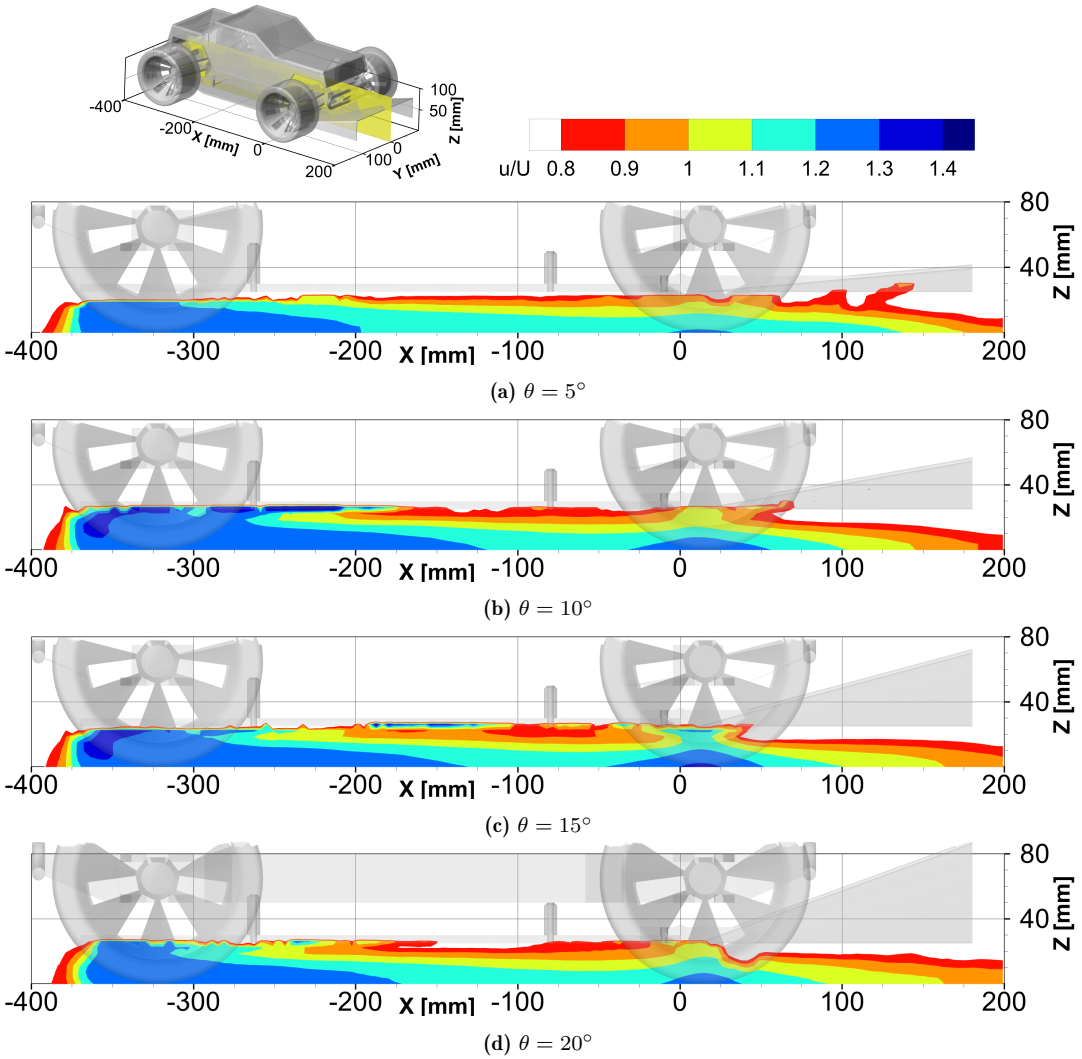

(a) $\theta = 5°$

(b) $\theta = 10°$

(c) $\theta = 15°$

(d) $\theta = 20°$

Figure 7.3: Y-slice at $y = 0$ showing flooded contours of u/U highlighting the position and size of the two acceleration peaks

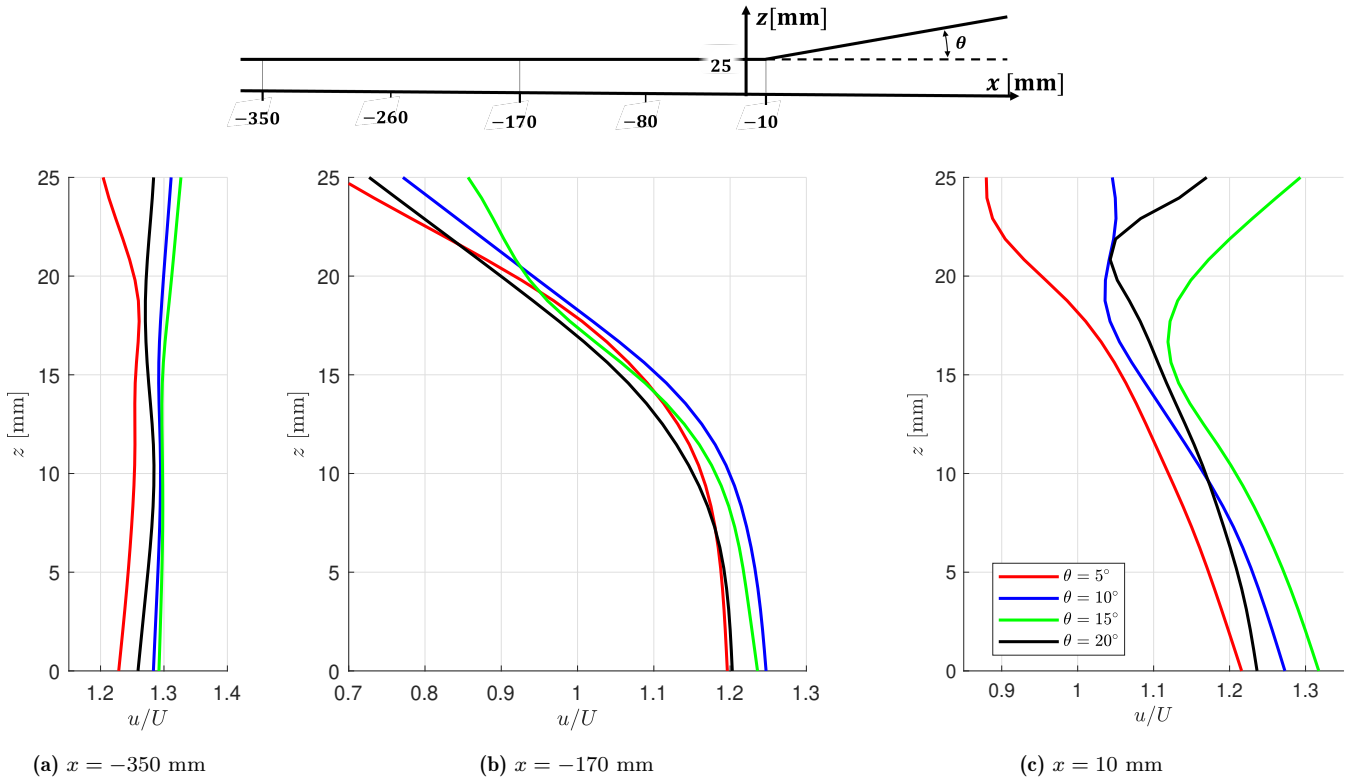

(a) $x = -350$ mm **(b)** $x = -170$ mm **(c)** $x = 10$ mm

Figure 7.4: Profiles of u/U under the vehicle at different x locations (floor inlet or "first peak", middle, diffuser inlet or "second peak") for the four diffuser angles

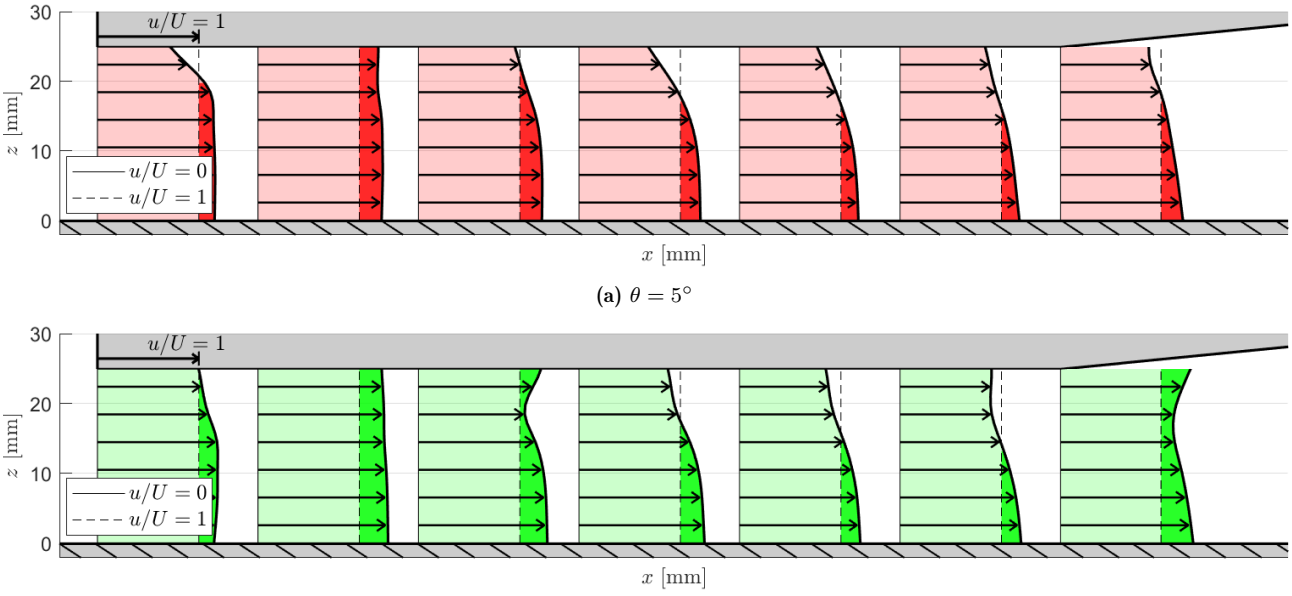

(a) $\theta = 5°$

(b) $\theta = 15°$

Figure 7.5: Profiles of u/U at different streamwise locations highlighting region where $u/U > 1$ with ground and car's floor annotation

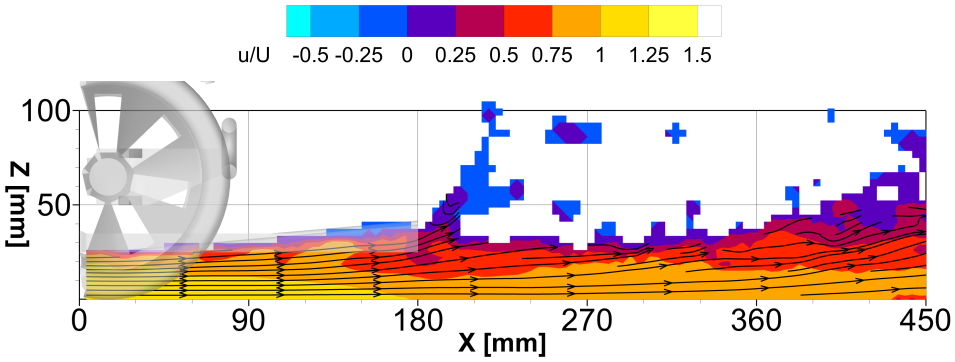

(a) $\theta = 5°$

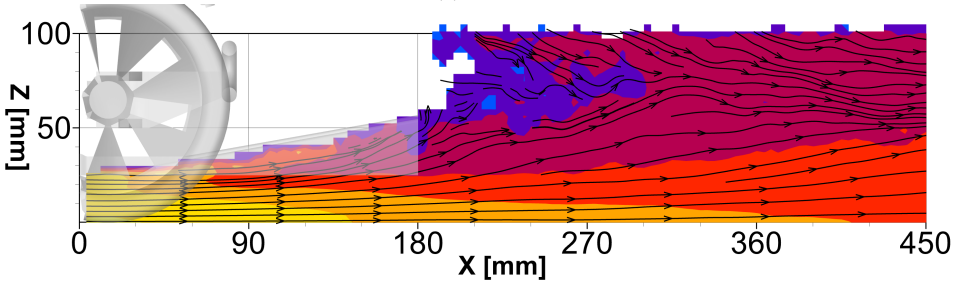

(b) $\theta = 10°$

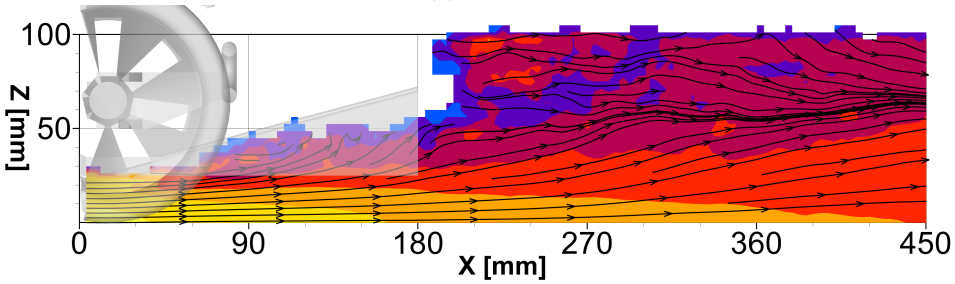

(c) $\theta = 15°$

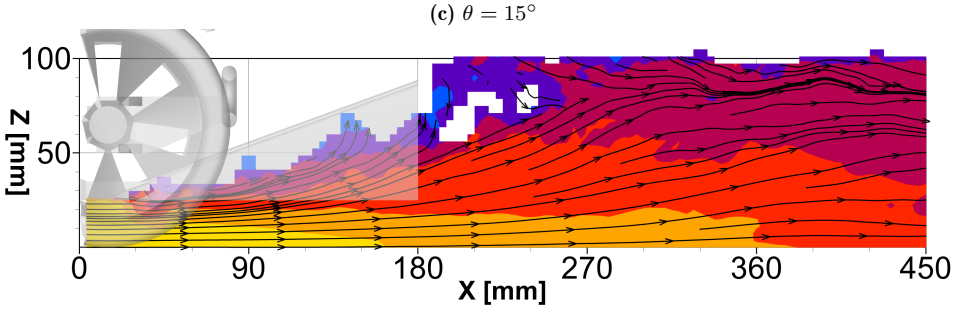

(d) $\theta = 20°$

Figure 7.6: Y-slice at $y = 0$ showing flooded contours of u/U and streamlines of planar velocity

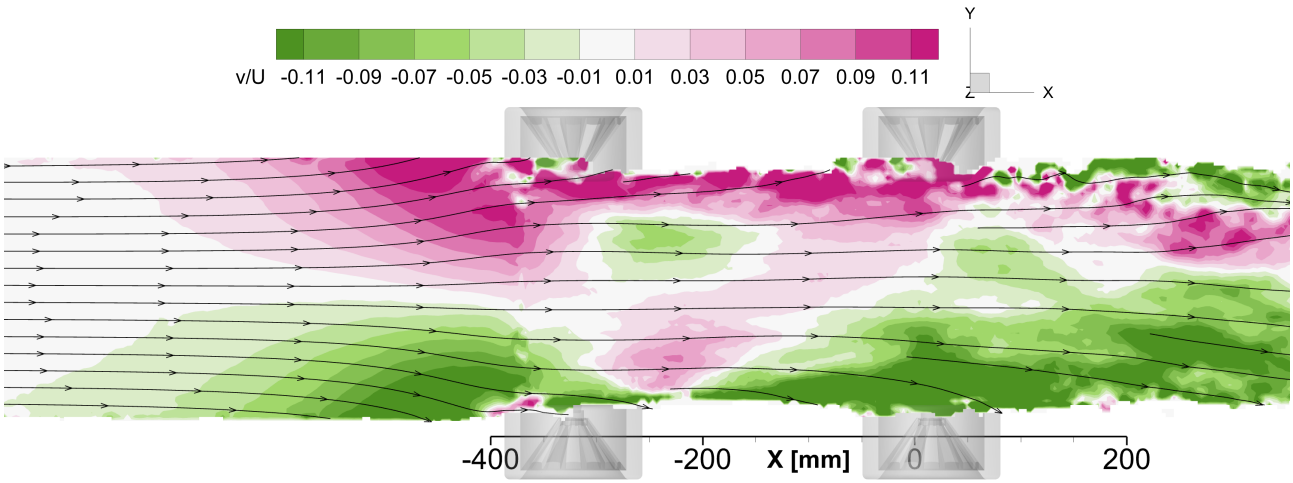

Figure 7.7: Slice at $z = 10$ mm showing streamlines and flooded contours of spanwise velocity (v) for $\theta = 15°$

provide a more robust description of the flow. The streamlines of planar velocity ($\sqrt{u^2 + w^2}/U$) also provide insights into how well the flow follows the change in surface direction. Where the diffuser angle is larger $\theta \geq 10°$, the wake is considerably larger than for $\theta = 5°$ as the region of slowed flow $u/U < 1$ dominates the region after the diffuser inlet.

7.1.2. Spanwise (Y) Velocity

Section 2.2 predicted low pressure in the floor and a strong pressure gradient through the sides that should be evident by inflow or air through the sides. The integration of out and inflow through the sides would lead to a measure of how much mass flow is gained or lost through the floor. This increased mass flow energizes the flow and allows more aggressive diffuser angles to work. Indeed, in a simplified 1D duct-like underfloor, the continuity of mass requires an equal inlet (free-stream) and outlet (diffuser outlet) area for perfect expansion. Thanks to inflow from the sides through 3D flow motion, the outlet area allowed for a given inlet area increases, resulting in lower pressure and higher streamwise velocity under the car. In reality, all geometry changes impact pressure and flow speed which in turn limit the performance of the vehicle.

Figure 7.7 presents an overview of the spanwise velocity component (v/U) on a Z-slice 1 cm from the ground for the diffuser with $\theta = 15°$. This provides a good idea of the general "sideways" motion of the flow across the whole vehicle. The chosen diverging colourmap highlights regions of flow moving "upward", towards $+y$ in pink and "downward", towards $-y$ in green. Pink regions on the upper side of the car and green regions on the bottom side relate to outflow. At a glance, the entrainment expected is not found the flow appears to move consistently move outwards throughout the whole length of the vehicle.

The stagnation region ($x < -400$ mm), is characterized by two large symmetric bubbles of outgoing flow. A different angle to this region and the floor inlet is shown in Figure 7.8(a), where a section at $x = -350$ mm is shown. This shows that the increasing outward flow velocity towards the edges of the floor is constant throughout the car's whole width. Further downstream, as shown in Figure 7.8(b), the outgoing flow leaves space for the more energetic and mainly streamwise flow through the middle of the car. This is marked by a large white region and by the local reduction of outgoing flow.

Interestingly, at around $x = -250$ mm, two bubbles of inflow exist. These are the same observed in Figure 7.7. Looking at Figure 7.8(c), this inward-moving air is found to come from the ground. Considering the huge effect of the tyre wake observed, this inward-moving air is a promising sign of low pressure under the floor. The presence of this stable region is also highlighted by

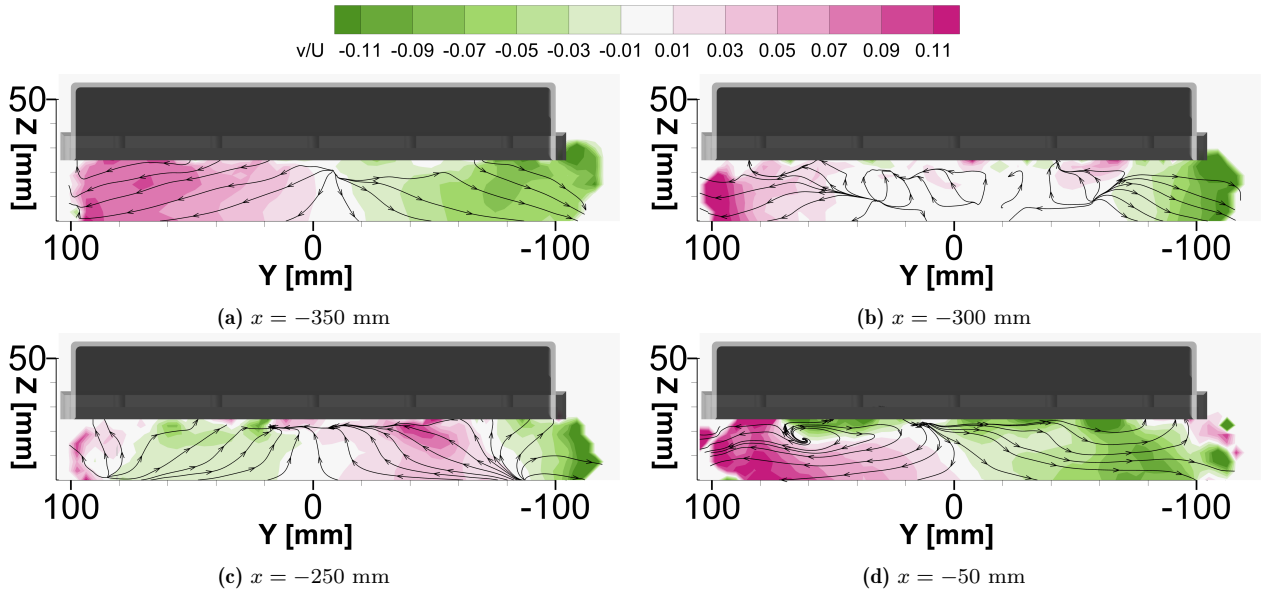

(a) $x = -350$ mm (b) $x = -300$ mm

(c) $x = -250$ mm (d) $x = -50$ mm

Figure 7.8: X-slices showing contours of v/U and streamlines at different locations of the floor for the diffuser with $\theta = 10°$

the momentary straightening of the streamlines (Figure 7.7) which have experienced a strong expansion in the xy plane since free-stream condition. Between $-200 < x < -50$ mm a slight convergence of the streamlines can be observed in the centre of the underbody region, marking an outward-facing pressure gradient.

From around $x = -200$ mm a gradually expanding region of outward moving flow, originating from the sides of the floor and growing towards the centre, dominates the domain. This outward motion is caused by the presence of the tyres. These large flow-obstructing appendices generate a large wake of turbulent and low-pressure air that evidently "sucks" air from beneath the car's floor. A more in-depth look at this phenomenon is included in Section 7.1.6. This motion is denoted by observing that streamlines close to the floor's edge experience a nearly constant outward push throughout the whole vehicle. Looking at Figure 7.7, small pockets of inflow can be detected near the leading edge of the tyres, marking the local stagnation of airflow in front of each tyre. This locally increases the pressure difference between under the car (low) and outside (high, tyre stagnation).

7.1.3. Vertical (Z) Velocity

One key indicator to detect separation and differentiate the performance of the diffuser geometries is the velocity component contours in the diffuser section as well as the streamline shape. These streamline were already presented and discussed with Figure 7.6. A similar graphic is proposed in Figure 7.9 showing contours of normalized w/U (vertical velocity). In this frame of reference, a positive, upward-moving w velocity is marked with blue contours. As expected, the flow in the diffuser moves upwards, following the expansion caused by the change in cross-sectional area. The flow over the car is sucked downward (red regions) as it joins the high-velocity jet that exits from the diffuser outlet. The two streams form a clear shear layer where streamlines from the two regions meet. This is visible through the accumulation of streamlines around the shear line.

All diffuser angles showcase a negative w velocity in the diffuser and a wake characterized by regions of downward-moving air coming from above the moving vehicle. For higher angles, the magnitude of w/U becomes larger to match a sharper expansion rate (faster spreading of

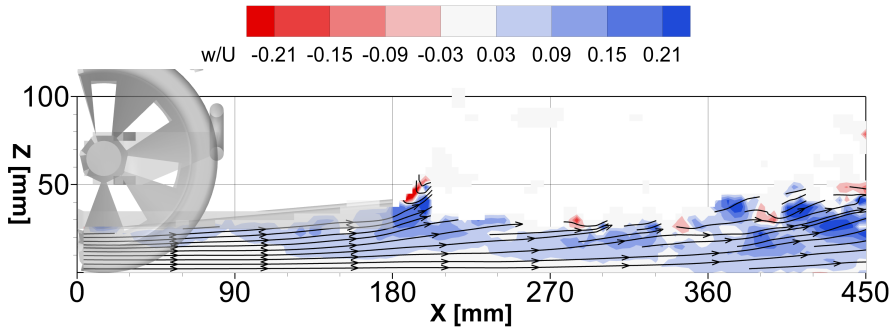

(a) $\theta = 5°$

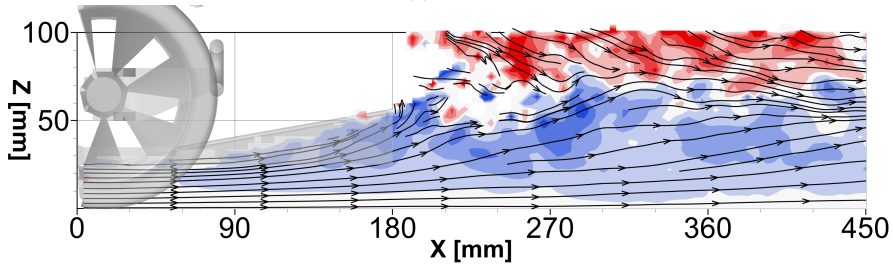

(b) $\theta = 10°$

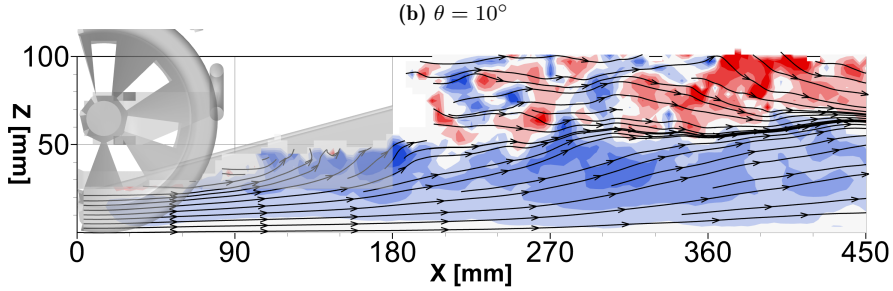

(c) $\theta = 15°$

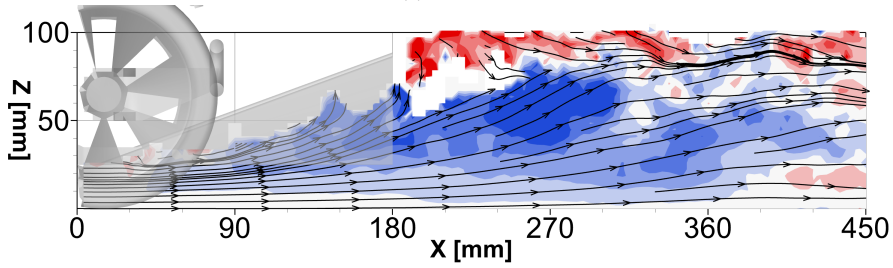

(d) $\theta = 20°$

Figure 7.9: Y-slice at $y = 0$ showing flooded contours of w/U and streamlines of planar velocity

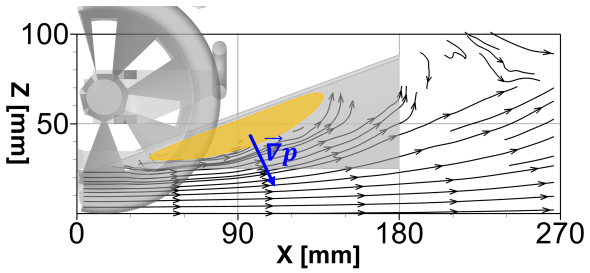

Figure 7.10: Streamlines of planar velocity in the diffuser with $\theta = 20°$ with annotated pressure gradient and low data and low-pressure region

streamlines).

In the case of $\theta = 5°$ and $\theta = 10°$, the flow expands in the diffuser in a homogeneous fashion as highlighted by the structure of the streamlines. At higher angles, the streamlines also expand but entail a larger curvature. Following traditional aerodynamic principles, streamline curvature is the consequence of a pressure gradient. This logic was already employed in Section 2.2 to explain the nature of the two low-pressure peaks that coincide with regions of streamlines curvature. In this case, the gradient is perpendicular to each streamline segment, pointing away from a potentially separated region. Technically speaking, the pressure gradient vector would point towards the convex side of the streamlines. Therefore, the large curvature of the streamlines upwards, in the diffuser, which can be observed for $\theta = 15°$ and $\theta = 20°$, is a strong indicator of the presence of a low-pressure bubble, around which these streamlines are curving. It is interesting to note that these low-pressure regions around which streamlines curve are also areas where data is missing. Since the blanking process hides cells where few or no particles are found, regions where the contour map does not reach and streamlines end abruptly mark the limit of the valid domain. As mentioned before, separated regions do not receive many tracer particles due to their recirculating nature. If the vehicle would traverse a long tunnel filled with bubbles, before arriving at the measurement area, more particles would have the physical time to reach these zones of recirculating flow.

Figure 7.10 again shows the streamlines in the diffuser for $\theta = 20°$. Here, annotations show the direction of the pressure gradient discussed along with the special region characterized by a lack of data and the origin of the pressure gradient. The presence of separation can be deduced by linking the low-pressure zone with streamline curvature with the lack of data in these regions. This type of region featuring both streamlines curving around it and a clear lack of data can be identified as regions of separated flow. These are seen to become larger at increasing diffuser angles.

7.1.4. Flow in the Diffuser

Figure 7.11 and Figure 7.12 present multiple X-slices specifically in the diffuser region of the vehicle with the $\theta = 5°$ and $\theta = 20°$ diffuser. An isometric view of the car showing the location of the slices is shown on top of Figure 7.11. Many of the observations that can be made when looking at these figures relate to the points made when looking at the v (Y) velocity. Indeed, both cases show a strong and consistent outflow of mass that is symmetric around the midplane. Circulatory motion is seen under the car ($x = -60$ mm) and right before the inlet of the diffuser ($x = 0$ mm) as a result of the outflow discussed. This rotation is opposite in direction to the one expected and predicted in Section 2.2 due to the reversed spanwise flow direction documented in Section 7.1.2 and observed in Figure 7.7.

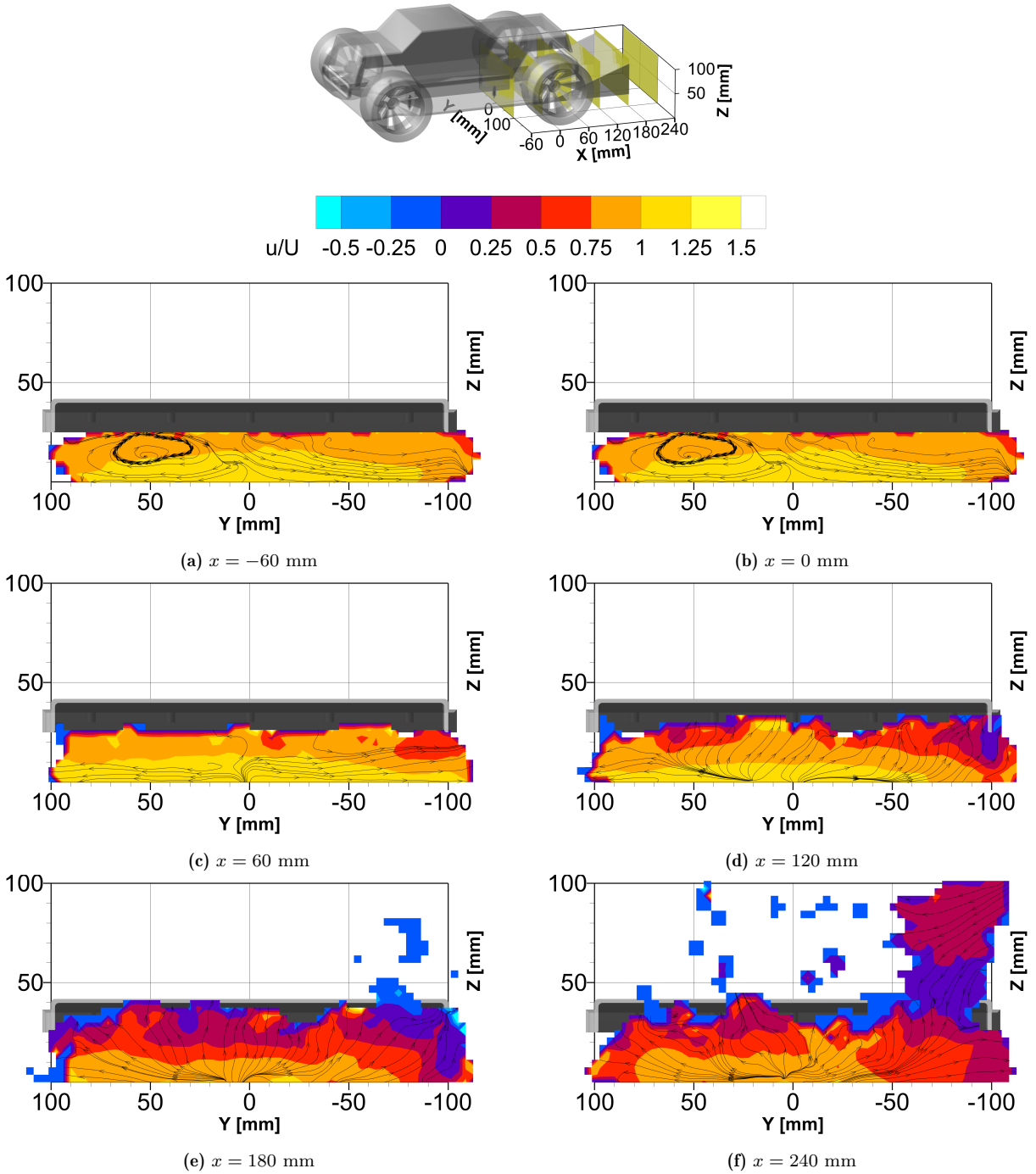

(a) $x = -60$ mm

(b) $x = 0$ mm

(c) $x = 60$ mm

(d) $x = 120$ mm

(e) $x = 180$ mm

(f) $x = 240$ mm

Figure 7.11: X-slices from 60 mm before the diffuser inlet until 60 mm after the outlet for the diffuser for $\theta = 5°$ showing contours of streamwise velocity (u/U, perpendicular to plane) and streamlines

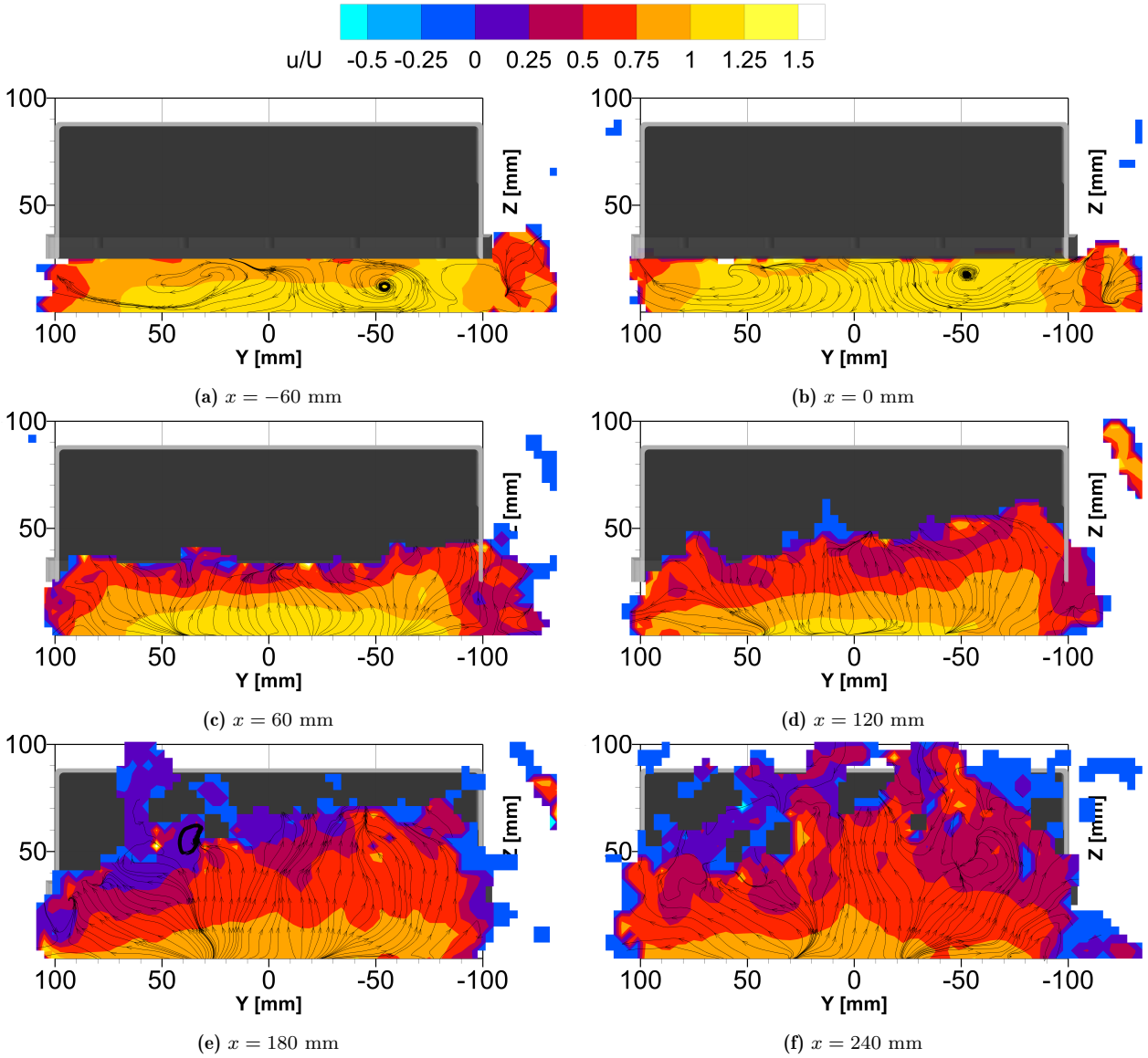

(a) $x = -60$ mm

(b) $x = 0$ mm

(c) $x = 60$ mm

(d) $x = 120$ mm

(e) $x = 180$ mm

(f) $x = 240$ mm

Figure 7.12: X-slices from 60 mm before the diffuser inlet until 60 mm after the outlet for the diffuser for $\theta = 20°$ showing contours of streamwise velocity (u/U, perpendicular to plane) and streamlines

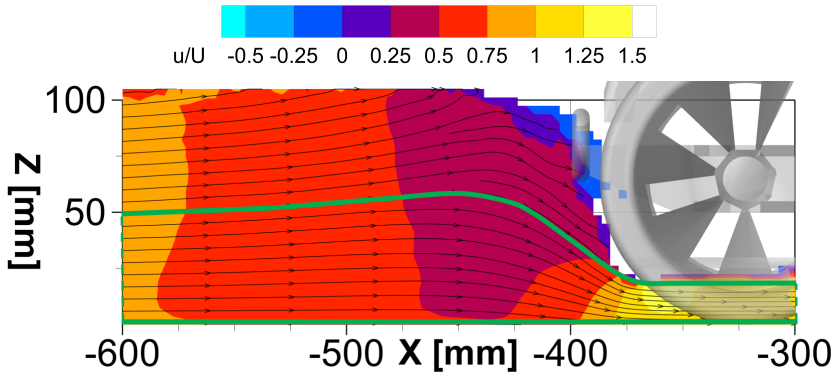

(a) $\theta = 5°$

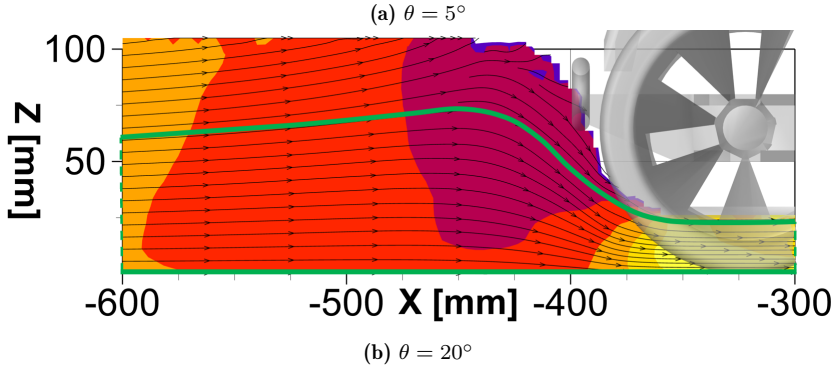

(b) $\theta = 20°$

Figure 7.13: Flooded contours of normalized u velocity featuring streamlines of planar velocity an annotated inlet tube shape on midplane slice ($y = 0$) around the car's front bumber

7.1.5. Stagnation

In the free-stream region before the car, it is possible to observe a smooth flow curvature through the shape of the streamlines and stagnation as reported in Figure 7.13 for two diffuser angles. This region is especially smooth due to the high tracer intensity obtained here resulting in a high number of triangulated bubbles.

The contours of streamwise velocity u/U show where the flow tends to accelerate (orange/yellow) and stagnate (purple/blue). Initially, the airflow is subject to even deceleration which is marked by almost vertical contour fronts. Flow in the top region of the domain encounters the bumper of the vehicle and shows a rapid deceleration and full stagnation. At the same time, to respect mass continuity, a portion of the flow is accelerated and deflected under the vehicle's floor. The acceleration fronts (orange→yellow) also show that flow closer to the ground experiences earlier acceleration.

Measuring the z position of the first streamline that enters the floor far upstream of the vehicle can help quantify the area ratio of a theoretical 1D nozzle that should behave similarly to this scenario. This information was used in Section 2.2. For case $\theta = 5°$ the height ratio between free-stream and under the floor is ∼5:2 (2.7) while $\theta = 20°$ is ∼8:2 (3.9). These ratios are derived from the annotations shown in Figure 7.13. The other angles have an area ratio between the one measured for the cases shown. This difference connects with the results obtained in Section 2.2 where it was seen that changing the diffuser angle and imposing free-stream pressure at its outlet led to changes in flow upstream, under the floor. The effect of the presence of the diffuser propagates even farther upstream to the stagnation region and even the free-stream before. In an ideal scenario, with perfectly attached flow, full pressure recovery in the diffuser and no 3D effects ($C_p = 0$ at diffuser outlet), the diffuser's outlet area should match the free-stream "tube"[2] height. Geometrically, the area ratio between diffuser inlet (same as

[2]In this context, tube or streamtube is used to characterize the portion of the flow below the stagnation

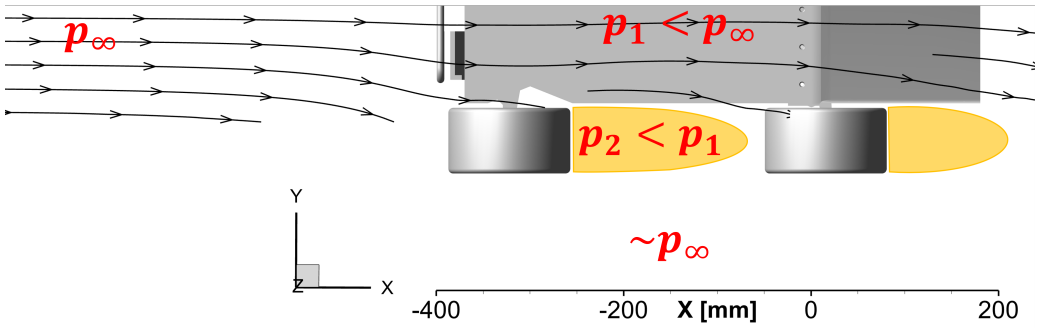

Figure 7.14: Bottom view of car with streamlines on $z = -10$ mm slice annotated with tyre wake and predicted (relative) pressure values

floor height) and outlet for $\theta = 5°$ is ∼3:2 (1.6) while for $\theta = 20°$ the real outlet area ratio is ∼7:2 (3.5). To summarize, at $\theta = 5°$ the free-stream inlet area is 5 units while the outlet is 3 while for $\theta = 20°$ the inlet is 8 units and the outlet is 7. For both cases, the free-stream inlet area is larger than the outlet area. This suggests a mass flow loss through the length of the vehicle and that less air is being pumped through the floor and diffuser than the theoretical limit. In a case without tyres where air flows inwards through the sides, the outlet area could theoretically be even larger than the inlet one due to the entrainment of flow through the sides thanks to the low pressure under the car.

To summarize, the stagnation point varies depending on the diffuser geometry. The difference in diffuser shape changes the area ratio between the diffuser outlet and inlet. Through the "diffuser pumping" effect discussed in Section 2.1, this physical change produces increased flow velocity upstream, under the floor (Figure 7.3) and even upstream of the car. This matches the results obtained from the theoretical 1D model built in Section 2.2. An effective change in outlet area is then linked to a change in inlet area ratio at free-stream location to respect mass flow continuity. While the general trend that expects the outlet (diffuser) and inlet (free-stream) area ratio to match is loosely found, the loss of mass flow through cross flow and 3D effects (Figure 7.7) leads to a less than ideal streamwise velocity under the floor which would reduce the downforce produced. These losses, linked to separation, turbulence and a potential loss of sealing vortical structures, which counteract the benefits of aggressive diffuser angles, grow in strength at high values of θ.

7.1.6. Final Observations: Separation and Vortical Structures

The general topics of separation and vortex-looking structures have been extensively covered in the literature, in the simplified 1 and 3D conceptual model constructed (Chapter 2) and throughout this section (Section 7.1).

Separation has been explained to be complicated to detect due to its physical tendency to repel tracers and bubbles. However, looking closer at the patterns of the streamlines and of the change in streamwise velocity, the consequences of separated flow can be identified throughout the whole domain.

Figure 7.14 presents a view of the vehicle's floor and diffuser from below with superimposed streamlines. In addition, the expected real relative pressure values in different regions are annotated. The wake of the tyre must generate a very low pressure in order to contrast the already low pressure present under the floor and seen through the acceleration in the floor. The vortices and the circulatory flow expected in the diffuser have not been found to be dominant

line, whose streamlines continue in the floor region

flow characteristics. The reversal of the spanwise (Y) flow direction compared to the expected direction (inflow), caused by the strong interference of the tyre's wake, is to be considered the main reason why the vortices that usually aid the sealing of the diffuser are not seen or why they show opposite circulation.

7.2. Performance Analysis

In this section, a quantitative analysis of the data shown in the previous section will be performed. The main metrics used for this purpose are pressure distribution along the underbody surface, downforce and mass flow under the vehicle.

7.2.1. Distribution of C_p and Pressure

Utilizing the methodology developed and explained in Section 6.6, the pressure distribution on the centerline of the underbody's surface (in the streamwise direction) can be estimated. To avoid the boundary layer and turbulent regions where Equation 2.2 do not apply, it was chosen to not follow the underbody surface. Instead, the probe line used to sample velocity values was chosen to be midway between the ground and the floor ($z = -12.5$ mm). On this line, the pressure coefficient can be obtained using the relationships reported in Equation 2.2. Importantly, these relationships relate velocity and C_p as: $C_p = 1 - (\frac{u}{U_\infty})^2$. From this, the pressure is also readily found, again considering inviscid, incompressible, and irrotational flow.

The results of this analysis are shown in Figure 7.15. Here, the planar velocity component ($\sqrt{u^2 + w^2}$), interpolated on the probe line is plotted along the normalized streamwise coordinate (x/L_u, the underbody length is $L_u = 550$ mm). The lines above the charts represent the ground, the diffuser surface and the probe line on which data is plotted. The distribution of C_p is also obtained and plotted using Equation 2.2. In this figure, the x axis has been highlighted to show the positive and negative C_p regions. The two regions split by the $C_p = 0$ line are linked to $p > p_\infty$ as C_p is positive and $p > p_\infty$ when it is negative. It can be seen how the floor region ($0 < x/L_u < 0.7$) is responsible for almost all the low pressure in the underbody. Since $C_p = 0$ ($p = p_\infty$) on the top surface of the car, when $C_p > 0$, the resulting integral pressure force is lift while downforce is produced when $C_p < 0$. Later, it will be shown that a large "negative" area (below x axis) is linked with downforce while a large "positive" area implies lift generation. Adding these effects together leads to the total force balance of the car.

All diffuser geometries perform similarly and show the same shape of C_p featuring two peaks and a fast deceleration and expansion in the diffuser. The relative height of the peaks between diffusers matches with the differences already identified in Section 7.1.1. Indeed, the diffuser with $\theta = 15°$ performs best in this case, showing the highest velocity maximums and low-pressure peaks. The diffuser pumping effect mentioned before leads to different velocities and pressure distributions under the floor depending on the angle of the diffuser fitted. Since downforce is related to the area enclosed between the $C_p = 0$ line and the C_p distribution local large suction peaks may not be as important as an average low pressure throughout the whole floor.

While the low-pressure peaks could already be discussed and appreciated in Figure 7.3 and Table 7.1, the distribution over the whole floor can be better understood now. Figure 7.15 shows how the $\theta = 10°$ does not entail large velocity peaks but presents a considerably higher velocity across the whole floor.

All curves present a small plateau of steady velocity right after the first peak. This can be explained by noting that this is also the location of where the front tyres are. While the wake of the tyres is a really disruptive presence to the aerodynamics below the car and in the diffuser,

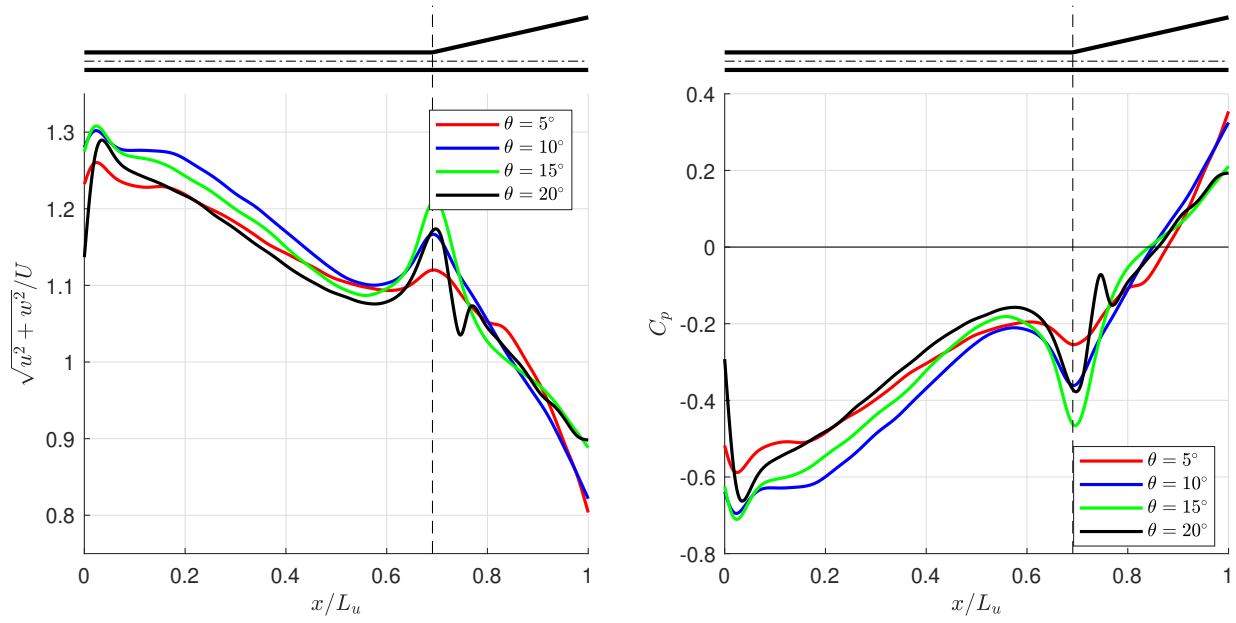

(a) (b)

Figure 7.15: Planar velocity magnitude and C_p on offset centerline of the underbody for different θ

in this section it creates a physical barrier where air is constrained and cannot expand in the y direction. As soon as the flow encounters the wake of the said tyres, a large low-pressure zone in the sides of the vehicle allows the flow underneath the car to expand rapidly, losing suction and low pressure. It is interesting to note that the flow through the diffuser with $\theta = 20°$ experiences three high-speed local peaks. The first and the second have already been extensively discussed. The third, which occurs around $x = 0.75L_u$, is related to the separation region identified and displayed in Figure 7.10. Although this local pressure minimum may be beneficial for downforce generation, the large loss in potential suction through the floor due to this separation bubble is much larger. Finally, all curves shown find the flow at the outlet to be over-expanded, experiencing a pressure coefficient above 0. This is mainly to be attributed to the highly turbulent nature of the wake where Equation 2.2 are not valid anymore and tend to severely overestimate pressure. Considering the motion of a fast-moving car, the air molecules are expected to return to a standstill ($u/U = 1$ in this frame of reference), after a time (and a distance) in the order of 10s and 100s of seconds[3]. Using these simplified equations, perfect pressure recovery to $C_p = 0$ can only occur at $u/U = 1$ or when airflow returns to a standstill in the reference frame of a static observer outside of the moving vehicle.

Comparison with literature The literature presented before predicted the presence of the two large suction peaks as well as a near-complete recovery of pressure. The experimental data quoted in Ref. [8], obtained on a Ahmed bluff body featuring a diffuser angle of 9.4° is superimposed to the experimental data of this investigation in Figure 7.16. Due to a slight difference in the diffuser length between the Ahmed body in the referenced literature and the RC car model, and the lack of a curved inlet in the RC car model, the dataset from literature has been slightly adjusted[4].

[3]By comparison, jet wake, the turbulent wake of taking off planes, can remain dangerously strong to other planes taking off for minutes.

[4]The whole curve has been shifted to the left by $x/L_u = 0.087$ and he final data points after the second peak have been stretched to align with the diffuser outlet to ensure that both curves cover the entire x/L_u range.

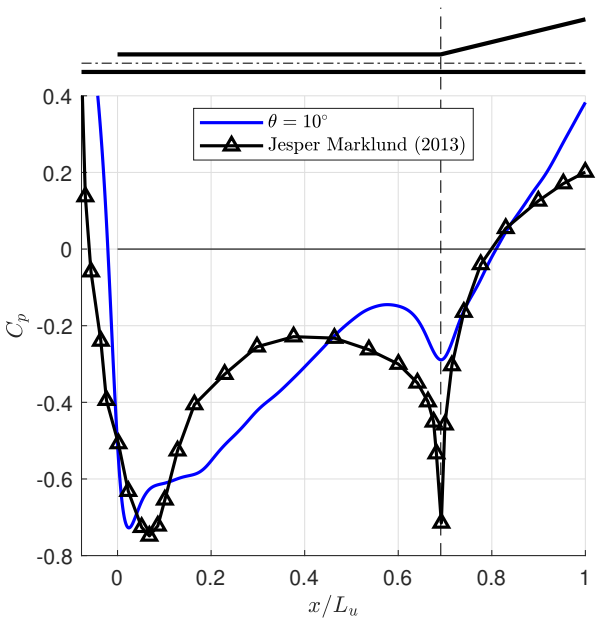

Figure 7.16: Comparison between PTV data of the diffuser with $\theta = 10°$ and the pressure tap, wind-tunnel experimental data report in Ref. [8]

Two main observations can be made with such comparison. Firstly, the peaks are smoother in the PTV data when compared to the literature. This is due to the non-negligible mesh size on which the scattered data is binned. This process effectively filters out high-frequency (smaller than the mesh size) features. Secondly, the valley of expanded flow and subsequent drop of pressure leading to the second pressure peak discussed is significantly different for the experimental data of $\theta = 10°$. This is due to the presence of the tyres which create a very different pressure distribution on the car's sides compared to a wheel-less Ahmed body. Finally, by extending the probe line farther into the upstream region before the car (Figure 7.16), the pattern of rapid pressure drop can be appreciated in both literature and experimental data.

7.2.2. Downforce

Integrating the pressure times the area over the underbody surface and the top surface (assuming that $C_p = 0$, $p = p_\infty$) and taking the difference between the two resulting forces provides an approximation for downforce (force in the z direction. When this force, F_z points towards the ground ($-z$), it is called downforce. Otherwise, it is lift. The equations and scheme displayed in Figure 7.17 show how the measure of downforce can be obtained from discrete pressure data points on mesh cells. While before, C_p was described on a straight probe line midway between the car and the ground, this line is now extended in the y direction ($-100 < y < 100$ mm) to form an xy plane at $z = 12.5$ mm. This way, downforce can be measured including the losses present on the sides of the floor due to 3D effect. The superscript ^{t} implies that the variable belongs to the top surface while ^{b} marks the variables of the bottom (underbody) surface.

$$F_z = \int p^b dA^b - A^t p_\infty$$

$$F_z = \sum_{i=1,j=1}^{n-1,m-1} dF^b_{ij} - A^t p_\infty$$

$$dF^b_{ij} = dxdy \cdot \frac{1}{4}(p^b_{ij} + p^b_{i+1,j} + p^b_{i+1,j+1} + p^b_{i,j+1})$$

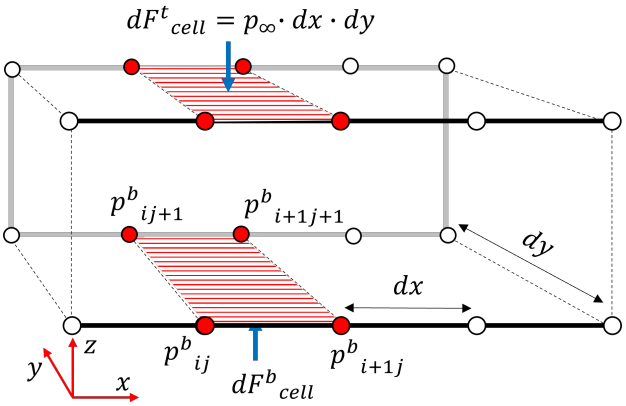

Figure 7.17: Simplified car fitted with slanted diffuser showing pressure data points on top and bottom surface to be integrated to obtain a resultant force along with relative equations

In this formulation, the force acting on the top surface is simply $A^t p_\infty$ which in practice was evaluated as $p_\infty \cdot \sum_{i=1,j=1}^{n-1,m-1} dxdy - A^t p^t_\infty p_\infty$. This was necessary since there may be cells in the plane chosen which do not have data and both sides should account for this. By adding up the contribution of each cell and subtracting the force on the top side, the total downforce, F_z, is computed. Figure 7.17 also explains how come, when adding up the pressure forces, the top side receives a $-$ sign and the bottom side a $+$. In order to remain consistent with the coordinate system used until now (positive z upwards), a positive resultant force implies lift while a negative one implies downforce. Using this scheme, the pressure data is located in the vertices of the cell's edges. The values at the four corners of each cell are averaged to compute the force pressure force on each cell. The script that performs this computation from the 3D binned data is included in Appendix A.

Table 7.2: Downforce generated by different diffuser geometries as obtained from potential flow analysis

Angle	**5°**	**10°**	**15°**	**20°**
F_z [g] ($U = 6$ m/s)	35.8	57.8	48.7	32.5
F_z[5] [g] ($U = 20$ m/s)	554.9	675.1	626.5	524.6

These results show that the diffuser with $\theta = 10°$ produces the largest downforce. This matches the prediction made by looking at Figure 7.15. This diffuser geometry is followed by $\theta = 10°$, $\theta = 5°$ and finally $\theta = 20°$, which produces the least downforce. Under this performance metric, the diffuser with $\theta = 10°$ is the best one among the four geometries tested. Fitting these four data points with a quadratic polynomial, a downforce maximum is expected in the range $10° < \theta < 15°$. This is in line with the wind tunnel experiments obtained and presented in Ref. [15] which found a downforce maximum at a diffuser angle of 13°. When considering the data on the 1D probe line only, and using the pressure on this line to compute downforce over the whole width ($2d$) of the floor ($dF^b_i = p_i \cdot 2d \cdot dx$), the downforce is higher. The force calculated is 50.0, 60.8, 56.4 and 47.2 g for the 5°, 10°, 15° and 20° diffuser respectively. These results would relate to a case with reduced 3D effects. The downforce loss is to be attributed to the flow deceleration and subsequent pressure loss near the sides which is not accounted for when considering values on the midplane only. Finally, since some cells lack data, the effective area of integration is smaller for the 2D case.

[5]Force obtained at freestream velocity 230% higher than average passing speed in the experiments.

7.2.3. Ride Height

A side-effect of downforce applied on a vehicle with suspension is a change in ride height. A larger downforce would ultimately lead to the compression of the spring dampers and to a lowering of the ride height. This complicated further the study of the flow under the vehicle as it becomes a highly dynamic environment. Due to the fact that the downforce produced by the vehicle with all four diffuser geometries is around 50 g[6], and that this weight was seen to not produce any suspension compression, no measurable ride height difference is expected. Furthermore, the bumpiness of the road and resonating motion of the car have seen to produce ride height changes of up to 1 cm in extreme cases. Figure 7.18 reports the average ride height of the markers among all frames available and all available runs for each diffuser angle.

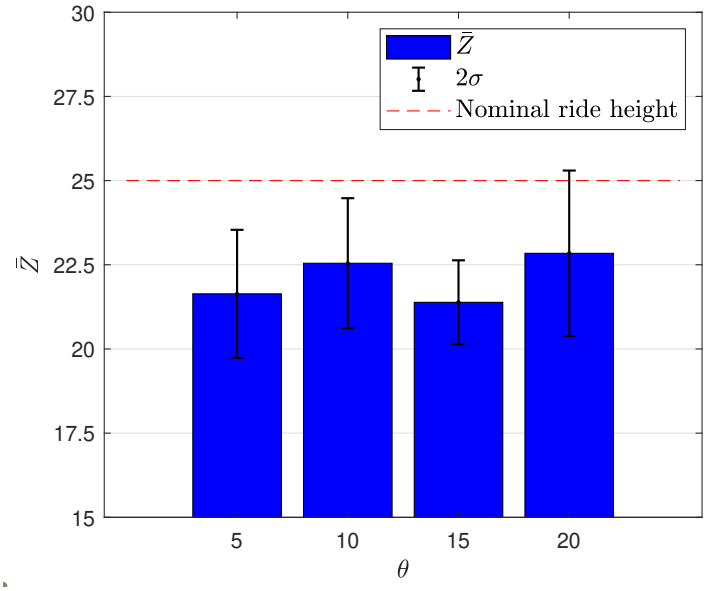

Figure 7.18: Average z position (ride height) of markers among all available runs of the four diffuser geometries with error bars for a 69 % confidence interval (2σ, $\pm\sigma$)

Although some changes are visible, the error bars ($\sim 70\%$ is within $\pm\sigma$) indicate that no trends can be accurately deduced.

7.2.4. Mass Flow

Obtaining the mass flow under the floor of the moving vehicle can be a key indicator to confirm the observations made before concerning the loss of mass flow through the sides due to the strong low pressure in the wake of the tyre. This behaviour has also been seen by analyzing the Y component of velocity in Figure 7.7 and Figure 7.8.

Due to the fact that the mesh size is constant in the entirety of the domain, the average velocity perpendicular to a slice is proportional to the mass flow through that slice. This measure can be obtained in the same way as already done in Section 7.1.1. The definition of mass flow through a constant area and at constant density is formulated below.

$$\dot{m} = \rho A u = \rho \sum_{i=1}^{N} A_i u_i = h^2 \rho \sum_{i=1}^{N} u_i = \rho \frac{A}{N} \sum_{i=1}^{N} u_i = \rho A \bar{u} \tag{7.1}$$

The final result is obtained by noticing that the sum of the mass flow through the area of each

[6]The weight of a large egg or a pair of Apple AirPods with the case [31].

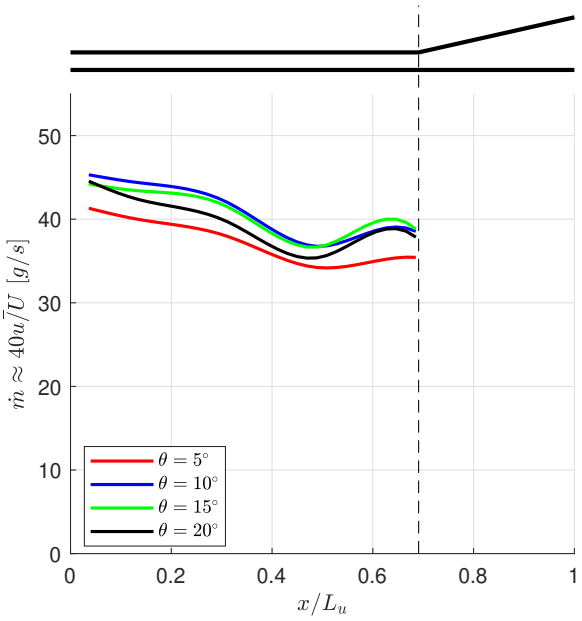

Figure 7.19: Average u/U velocity through slices of x plotted against normalized length x/L_u

cell ($A_i u_i$) equals the average velocity among all cells multiplied by the total area since each cell has the same area ($A = h^2 N$). Here, h is the edge length of the square mesh cells to which each velocity belongs. A is the total cross-sectional area through which mass flow is computed. $\bar{u}$ is the average perpendicular (streamwise) velocity through this slice. The computation of the average velocity at different x locations was limited to slices that span $-25 < z < 0$ mm (ground to floor height) and $-100 < y < 100$ mm (flat floor width). The computation of mass flow after the beginning of the diffuser $x > 10$ mm is complicated due to the non-constant area and the fact that not all cells have data. Averaging u on the available area could lead to large underestimations of the total mass flow through these locations and therefore no trends can be deduced.

In the floor section, where the cross-sectional area of the duct-like passage is fixed and fully packed with data points, the flow of mass through the slices can be written as shown in Equation 7.2. Ignoring compressibility, $\rho = 1.225$ while u_c is set at 6 m/s, the average passing of the vehicle computed among all passages.

$$\dot{m}\ [\text{kg/s}]] = \rho A \frac{\bar{u}}{U} u_c = 1.225 \cdot 0.2 \cdot 0.025 \cdot 6 \cdot \frac{\bar{u}}{U} \approx \frac{1}{25}\frac{\bar{u}}{U}; \quad \dot{m}\ [\text{g/s}] \approx 40\frac{\bar{u}}{U} \tag{7.2}$$

Table 7.3 reports the mass flow values found from the average streamwise values found in Section 7.1.1.

Table 7.3: Mass flow through $x = -350$ mm slice at $u_c = 6$ m/s

Angle	**5°**	**10°**	**15°**	**20°**
$\dot{m}\ [g/s]$	41.3	46.0	45.2	44.5

Perhaps more interesting to the discussion of this chapter is the variation of $\dot{m}$ through x slices at different x locations shown in Figure 7.19. The key takeaway from this chart is the downward trend. This trend matches well with the variation of v in Figure 7.7 and Figure 7.1.

The bump in streamwise velocity at around $x = 0.65L_u$ can be explained by observing that the front of the rear tyres is positioned at this location. The high pressure expected right in front of this object, which would also entail its own stagnation region forces oncoming air to be diverted outwards with respect to the tyre. Some of this flow ends up mitigating the mass flow leakage seen throughout the floor's length thus locally increasing streamwise velocity. This does not justify the difference of this peak among different diffusers. The strength of the second acceleration peak shown in Section 7.1.1 that was discussed to be a consequence of the local curvature of the underbody's surfaces, is much stronger for higher diffuser angles. This leads to the low-pressure minimum displayed in Figure 7.15. Evidently, this local low-pressure zone creates sufficient suction to increase the mass flow.

7.3. Convergence of Results

One interesting analysis of the binned data is related to the convergence of the results when increasing the number of car passages considered. Indeed, when choosing how many runs to perform for each diffuser angle, a big assumption and educated guess was that 20 recordings of the car's passage, when averaged together, would form a good picture of the flow around the car.

To measure the effect and benefit of including an r^{th} additional run, the binning process is performed multiple times, each time adding a run as input to the binner script. The error associated with each total r (number of runs used for binning) is defined as the root mean square of the difference in absolute velocity ($\sqrt{u^2 + v^2 + w^2}$) between all cells of the 3D volume between the binned solution found by using r runs and using $r - 1$ runs. The formula for this error is shown in Equation 7.3. The sum is actually performed on a 3D mesh but only the index i is written for clarity.

$$e_r = \sqrt{\frac{\sum_{i=1,j=1,k=1}^{n,m,p}(x_r - x_{r-1})^2}{n \cdot m \cdot p}} \tag{7.3}$$

In practice, using array operations, this result can also be obtained through the "square root of the average squared delta" between the absolute velocity magnitude in a cell for subsequent values of r and among all cells. The short script describing this procedure is included in Appendix A.

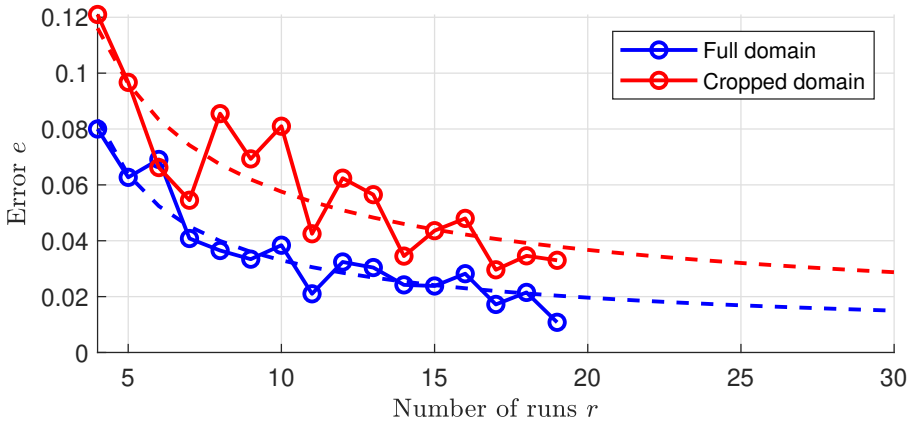

Figure 7.20: Error plot for different total number of runs on full and cropped domain including $a/(\sqrt{r} + b)$ fit (dashed line)

It is important to note that all arrays include `NaN` values in certain locations (inside the car

and in cells with insufficient particles). These empty cells vary between solutions x_r and $x_{\neq r}$ and should not be included in the averaging process.

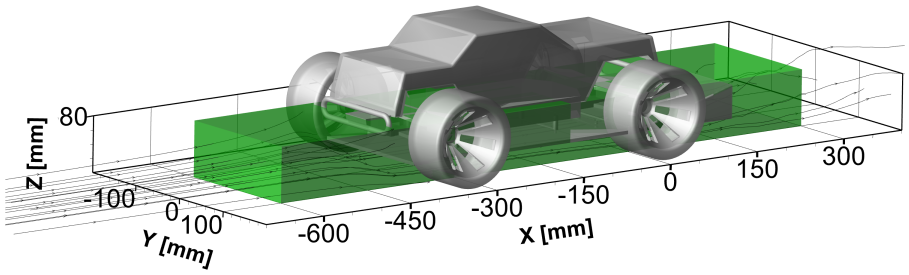

Figure 7.21: Physical size of sub-domain (green box) used for convergence analysis

The result of this analysis are shown in Figure 7.20. Due to the fact that total particle count can vary drastically between files of different runs, including a large run file that entails many particles has a large relative effect on the binner results (large error) compared to adding a small file with few particles. Therefore, verifying the percentage error linked to two values of r to be less than a threshold may not be as important as observing the complete trends reported in Figure 7.20. The cropped domain data points represent the error of the binned data limited in the region highlighted in Figure 7.19 ($-600 < x < 300$, $-100 < y < 100$ and $-80 < z < 0$). This was done to highlight that most of the variation and oscillation in the binned results occurs inside the cropped domain, the floor and the diffuser area, the region of most interest in this investigation. Observing the inverse quadratic fit of the real error data, the trends tabulated in Table 7.4 are extracted. The fitting model $a/(\sqrt{x}+b)$, requires $a = 0.1328$ and $b = -0.856$ for the full domain data points and $a = 0.0635$ and $b = -1.238$ for the cropped domain. The specific function used to fit the data was chosen since it is commonly agreed that the error of a function that entails some degree of random sampling scales with the inverse of the square root of the sample size (Monte Carlo, $1/\sqrt{N}$).

Table 7.4: Number of runs required to achieve a convergence (percentage change in error between two consecutive r values) below 10, 5 and 2 %

	r (<10%)	**r (<5%)**	**r (<2%)**
Full domain	8	14	29
Cropped domain	9	15	32

The table data indicates that for the full domain, adding data from a 15th run would lead to a change in the resulting velocity field of less than 5%. Achieving a 2% convergence requires data from a large number of runs (> 29 for the full domain and > 32 for the cropped domain) which may not be practically possible to obtain. Performing a minimum of 20 runs would be considered the minimum to achieve a convergence of at least 5% while ensuring that a few runs can be discarded if necessary without compromising the results of the experiment. It must be noted that, if the field of view of the cameras had allowed to view the entirety of the diffuser in each passage, each run would add a large number of extra particles to the existing particle cloud and therefore yield a faster convergence.

8

Conclusions and Recommendations

Aerodynamics is a core discipline of the design of automotive vehicles both for personal and professional racing use. The study of the flow, applied to the large and multidisciplinary activity of vehicle design, is an important tool to produce safe, stable, and high-performance machines. Wings, splitters, vortex generators, and diffusers are commonly employed on performance-oriented vehicles to manage the airflow and, most importantly, generate downforce. In this context, downforce is the aerodynamic force by which a ground-effect vehicle is pushed towards the ground. Strong and predictable downforce is advantageous as it provides additional grip through the vehicle's tyres thereby increasing cornering speed and reducing lap time around race tracks.

Within the set of aerodynamic features of vehicles, the diffuser and underbody regions are responsible for a large portion of the total downforce produced. For instance, more than 50% of the total downforce generated by the 2009 F1 car comes from the diffuser and floor, while they account for only 10% of the drag [7]. Studying the flowfield in and around the diffuser and underbody is a challenging activity due to the difficult visual access, often impaired by tyres and possible side plates. Multiple studies have attempted to characterize the flow in the diffuser by simplifying the problem using scale models and Ahmed bodies in a wind tunnel environment. The emergence of PIV techniques for large-scale experiments [28], advanced processing techniques like Shake-the-box [3], and the development of the Ring of Fire methodology[1] [2] sparked interest in studying the flow in the diffuser of automotive vehicles by leveraging the realistic ground interaction achievable though Ring of Fire style experiments. The objective of this investigation was to construct a PTV experimental setup where cameras have direct viewing access to the underbody and diffuser of a moving ground vehicle to characterize the flow underneath it. In addition, it was key to demonstrate the viability of the designed experiment to host a full-scale vehicle in a future test and generalize the method to benefit many applications. Finally, four different diffuser geometries with varying diffuser angles were tested to highlight the setup's ability to capture differences in the flow field and to understand the mechanism of downforce production.

Extensive study of the problem and consideration of the many limitations resulted in the conception, design, and construction of a two-camera Particle Tracking facility featuring Helium Filled Soap Bubbles and LED illumination (Figure 5.2 and Figure 5.3). The distinctive feature of this design is the unprecedented optical access to the inside of the diffuser of a moving wheeled car. This was achieved by placing cameras underground and by using mirrors to control the viewing angles.

[1] A type of experiment where the object of interest travels through a PIV measurement zone

The images obtained during the experimental campaign that took place in November 2023 were enhanced with image processing tools and then processed with the Shake the Box algorithm to produce the particle tracks. In post-processing, custom scripts were used to convert the particle data from the laboratory's frame of reference to the vehicle's (moving) reference system to produce a wind tunnel-like data representation (Galilean transformation). The scattered data of multiple runs (of the same diffuser geometry) was joined together and interpolated onto a Cartesian grid through the binning process. The resulting 3D domain of gridded velocity vectors constitutes the result of this investigation.

8.1. Study of Separation, Downforce and Vortices in the Diffuser

In order to describe the aerodynamics of the diffuser, a few important aspects were chosen to lead the research. In this regard, the investigation aimed, among all research questions, to determine "*at which diffuser angle [...] flow separation occur(s)*". Identifying separation can usually be done by observing the location of flow reversal. Since the time needed for tracers to enter reversed flow regions wasn't provided with the setup developed, flow reversal was not found and instead, gaps in the data were seen. Gaps in data were caused by the lack of particles while curving streamlines were discussed to be the consequence of a pressure gradient (Figure 7.10). The presence of a region of curved streamlines around a zone lacking data was argued to be a solid criterion to identify separated flow. Streamline curvature was observed for all diffusers with $\theta \geq 10°$ highlighting regions of low pressure (Figure 7.9). Separation originating from the diffuser inlet was seen to dominate the flowfield for the diffusers with $\theta = 15°$ and $\theta = 20°$. In these cases, large regions of missing data and significant streamline curvature were observed and linked to separated flow leading to sub-optimal performance. This loss of performance is also the cause of the difference between the theoretical model presented in Section 2.2 (1D, inviscid, incompressible, purely geometry based), which predicted the $\theta = 20°$ diffuser to produce the lowest pressure under the car, and the measurements. Indeed, maximum suction and downforce were not found at the highest diffuser angle but between $\theta = 10°$ and $\theta = 15°$. This is in line with Refs. [15], [9] and [14] which found a maximum downforce diffuser angle at $\theta = 13°$.

Again within the topic of flow study and investigation of the aerodynamics of the diffuser, one important research question was: "*which diffuser angle yields the highest downforce?*". To obtain an estimate of downforce, the flowfield was first analyzed to locate the high velocity (and low-pressure peaks) predicted by literature. The presence and magnitude of these peaks, along with the average speed under the car for different diffusers is a key performance indicator of the diffuser. Downforce is enhanced by the presence of the diffuser not by generating downforce directly but by increasing the area ratio of the diverging duct and forcing the pressure under the car to drop further. The contours shown in Figure 7.3 and discussed in Chapter 7, clearly identify the presence of two peaks of streamwise velocity in the floor located at the floor's inlet and at the diffuser's inlet. These have different magnitudes but the same position for all diffuser angles studied. This location matches the one predicted by literature and coincides with where streamlines curve. Streamline curvature must occur as a consequence of a pressure gradient developing a force. When curving around the front to squeeze under the car and to follow the angled diffuser surface, the flow accelerates. The case where $\theta = 15°$ presented the highest velocity peak measuring $1.32U$, 32% faster than freestream. The velocity vectors on the midplane of the vehicle were extracted and interpolated on a straight probe line. Utilizing Bernoulli's relationship between velocity and pressure, Figure 7.15 and Figure 7.16 were generated. These show how increasing the diffuser angle increases velocity through the floor through the diffuser pumping effect. Increasing (diffuser) outlet area, which, in perfect conditions is characterized by atmospheric pressure, forces the pressure upstream at the diffuser inlet to drop. This effect

is reduced for the diffuser with $\theta = 15°$ and completely disrupted for the diffuser with $\theta = 20°$. Integrating the pressure distributions leads to an estimation of the downforce produced at 6 m/s, the average test speed. This measures around 60 g for the diffuser with $\theta = 10°$. Although the $\theta = 15°$ geometry produced larger low-pressure peaks, the geometry with $\theta = 10°$ performed the best among the ones tested due to the large portion of low-pressure flow under the floor ($0 < x/L_u < 0.75$).

Another interesting aspect of the flow physics expected in the diffuser is the possible presence of vortices. As the pressure under the car and outside is different and when a surface divides these regions, a vortex would form at the finite edge of this separating surface. One research question, aimed to locate these vortices and measure "*how the(ir) intensity [...] vary when changing the diffuser angle*". The vortices found by a few authors and described in the literature (Chapter 2) were not observed. Some rotation is captured (Figure 7.12) but opposes the predicted direction. This is the case since mass flow leaks out of the underfloor region instead of being "sucked" in (Figure 7.8). This was shown to be the result of the strong disturbance created by the tire's wake. Indeed, despite the diffuser and the car in ground effect producing low pressure underneath the floor, the size and roughness of the tyres generated an even stronger low pressure in their wake, forcing air to flow outwards. This loss of flow through the sides is also the main reason why even when the outlet area is equal or inferior to the characteristic freestream area, near-perfect expansion is not possible. Leaking mass through the sides effectively reduces the outlet area that a given inlet area can successfully expand to.

8.2. Analysis of Velocity Field Convergence

The process of averaging multiple runs to obtain a statistically converged velocity field is a key feature of the experiment carried out. Indeed, single runs do not produce enough data to draw conclusions and they may entail unsteady flow features that do not concern the research. The present investigation set out to find "*how many runs are required for the average velocity field to converge with a rate of 2 %*". To address this, the process of interpolating the scattered data, after the coordinate system conversion, was repeated multiple times using a progressively increasing number of runs to investigate the convergence of the velocity field. The study found that a minimum of 15 measurements are required to achieve a convergence of 5% while more than 30 runs would be required to achieve a 2% rate of convergence. In hindsight, obtaining data from 25 runs was a good practical choice to trade off testing time and result convergence while allowing for a few runs to be discarded.

8.3. Recommendations and Scalability of the Method

Potential scalability and future optimization of the setup were important aspects that guided the design of the experiment. The first research question that encapsulated these goals aimed to determine "*to what extent can the setup be upscaled to allow for a full-scale vehicle to be the subject of measurements*". This question was addressed by making realism and scalability a top priority when designing the experimental setup. Indeed, decisions like running the car on the ground rather than on an elevated track, building the setup outdoors on a large stretch of paved road and using materials with specific properties to allow for a large and heavy vehicle to not damage the equipment were all taken with the goal of a future full-scale test in mind. Overall, a few adjustments would still have to be made to host a full-scale vehicle. While the transparent cover is designed to not break under the weight of a 2000 kg car, it would certainly deflect, causing apparent motion of the tracers due to light refraction within the thickness of the transparent plate. The stretch of road dedicated to the acceleration and braking should also be adjusted to ensure safety and repeatability.

Since the experimental campaign at the core of this investigation is the very first iteration of such a setup, there is plenty of room to improve the quantity and quality of the results. These concern the relative importance of the tires, the size of the seeding confinement and the mechanical stability of the vehicle. The recommendations, compiled from first-hand experience with the setup, answer the research question that aims to describe "*what can be learnt by developing the proposed setup to benefit a future application on a motorsport vehicle*". These insights will be crucial in generalizing the methodology to accommodate a larger and more complex vehicle, potentially leading to the design of a groundbreaking diffuser concept.

Seeding and seeding containment The size of the seeding containment should be tested more extensively to aid the detection of separated flow. As discussed, separated flow is characterized by cells that lack data since particles are not able to fill these regions. While in a wind tunnel experiment, the car is stationary and new tracers invest the test object continuously, the transient motion of the RC car in the setup constructed and the finite nature of the containment box provide little time for the tracers to settle. In a wind tunnel-like frame of reference, this would equal to producing bubbles only for 110 ms[2]. By making the containment box longer in the direction of motion of the car, more tracers may have the possibility to encounter and break into a separation bubble. This experiment utilized a containment volume resembling a tunnel with a length in the order of one car length positioned exactly on the measurement zone. Future tests could include a tunnel box two, three or four times the length of the vehicle in addition to identifying the best position for the bubble enclosure to be placed. The height and width of the enclosure could also be optimized to maximize particle concentration in the diffuser.

The Helium Filled Soap Bubbles, the tracers, are a key component that enables the tracking of the flow. During the campaign, the temperature ranged between $-1°C$ and $4°C$. This altered the viscosity of the soap flowing in the capillaries (the microtubes transporting air, helium and soap). Utilizing this type of bubble generator outdoors, and at such low temperatures has not been attempted in the past adjustments had to be done to successfully generate bubbles. The capillary tubes had to be heated by air convection with a heat gun to allow the soap to flow at the correct rate. In addition, the nozzle needed to be thoroughly cleaned and purged after every day of use. Future iterations of the setup should be equipped with heating elements and multiple spare nozzles with the associated capillaries to mitigate the risk of corrosion (by soap) damage.

Camera and light layout Two cameras are the minimum required in order to triangulate particles in 3D space. Obtaining an extra point of view through the use of another camera would drastically reduce the triangulation uncertainty. Utilizing more compact cameras would allow to fit three or four cameras inside the already existing trench used for this experimental campaign. The result would be more accurate triangulation but also a higher number of successfully triangulated particles. Indeed, the Shake-the-box algorithm may remove and discard real particles when the measured position error exceeds a given threshold.

Utilizing a different LED type could also help illuminate a larger portion of the moving vehicle, drastically increasing the number of particles tracked successfully. Indeed, tracing bubbles are present all around the vehicle since the box is three times as wide as the car but they cannot be tracked since they are not illuminated. This would also require to better manage reflections either in post-processing or physically with clever choice of viewing angles and mirrors.

[2]The bubbles fill the box which measures 0.7 m in the direction of the car. The vehicle traverses this domain at 6 m/s

Setup construction Despite the high stiffness of the transparent cover and the relatively light weight of the car, it was seen that the passing vehicle created millimetre-size oscillations in the polycarbonate sheet. These are not structurally problematic but create unwanted apparent motion in the images due to time-dependent changes in the angle of refraction through the sheet's thickness. This issue can be tackled by clamping the sheet on the concrete to increase its stiffness. The current setup is equivalent to a "*simply supported*" beam while a clamped layout would result in a (double) "*fixed end*" beam equivalent. The latter type of support produces smaller deflections at equal load.

The impossibility of deducing trends by observing the average characteristic ride height of each diffuser is the consequence of the little downforce produced but also the bumpiness of the car's motion over the measurement zone. Despite renting out smooth road coverings to form a proper track for the vehicle, videos of the car reported unpredictable large jumps and other undesired motions dampened by the suspension system. While the track plates smoothened out roughness with a characteristic length in the order of 1 cm such as gaps between tiles and cement roughness, larger road imperfections cannot be dealt with flexible road coverings. Future experiments should be carried out by actively managing the smoothness of the track by adjusting road covering plates or constructing an alternative track design. It is expected that unwanted ride height differences, relative to the rest ride height, would decrease with a larger vehicle or when using a more advanced suspension system. Reducing the motion of the car in the Z direction would allow to study ride height changes with more precision as well as better isolate the effect of the geometry changes.

Table 8.1: Speed and positional precision of vehicle's passage

Power Setting	**Speed ($\mu(\mathbf{U}) \pm 2\sigma$ [m/s])**	**Y-offset ($\pm 2\sigma$ [cm])**
1	4.74±0.14	14.7
2	8.61±0.23	24.9
3	11.20±0.44	39.8

Vehicle features Modifying the vehicle would be an important aspect to focus on when repeating the experiment. The recommendations concerning the vehicle choice are the following:

- Testing the car without a diffuser could provide an interesting comparison metric in order to better quantify the effect of the diffuser.
- The interference of the tyres could be minimized by choosing a wider vehicle with smaller, thinner and smoother tyres. The location of the tyres should also be updated to not coincide exactly with the inlet of the diffuser. Specifically, the tyres should be moved backwards with respect to the diffuser in order to better match real vehicles.
- While the energy source and the motors of the vehicle in question provided all the power necessary to move the model at up to 15 m/s, the car was never actually tested at this high velocity. This is due to the jumping and upsetting of the car's balance getting worse at higher speeds and due to the difficulty of piloting the RC car remotely with the necessary precision at high speeds. The current positional precision of the car's passage and of speed control is shown in Table 8.1. This data was obtained by measuring the position of the car relative to a target point and its velocity at one power setting set on the controller. Since the sideways offset is a variable centred at $y = 0$ cm only the standard deviation is provided. Observing that obtaining a velocity of $> 10m/s$ carries

an associated lateral positional uncertainly of ±40 cm (car's position at measurement zone is within 40 cm of the target for 95% of passages), it is clear that this vehicle and control type are not suitable for tests at higher speeds. This uncertainty is problematic since the width of the illuminated region is only 8 cm.

- In addition to making the vehicle more stable at speed, different diffuser parameters could be changed. For instance, the area ratio and the normalized ride height could be interesting non-dimensional independent variables of a future experiment. This would be possible only when ride height can be controlled more effectively.
- In the current experimental campaign, the vehicle's front was taped to create a flat leading edge to reduce reflections and increase mass flow. This concept could be further improved by creating a smoother "entry" section for the flow entering the underbody region.

In conclusion, the strides made and the challenges encountered highlighted how complex and sensitive the discipline of (on-site) track testing is. The large number of variables and unpredictable external factors such as road surface, temperature, pilot skill, tyre shape, tyre size, and the vehicle's mechanical dynamics all contribute to creating a highly dynamic system. While wind tunnel tests can isolate these factors and focus on the predetermined study objective, crucial relationships between elements of the vehicle's motion may be overlooked and accidentally removed through the process of isolation and simplification of the problem. On-site characterization of the flow with the use of the setup designed and tested in this report allows to accurately and effectively evaluate many key flow indicators. Specifically, the results described the diffuser angle for maximum downforce, the process of separation and performance loss at high diffuser angles and the mechanism of mass flow loss through the sides.

Bibliography

[1] O. H. Ehirim. "Aerodynamics and performance enhancement of a ground-effect diffuser". PhD thesis. 2018.

[2] W. Terra, A. Sciacchitano, and F. Scarano. "Aerodynamic drag of a transiting sphere by large-scale tomographic-PIV". In: *Experiments in Fluids* 58 (2017), pp. 1–14.

[3] D. Schanz, S. Gesemann, and A. Schröder. "Shake-The-Box: Lagrangian particle tracking at high particle image densities". In: *Experiments in fluids* 57 (2016), pp. 1–27.

[4] W. Toet. "Aerodynamics and aerodynamic research in Formula 1". In: *The Aeronautical Journal* 117.1187 (2013), pp. 1–26.

[5] *F1: Rivals 'dismayed' at Red Bull floor complexity*. https://www.autoracing1.com/pl/400659/f1-rivals-dismayed-at-red-bull-floor-complexity/. Accessed: 18/09/2023.

[6] *The most powerful Ford GT ever*. https://www.ford.com/performance/gt/. Accessed: 18/09/2023.

[7] O. H. Ehirim, K. Knowles, and A. J. Saddington. "A Review of Ground-Effect Diffuser Aerodynamics". In: *Journal of Fluids Engineering* 141.2 (June 2018), p. 020801. ISSN: 0098-2202. DOI: 10.1115/1.4040501. eprint: https://asmedigitalcollection.asme.org/fluidsengineering/article-pdf/141/2/020801/6372264/fe_141_02_020801.pdf. URL: https://doi.org/10.1115/1.4040501.

[8] J. Marklund. *Under-body and diffuser flows of passenger vehicles*. Chalmers Tekniska Hogskola (Sweden), 2013.

[9] L. Jowsey and M. Passmore. "Experimental study of multiple-channel automotive underbody diffusers". In: *Proceedings of the Institution of Mechanical Engineers, Part D: Journal of Automobile Engineering* 224.7 (2010), pp. 865–879. DOI: 10.1243/09544070JAUTO1339.

[10] A. George and J.E. Donis. "Flow patterns, pressures, and forces on the underside of idealized ground effect vehicles." In: 7 (Jan. 1983), pp. 69–79.

[11] A. E. Senior. "The aerodynamics of a diffuser equipped bluff body in ground effect". PhD thesis. University of Southampton, 2002.

[12] A. Ruhrmann and X. Zhang. "Influence of Diffuser Angle on a Bluff Body in Ground Effect". In: *Journal of Fluids Engineering* 125.2 (Mar. 2003), pp. 332–338. ISSN: 0098-2202. DOI: 10.1115/1.1537252. eprint: https://asmedigitalcollection.asme.org/fluidsengineering/article-pdf/125/2/332/5901864/332_1.pdf. URL: https://doi.org/10.1115/1.1537252.

[13] A. Newey. *How to build a car*. Harper Collins, 2017.

[14] L. Jowsey. "An experimental study of automotive underbody diffusers". PhD thesis. Loughborough University Loughborough, UK, 2013.

[15] Kevin R. Cooper, T. Bertenyi, G. Dutil, J. Syms, and G. Sovran. "The Aerodynamic Performance of Automotive Underbody Diffusers". In: *SAE Transactions* 107 (1998), pp. 150–179. ISSN: 0096736X, 25771531. URL: http://www.jstor.org/stable/44740947 (visited on 09/13/2023).

[16] A. E. Senior and X. Zhang. "The force and pressure of a diffuser-equipped bluff body in ground effect". In: *J. Fluids Eng.* 123.1 (2001), pp. 105–111.

[17] R. J. Adrian and J. Westerweel. *Particle image velocimetry*. 30. Cambridge university press, 2011.

[18] J. Kompenhans, M. Raffel, L. Dieterle, T. Dewhirst, H. Vollmers, K. Ehrenfried, C. Willert, K. Pengel, C. Kähler, A. Schröder, and O. Ronneberger. "Particle Image Velocimetry in Aerodynamics: Technology and Applications in Wind Tunnels". In: Jan. 1999.

[19] M. A Passmore, A. Spencer, D. Wood, L. Jowsey, and P.S. Newnham. "The Application of Particle Image Velocimetry in Automotive Aerodynamics." In: (2010). ISSN: 0148-7191. DOI: 10.4271/2010-01-0120.

[20] F. Scarano. "Tomographic PIV: principles and practice". In: *Measurement Science and Technology* 24.1 (Oct. 2012), p. 012001. DOI: 10.1088/0957-0233/24/1/012001. URL: https://dx.doi.org/10.1088/0957-0233/24/1/012001.

[21] K. D. Hinsch. "Three-dimensional particle velocimetry". In: *Measurement Science and Technology* 6.6 (June 1995), p. 742. DOI: 10.1088/0957-0233/6/6/012. URL: https://dx.doi.org/10.1088/0957-0233/6/6/012.

[22] Q. Gao, H. Wang, and G. Shen. "Review on development of volumetric particle image velocimetry". In: *Chinese Science Bulletin* 58 (2013), pp. 4541–4556.

[23] G. E. Elsinga, F. Scarano, B. Wieneke, and B. W. van Oudheusden. "Tomographic particle image velocimetry". In: *Experiments in fluids* 41.6 (2006), pp. 933–947.

[24] R. D. Keane and R. J. Adrian. "Theory of cross-correlation analysis of PIV images". In: *Applied scientific research* 49 (1992), pp. 191–215.

[25] M. Raffel, C. E. Willert, F. Scarano, C. J. Kähler, S. T Wereley, and J. Kompenhans. *Particle image velocimetry: a practical guide*. Springer, 2018.

[26] A. M. C. M. G. Spoelstra. "Ring of fire as a novel approach to study cycling aerodynamics". In: (2022). DOI: 10.4233/uuid:5b51be97-aca7-4935-836a-be9b75f819df.

[27] F. Scarano, S. Ghaemi, G. C. A. Caridi, J. Bosbach, U. Dierksheide, and A. Sciacchitano. "On the use of helium-filled soap bubbles for large-scale tomographic PIV in wind tunnel experiments". In: *Experiments in Fluids* 56 (2015), pp. 1–12.

[28] J. Bosbach, M. Kühn, and C. Wagner. "Large scale particle image velocimetry with helium filled soap bubbles". In: *Experiments in fluids* 46 (2009), pp. 539–547.

[29] D. E. Faleiros. "Soap bubbles for large-scale PIV: Generation, control and tracing accuracy". In: (2021).

[30] N. Agüera, G. Cafiero, T. Astarita, and S. Discetti. "Ensemble 3D PTV for high resolution turbulent statistics". In: *Measurement Science and Technology* 27.12 (2016), p. 124011.

[31] *AirPods Pro (2nd generation)*. https://www.apple.com/airpods-pro/specs/. Accessed: 06/04/2024.

A

Scripts

Galilean transformation MATLAB processing loop including outlier detection

```
for i = 1:length(indices)  % Array of row number of frame block start
    j_start = indices(i);  % Start of current block
    if i < length(indices), j_end = indices(i+1)-4; % End of current block
    else, j_end = height(Data);
    end

    [x, y, z, u, v, w] = getVarss(tData(j_start:j_end, :));

    % Data transformation
    x = -(x - cys_t0(1) - Vx_car*(i));
    y = y - cys_t0(2));
    u  = -1/Vx_car*(u - Vx_car);
    v  = v/Vx_car;
    w  = w/Vx_car;

    % Outlier removal
    [x, y, z, u, v, w, ID] = getVarss(tData(j_start:j_end, :));
    badparticle_row = find(condition(x, y, z, u, v, w)) + j_start;
    current_badparticle_row = ID(badparticle_row);
    badtracks = [badtracks; current_badparticle_row];
end
```

Velocity field convergence

```
r = 16;  % total number of runs
angle = 10;
data_r = getData(r); data_rm1 = getData(r-1);

[u, v, w] = data_r.binned_data.U{1:3};
mag_r = sqrt(u.^2+v.^2+w.^2);
[u, v, w] = data_rm1.binned_data.U{1:3};
mag_rm1 = sqrt(u.^2+v.^2+w.^2);
```

```
9
10  sqrare_delta = (mag_r -  mag_rm1).^2;
11  rmse = sqrt(nanmean(diff2(:)));
```

Downforce integration on 2D $z = h/2 = 12.5$ mm slice

```
1   angle = 10;  % Choose angle to extract data from correct file
2   data = load([num2str(real_angle),'d_full.mat']);
3
4   zh = -12.5; u_c = 6;  % z height of slice and freestream speed
5   rho_inf = 1.225; p_inf = 101325; q_inf = 0.5*rho_inf*(u_c^2);
6
7   [x, y, z] = data.binned_data.A{:};
8   [u, v, w, umag] = data.binned_data.U{:};
9
10  % Obtain indices of limits z=12.5, -100<y<100, -370<x<180
11  [~, zIndex] = min(abs(z(1, 1, :) - zh));
12  [~, ym] = min(abs(y(:, 1, 1)- (-100))); [~, yp] = min(abs(y(:, 1, 1)-
    ↪  (100)));
13  [~, xm] = min(abs(x(1, :, 1)- (-370))); [~, xp] = min(abs(x(1, :, 1)-
    ↪  (180)));
14
15  X_ = squeeze(x(1, xm:xp, 1)); Y_ = squeeze(y(ym:yp, 1, 1));
16  U = squeeze(u(ym:yp, xm:xp, zIndex)); W = squeeze(w(ym:yp, xm:xp, zIndex));
17
18  df = 0;
19
20  for i_x=1:length(X_)-1
21      for i_y=1:length(Y_)-1
22          dx = X_(i_x+1) - X_(i_x); dy = Y_(i_y+1) - Y_(i_y); A =
            ↪  dx/1000*dy/1000;
23          u_cell = (U(i_y, i_x) + U(i_y, i_x+1) + U(i_y+1, i_x+1) + U(i_y+1,
            ↪  i_x)) / 4;
24          w_cell = (W(i_y, i_x) + W(i_y, i_x+1) + W(i_y+1, i_x+1) + W(i_y+1,
            ↪  i_x)) / 4;
25          mag_cell = sqrt(u_cell^2+w_cell^2);
26          cp = 1 - mag_cell^2; p_low = cp*q_inf + p_inf;
27          df_cell = A*(p_inf - p_low); if ~isnan(df_cell); df = df + df_cell;
            ↪  end
28      end
29  end
```

B

Additional Results

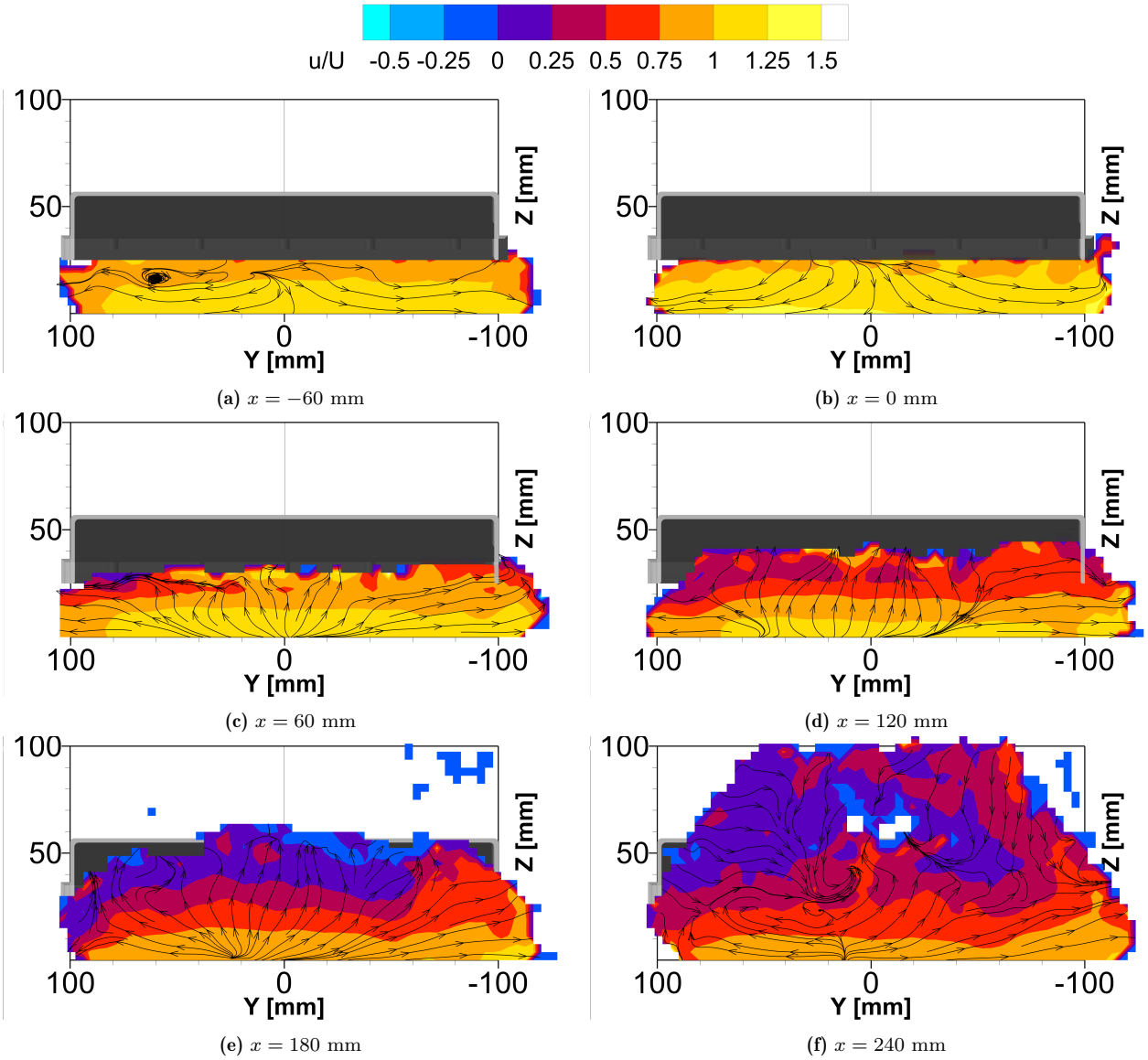

(a) $x = -60$ mm

(b) $x = 0$ mm

(c) $x = 60$ mm

(d) $x = 120$ mm

(e) $x = 180$ mm

(f) $x = 240$ mm

Figure B.1: X-slices from 60 mm before the diffuser inlet until 60 mm after the outlet for the diffuser for $\theta = 10°$ showing contours of streamwise velocity (u/U, perpendicular to plane) and streamlines

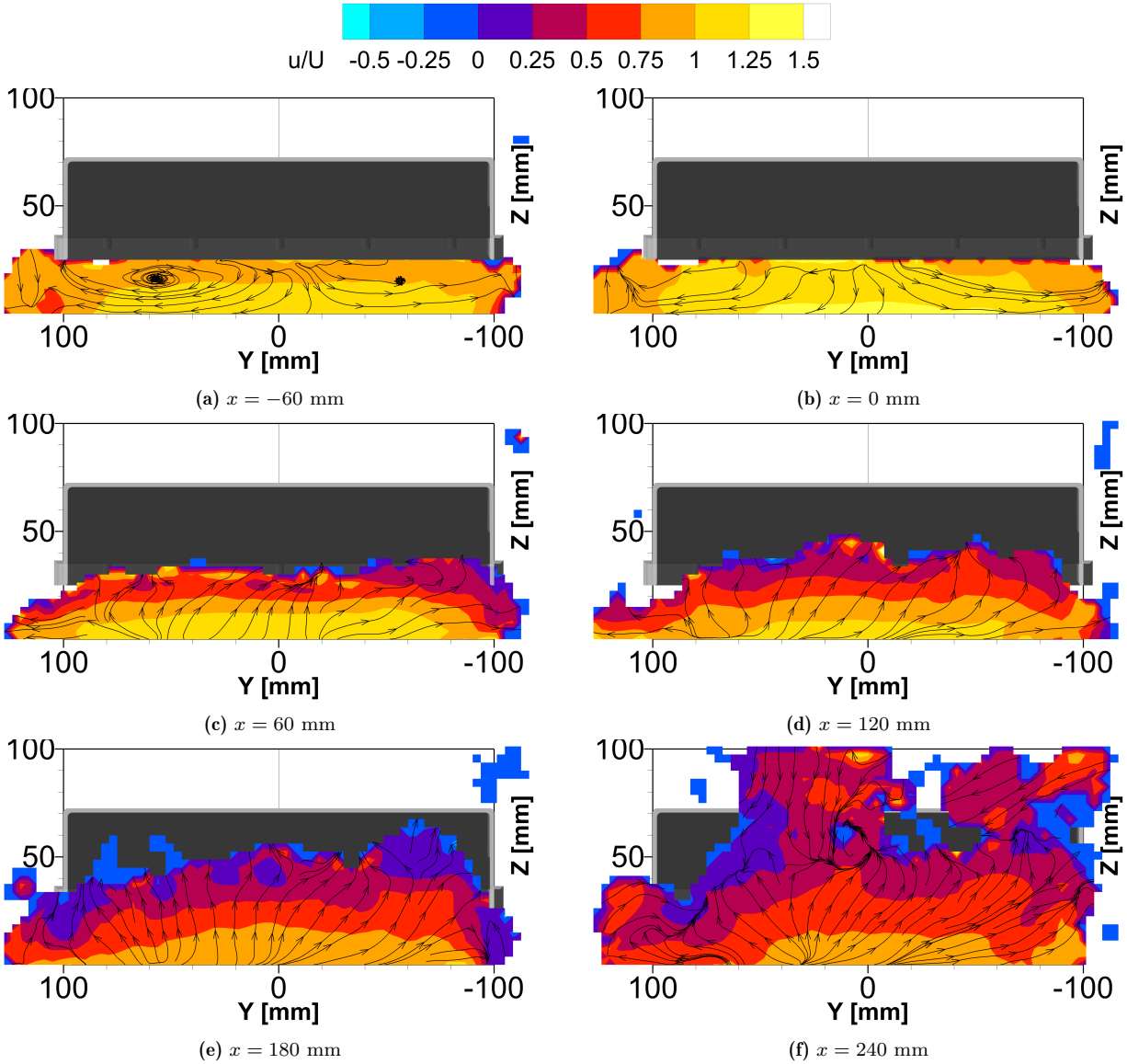

(a) $x = -60$ mm

(b) $x = 0$ mm

(c) $x = 60$ mm

(d) $x = 120$ mm

(e) $x = 180$ mm

(f) $x = 240$ mm

Figure B.2: X-slices from 60 mm before the diffuser inlet until 60 mm after the outlet for the diffuser for $\theta = 15°$ showing contours of streamwise velocity (u/U, perpendicular to plane) and streamlines

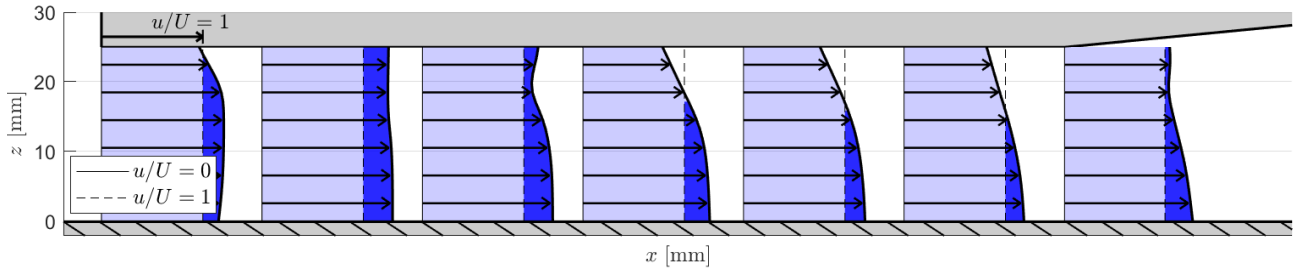

(a) $\theta = 10°$

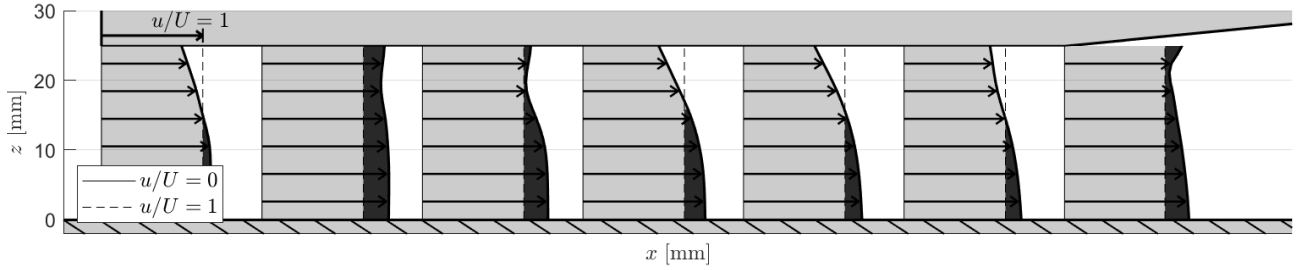

(b) $\theta = 20°$

Figure B.3: Profiles of u/U at different streamwise locations highlighting region where $u/U > 1$

C

Additional Experiment Photos

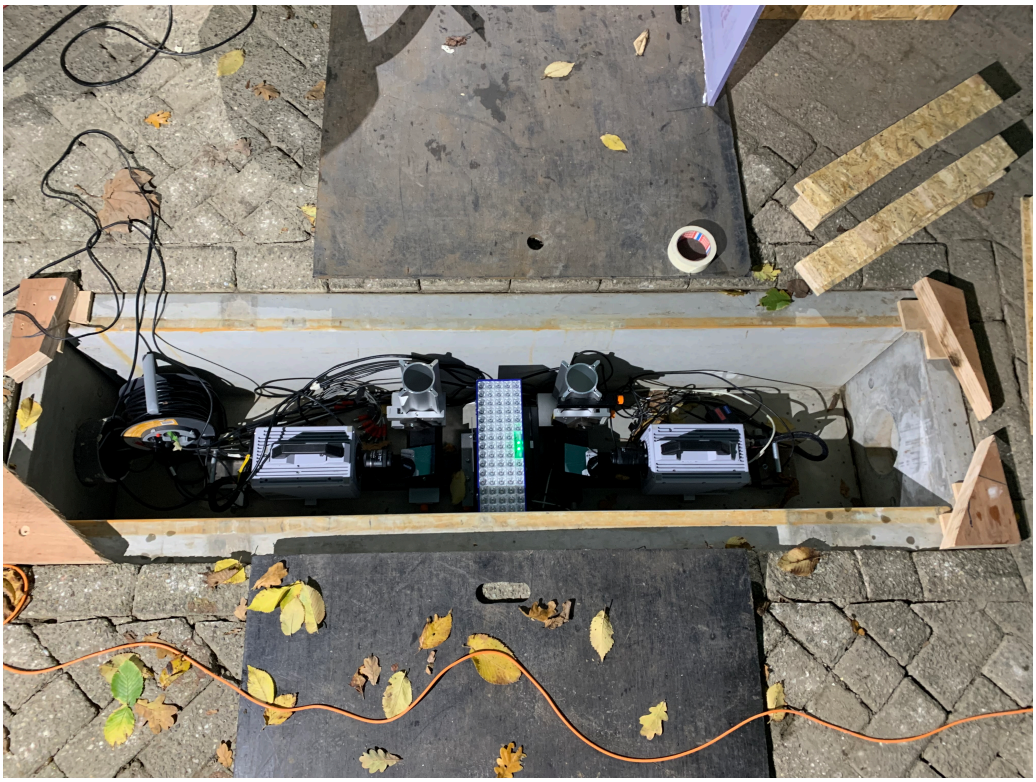

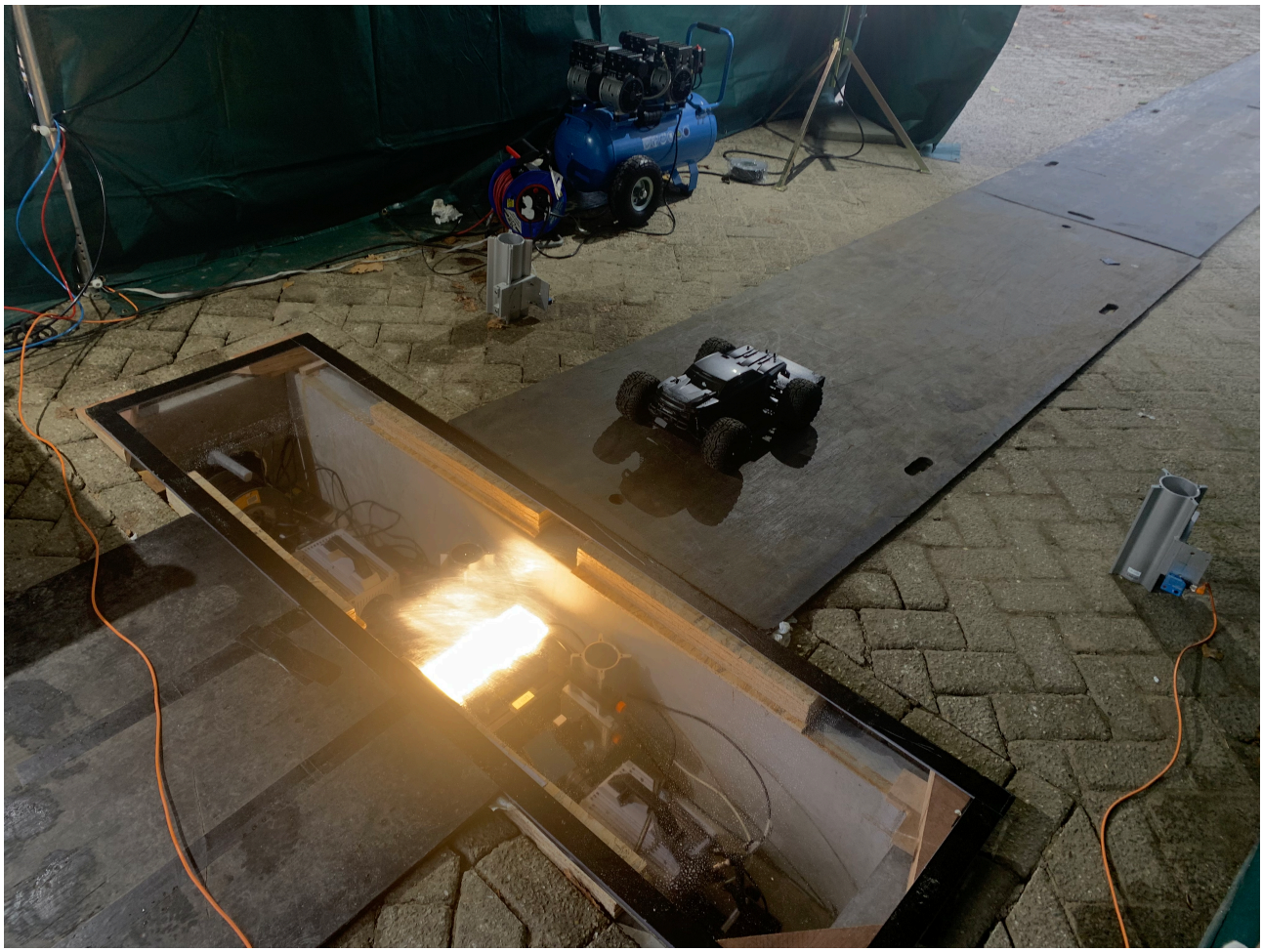

D

Campaign Support Staff

Due to the fact that the operation of the experiment was at minimum a 2 person job but required 3 people for the fastest data acquisition rate, a few people voluntarily offered their help. The main tasks covered by these helpers was: opening and closing the curtains, managing the tracer generating nozzle, check seeding density and communicate status with RC car pilot and control room operator. Adrian been present throughout the whole "Setup" phase as well as many other times during the testing days.

Table D.1: Experiment campaign schedule and third party contributions

			W - 22/11	**T - 23/11**	**F - 24/12**
9-11			Setup	Setup	Setup
11-13			Setup	Setup	Setup
14-16			Setup	Setup	Setup
16-18			Setup	Setup	Setup

	M - 27/11	**T - 28/11**	**W - 29/11**	**T - 30/11**	**F - 01/12**
9-11		Octavian	Alexander		Octavian
11-13	Michael	Octavian	Alexander	Aytek	
14-16	Michael			Aytek	Tamim
16-18		Alejandro	Michael	Alejandro	Luca

	M - 04/12	**M - 05/12**
9-11		
11-13	Tamim	
14-16	Austin	Francesco
16-18	Alessandro	

E

Vehicle CAD

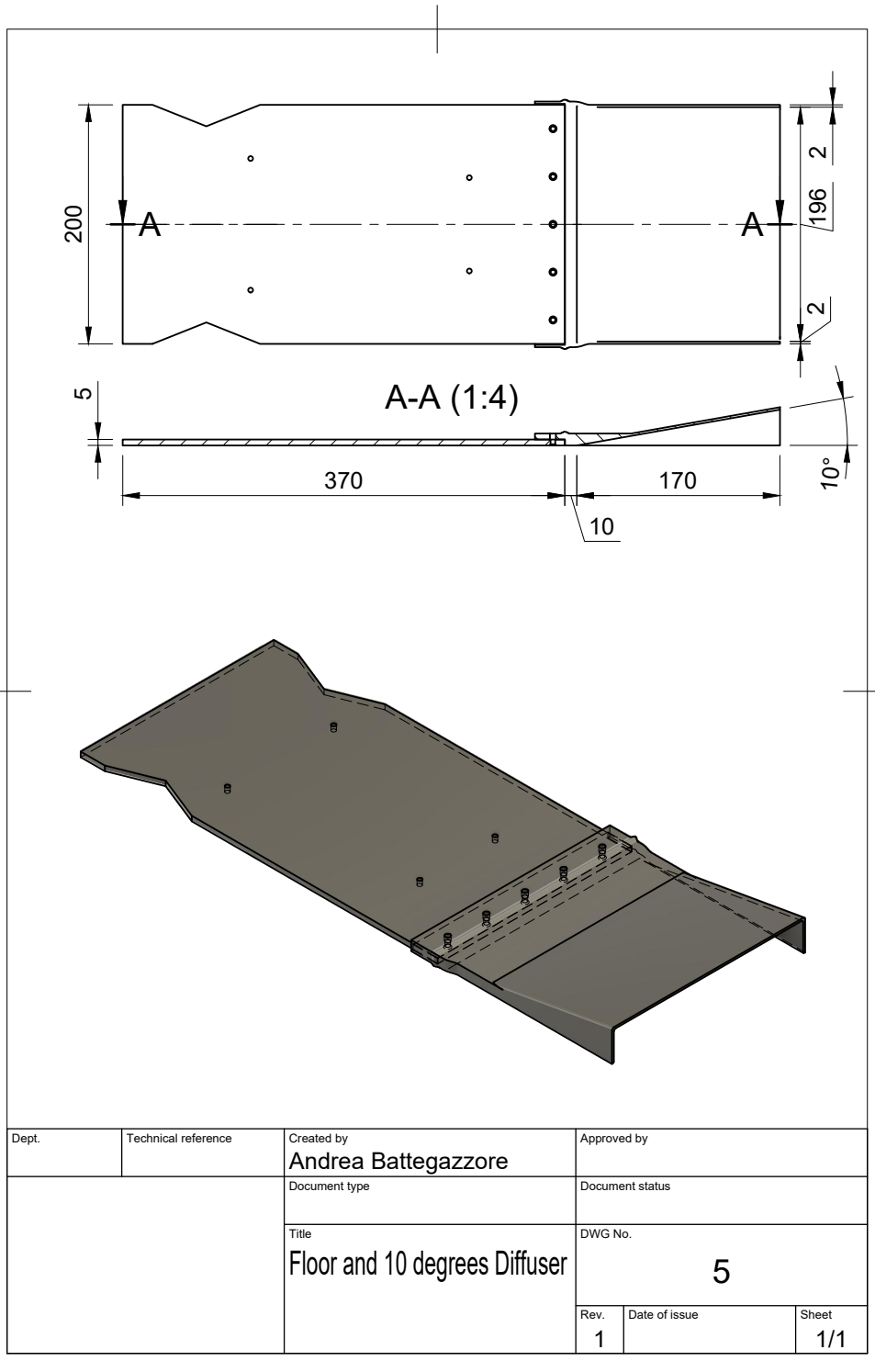

Figure E.1: Technical drawing of diffuser and floor model

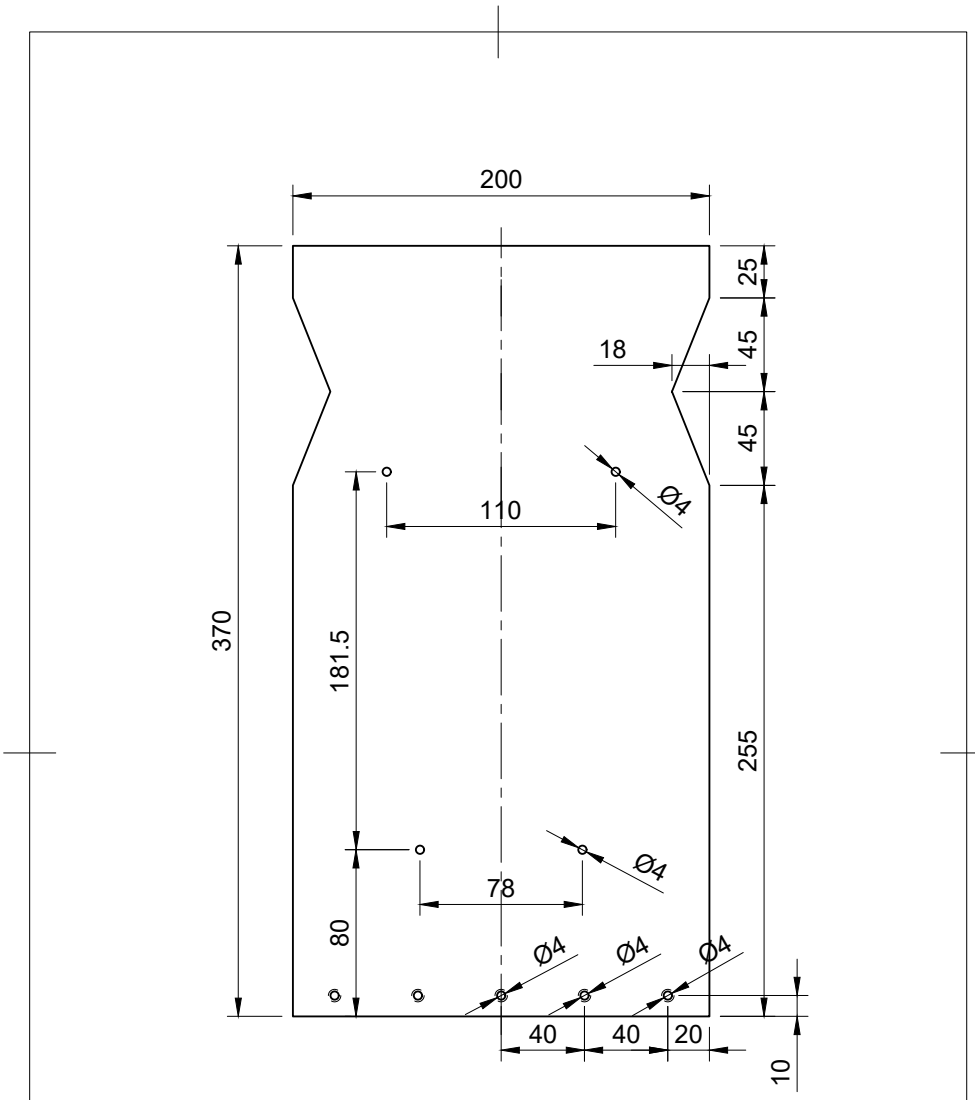

Dept.	Technical reference	Created by Andrea Battegazzore 10/10/2023	Approved by	
		Document type	Document status	
		Title RC car Floor	DWG No.	
			Rev. / Date of issue	Sheet 1/1

Figure E.2: Technical drawing of the manufactured plexiglass floor

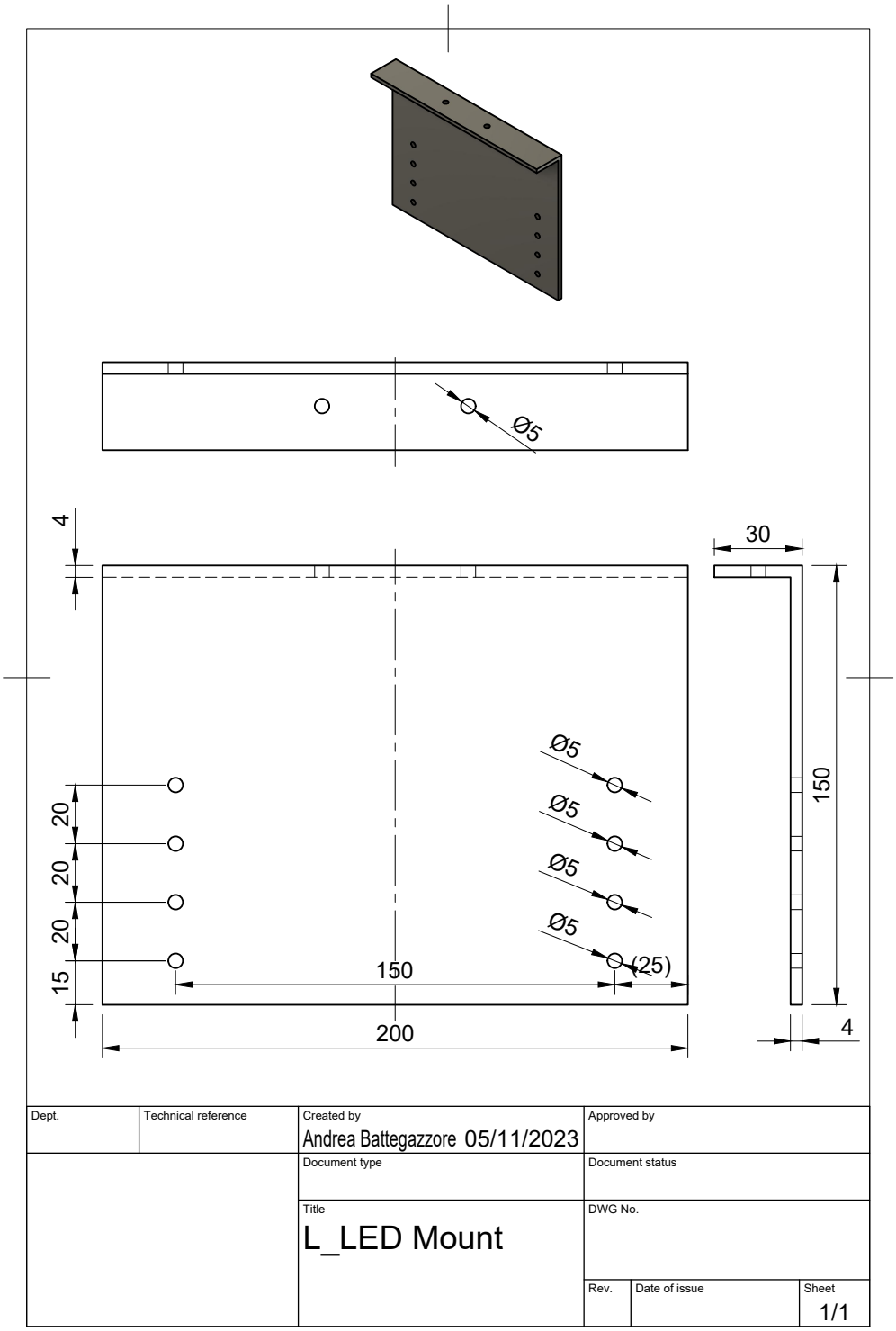

Figure E.3: Technical drawing of the custom steel LED mount used for part manufacturing

F

FEM Simulations

To ensure safety of operation, the thickness of the transparent plate was carefully selected. To make this choice, a worst-case scenario of a heavy transport truck passing over the concrete shell covered with the transparent top when the setup is left unattended was considered. The results are shown below.